NANOENGINEERED TISSUE SCAFFOLDS FOR REGENERATIVE MEDICINE IN NEURAL CELL SYSTEMS

By

Volkan Mujdat Tiryaki

A DISSERTATION

Submitted to
Michigan State University
in partial fulfillment of the requirements
for the degree of

Electrical Engineering—Doctor of Philosophy

2013

ABSTRACT

NANOENGINEERED TISSUE SCAFFOLDS FOR REGENERATIVE MEDICINE IN NEURAL CELL SYSTEMS

By

Volkan Mujdat Tiryaki

Central nervous system (CNS) injuries present one of the most challenging problems. Regeneration in the mammal CNS is often limited because the injured axons cannot regenerate beyond the lesion. Implantation of a scaffolding material is one of the possible approaches to this problem. Recent implantations by our collaborative research group using electrospun polyamide nanofibrillar scaffolds have shown promising results *in vitro* and *in vivo*. The physical properties of the tissue scaffolds have been neglected for many years, and it has only recently been recognized that significant aspects include nanophysical properties such as nanopatterning, surface roughness, local elasticity, surface polarity, surface charge, and growth factor presentation as well as the better-known biochemical cues.

The properties of: surface polarity, surface roughness, local elasticity and local work of adhesion were investigated in this thesis. The physical and nanophysical properties of the cell culture environments were evaluated using contact angle and atomic force microscopy (AFM) measurements. A new capability, scanning probe recognition microscopy (SPRM), was also used to characterize the surface roughness of nanofibrillar scaffolds. The corresponding morphological and protein expression responses of rat model cerebral cortical astrocytes to the polyamide nanofibrillar scaffolds versus comparative culture surfaces were investigated by AFM and immunocytochemistry. Astrocyte morphological responses were imaged using AFM and phalloidin staining for F-actin. Activation of the corresponding Rho GTPase regulators was investigated using immunolabeling with Cdc42, Rac1, and RhoA. The results supported the

hypothesis that the extracellular environment can trigger preferential activation of members of the Rho GTPase family, with demonstrable morphological consequences for cerebral cortical astrocytes.

Astrocytes have a special role in the formation of the glial scar in response to traumatic injury. The glial scar biomechanically and biochemically blocks axon regeneration, resulting in paralysis. Astrocytes involved in glial scar formation become reactive, with development of specific morphologies and inhibitory protein expressions. Dibutyryl cyclic adenosine monophosphate (dBcAMP) was used to induce astrocyte reactivity. The directive importance of nanophysical properties for the morphological and protein expression responses of dBcAMP-stimulated cerebral cortical astrocytes was investigated by immunocytochemistry, Western blotting, and AFM. Nanofibrillar scaffold properties were shown to reduce immunoreactivity responses, while PLL Aclar properties were shown to induce responses reminiscent of glial scar formation. Comparison of the responses for dBcAMP-treated reactive-like and untreated astrocytes indicated that the most influential directive nanophysical cues may differ in wound-healing versus untreated situations.

Finally, a new cell shape index (CSI) analysis system was developed using volumetric AFM height images of cells cultured on different substrates. The new CSI revealed quantitative cell spreading information not included in the conventional CSI. The system includes a floating feature selection algorithm for cell segmentation that uses a total of 28 different textural features derived from two models: the gray level co-occurance matrix and local statistics texture features. The quantitative morphometry of untreated and dBcAMP-treated cerebral cortical astrocytes was investigated using the new and conventional CSI, and the results showed that quantitative astrocyte spreading and stellation behavior was induced by variations in nanophysical properties.

Dedicated to my family.

ACKNOWLEDGEMENTS

First, I would like to thank my advisor, Professor Virginia M. Ayres, for her generous support and guidance throughout my PhD studies at Michigan State University. Her broad vision has always inspired me. It has been a great privilege having her as my advisor during these five years. Her enthusiasm and wise criticism greatly influenced my professional development.

I would like to thank Professors Hayder Radha, Martin Crimp, Alicia Pastor, and Yiying Tong for serving on my Academic Guidance Committee. Their technical feedback greatly expanded the scope of my research.

I would like to thank Professor David I. Shreiber for his technical discussions and essential contributions to our research. All primary cell cultures involving vertebrate animals in this dissertation are prepared at Rutgers, The State University of New Jersey. The Animal Welfare # is A3262-01. Fixed cell cultures are sent to Michigan State University. I thank Dr. Ijaz Ahmed for teaching me primary neural cell preparation and analysis techniques, and also his hard work in preparing the cell cultures, Western blotting, and immunofluorescence samples. I am also grateful to Professor Sally Meiners for introducing our research group the new polyamide nanofibrillar scaffolds, and her collaboration in our publications. I thank Professor Harini Sundaraghavan for providing tissue scaffolds including polycaprolactone (PCL), methacrylated hyaluronic acid (MeHA), and A6 gels. I also thank Corning Life Sciences for providing us polyamide nanofibrillar scaffolds.

I thank Dr. Melinda Frame for invaluable discussions about colocalization and quantitative immunolabeling analysis using confocal laser scanning microscopy. I thank Dr. Baokang Bi for teaching me use of SEM and Bruker Dimension 3100 AFM at the MSU Keck Microfabrication

Center, Lars Haubold (Fraunhofer, USA) for teaching me contact angle measurements, and Katerina Moloni and Sharath Nair (nPoint Inc.) for their assistance in closed-loop multimode AFM investigation. I am grateful to Abigail Tirrell for her help in imaging the AFM probe with FESEM and gold coating of various tissue scaffolds, and Kan Xie for his help in SEM imaging of polyamide nanofibers, PCL, MeHA, and A6 gels.

I also thank the Office of the Turkish Educational Attaché in New York for their support during my PhD studies. I thank the National Science Foundation of the United State of America (USA) for their support during my PhD studies through grant PHY-097776, awarded through the Physics of Living Systems Program, Dr. Kraston Blagoev, Program Director. The Dissertation Completion Fellowship provided by Michigan State University's Graduate School was a great honor and instrumental in helping me complete my work.

Finally, I would like to thank my father and my mother for understanding my wish to come to the USA for my PhD studies, which opened a new era in my professional career. They always loved and supported me. I dedicate my dissertation to them.

TABLE OF CONTENTS

LIST OF TABLES

LIST OF FIGURES

Chapter 1

Introduction

1.1 Motivation

Tissue engineering, or regenerative medicine, is a multidisciplinary field that merges expertise from engineering, physics, and biology. Tissue engineering is based on experimental observations that, when injury sites are supplied with artificial scaffolds, the cell populations can regenerate and re-establish original functions within the surrounding tissue. Tissue engineering applications depend on the location of the organ or injury. Fundamental research is needed to design tissue scaffolds with appropriate mechanical, topographical, and biochemical properties.

Central nervous system (CNS) injuries present one of the most challenging problems. Regeneration in the mammal CNS is often limited because the injured axons cannot regenerate past the lesion. Implantation of a scaffolding material is one of the possible approaches to this problem, and recent experiments have shown promising results. However, more research is still needed before CNS tissue scaffolds can be designed and implemented successfully. Characterizing physical properties of tissue scaffolds and determining the corresponding cell behavior are required in order to improve the current tissue scaffold applications. The physical properties of the tissue scaffolds have been neglected for many years, and it has only recently been recognized that significant aspects include nanophysical properties such as nanopatterning [1, 2], surface roughness [3, 4, 5], local elasticity [6], surface energy [7, 8], surface charge [9], and growth factor presentation [10]. In this dissertation, the rat neural cell system was used to

model human CNS injuries. The advantages of using rats over other organisms as a model of human disease have been reviewed by Iannaccone and Jacob [11].

The characterization of tissue scaffold physical properties must be at the same nanoscale level as the cell-matrix interactions. Atomic force microscopy (AFM), a milestone invention in nanotechnology, has been used to investigate the surface roughness, elasticity, nanofibrillar architecture, and even growth factor presentation of tissue scaffolds [10]. Therefore, AFM has great potential for determining physical properties of tissue scaffolds. Conventional AFM was designed for planar substrates and therefore cannot provide automated property measurements along individual cylindrical nanofibers. Scanning probe recognition microscopy (SPRM), the integrated version of AFM with image processing, pattern recognition, and computer vision techniques, was developed in the Electronic and Biological Nanostructures Laboratory at Michigan State University. It can auto-track individual nanofibers, and therefore has the capability of collecting data from an individual nanofiber, and was recently used to characterize the physical properties of nanofibrillar scaffolds with higher detail than a conventional AFM [12, 13, 14, 15]. SPRM is expected to be used for new investigations of tissue scaffolds.

AFM is a surface technique that provides three-dimensional topography of samples. To identify cellular mechanisms, internal protein expressions must also be analyzed through the use of immunostaining. Immunostaining is a general term in biochemistry that applies to any use of an antibody-based method to detect a specific protein in a sample. Immunostaining covers a broad range of techniques used in histology, cell biology, and molecular biology that utilize antibody-based staining methods. Two of those techniques are immunocytochemistry and Western blotting, which are used in this dissertation. Both techniques are used to investigate cell behavior in response primarily to nanophysical cell environments.

1.2 Overview of tissue engineering for neural cell systems

Tissue engineering uses cells and/or scaffolding materials that will facilitate regeneration around a lesion, and improve or replace the biological function of an organ. This is a difficult task because the material has to provide appropriate signals to the tissue over time. To be successful, the scaffolding material has to mimic all aspects of the natural environment of cells. It should provide appropriate mechanical support to the cells in the lesion area, and should be degraded during the healing process. The type of tissue dictates the appropriate methods of tissue engineering.

Mammals have a nervous system that is divided into the peripheral nervous system (PNS) and the CNS. The CNS consists of the brain, spinal cord, optic, olfactory, and auditory systems, and the PNS includes all other neural cells outside the CNS. The regeneration capability differs between the two systems. The neurons in the PNS are able to regenerate to some extent; but the neurons in the CNS often cannot regenerate and CNS injury usually results in paralysis. Neural tissue engineering seeks the optimum engineering and life science approach that will provide the appropriate environment for the neurons to grow past the lesion and re-gain their original function.

Current neural tissue engineering applications have been tested on animals, and promising results have been obtained [1]. The regeneration capability of rodents is known to be better than that of humans. Until the techniques can be perfected for rodents, clinical applications are not yet warranted.

1.3 Nanoscale imaging of tissue scaffolds

Optical microscopy has been the most commonly used technique in the biomedical sciences; however, its resolution is limited by the optical diffraction limit, which is on the order of half the wavelength of light. Assuming a light source with a wavelength of 500 nm, the optical diffraction limit, also known as Abbe diffraction limit, would be approximately 250 nm. This resolution is not enough to visualize the nanostructures of cells such as receptors, protein assemblies, channels, and nanoscale membrane protrusions [16]. The Abbe diffraction limit was one of the reasons why researchers sought a higher-resolution instrument. AFM, invented in 1986, is able to provide atomic resolution of samples under certain conditions. Since its invention, AFM has been successfully used for biomedical investigations including tissue engineering [10,14], drug delivery [17], protein folding [18], and clinical medicine [19].

Other techniques that provide nanoscale images are transmission electron microscopy (TEM) and scanning electron microscopy (SEM), which were invented in 1931 and 1938, respectively. Both techniques have been used to observe biological nanostructures. AFM has several advantages over TEM. TEM provides a two-dimensional projection of a three-dimensional volume of the sample while AFM provides a three-dimensional surface profile of the sample. TEM sample preparation involves expertise in fixation and sectioning, and the sample must be observed in vacuum. AFM sample preparation is easier than that of TEM as thin sectioning is not required and standard culture preparations can be used. Capturing an AFM image can be done in ambient air, and even in a liquid environment, which makes investigation of living cells possible. SEM and TEM techniques do not allow live cell imaging because they require a vacuum. A modified version of SEM, called the environmental SEM (ESEM), operates at atmospheric pressure and can be used to investigate living cells. Image capture time by AFM is longer than

by TEM, but the scan speed of AFM in the newest commercially available instruments is increased. AFM can be used not only for imaging at the nanoscale but also for characterizing the mechanical properties and surface charges of regenerative tissue scaffolds.

1.4 Summary of the following chapters

Details about the CNS, neural tissue engineering applications, and CNS injury are discussed in Chapter 2. The new SPM family member, SPRM, its principle, and its recent applications are presented in Chapter 3. Chapter 4 addresses confocal laser scanning microscope (CLSM), which provides three-dimensional localization of proteins and other cellular structures. The protein expression estimation technique using CLSM is included in this chapter. In Chapter 5, characterization of nanophysical properties of tissue scaffolds are described. The consequences of the nanophysical environment for the neural cell system are presented in Chapter 6. In Chapter 7, a new cell morphology evaluation technique is proposed. The advantages of the technique are compared to the conventional method. Finally, the summary of the dissertation and recommended future work are given in Chapter 8.

Figures that use images that originate from the candidate's thesis work are identified by an asterisk in the figure caption.

Chapter 2

Central nervous system

The nervous system is responsible for signal transmission throughout the animal body. The system is divided into the CNS and the PNS. The CNS consists of the brain, spinal cord, optic, olfactory, and auditory systems, and the PNS includes all other neural cells outside the CNS. The CNS transmits and interprets signals and also excites the PNS, whereas PNS innervates the muscles, and transmits and receives signals from the spinal column.

This dissertation will focus on neural tissue engineering applications for the rat CNS model. The differences between rat and human brain have not yet been fully addressed. The human brain is the largest among mammals relative to body size. Another difference is that the cerebral cortex of rodents is smoother than that of humans. Nonetheless, the advantages of using rats over other organisms as a model of human disease have been documented [11] and use of a rat model system is an accepted neural cell system investigative procedure.

2.1 Cellular components of the CNS

Neurons and glial cells are the two classes of cells in the CNS. Neurons are the main signaling cells, and glial cells are the supporting cells in the CNS. There are three different types of neurons in terms of function: sensory neurons respond to touch, sound, light and other stimuli affecting cells of the sensory organs that then send signals to the spinal cord and brain. Motor neurons receive signals from the brain and spinal cord, cause muscle contractions, and affect

glands. Interneurons connect neurons to other neurons within the same region of the brain or spinal cord. Neurons cannot undergo mitosis, whereas glial cells are able to divide. Although neurons cannot divide, they can extend or sprout axons under certain conditions.

Glia are not directly involved in information processing, but have vital roles such as supporting and insulating neurons, removing debris after injury, directing outgrowth of axons, and releasing growth factors. Glial cells are grouped as microglia and macroglia. Microglial cells are phagocytes that become activated after injury, infection, or disease. Macroglial cells are classified into oligodendrocytes, pericytes, and astrocytes. Oligodendrocytes insulate axons by providing a myelin sheath to enable efficient signal transmission in the CNS. Pericytes are connective tissue cells that occur around small blood vessels.

The importance of astrocyte functions is apparent from the ratio of the number of astrocytes to neurons, which is 1:6 in worms, 1:3 in the rodent cortex, and 1.4:1 in the human cortex. This indicates that the role of astrocytes increases as the complexity of the tissue increases [20]. The majority of the glial cells are astrocytes, which have a star-shaped cell body (Figure 2.1). Astrocytes are the key support cells for CNS neurons and have many roles; their functions include transferring nutrients from capillaries to neurons, removing wastes from neurons, contributing to the blood brain barrier, maintaining the potassium ion concentration in the extracellular space between neurons, and controlling the blood flow. Astrocytes are a very heterogeneous population of cells with specific morphologies and properties [21]. They are considered to be the cellular bridge between the capillary basement membrane and the neurons [22].

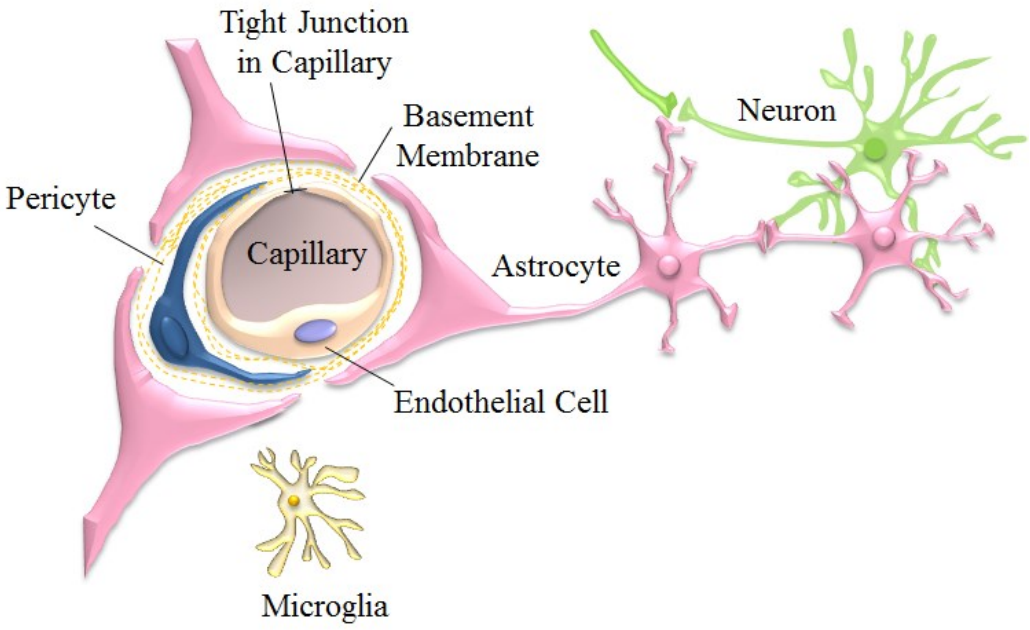

Figure 2.1: The blood brain barrier is formed by endothelial cells, basement membrane, and astrocyte endfoot. [22]. For interpretation of the references to color in this and all other figures, the reader is referred to the electronic version of this dissertation.

The cerebral cortex contains two types of matter: gray and white. White matter consists of myelinated and unmyelinated axons, whereas grey matter consists of the dendrites, cell bodies, neuroglia, unmyelinated axons, and axon terminals. Astrocytes are classified into fibrous and protoplasmic on the basis of cell morphology and anatomy. The astrocytes in gray matter are protoplasmic, whereas those in white matter are fibrous. Human astrocytes are known to be larger, structurally more complex, and more diverse than rodent astrocytes [23].

2.2 CNS extracellular matrix

The extracellular matrix (ECM) is the part of animal tissues that usually provides structural support and regulates intercellular communication. Animal cells, except blood cells, are

anchorage-dependent, and they adhere to a solid tissue composed of an ECM and resident cells or an adjacent cell to survive. The solid tissue ECM may have physical properties such as soft or stiff, thick or thin, and smooth or rough.

Cells adhere to other cells and the ECM through cell adhesion molecules. The ECM contains many types of structural and directive proteins such as collagens (type I, II, III), multiadhesive matrix proteins (laminin, fibronectin, entactin) and proteoglycans. The CNS ECM includes fibronectin, laminin, tenascin C, and proteoglycans. Epi-fluorescent images of ECM proteins in a matrix surrounding a capillary in a rat cerebrum are shown in Figure 2.2.

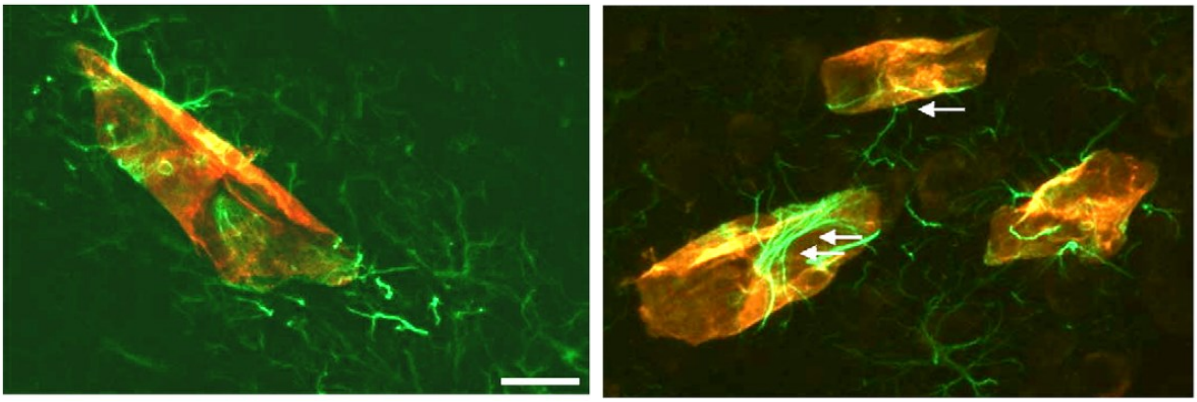

Figure 2.2: Epi-fluorescent images of ECM proteins and astrocytes in blood brain barrier. Immunolabeling was performed with antibodies against glial fibrillary acidic protein (GFAP) in order to dye astrocytes green, and either fibronectin (a) or laminin (b) with red. An astrocyte endfoot is shown by a single arrow, and an astrocyte cell body is shown by a double arrow in (b). Scale bar, 35 μm. [15].

2.3 Glial scar

Recent research indicates that the regenerative capability depends on the glial cells. After the CNS injuries in mammals, glial scar formation creates a barrier to axon regeneration. Glial scars consist mainly of reactive astrocytes and proteoglycans. Glial cells are believed to have a key

role in determining CNS regenerative capability. The response of astrocytes to injuries is called reactive astrogliosis. During astrogliosis, astrocytes enlarge, become stellate, proliferate, and up-regulate GFAP expression. Astrocytes are present in all CNS tissues without overlapping domains. However, in severe reactive astrogliosis astrocytes form overlapping processes. Astrocytes express four classes of proteoglycans: CSPG, heparan sulfate proteoglycans (HSPG), and keratan sulfate proteoglycans (KSPG) are inhibitory to neurite outgrowth [24]; whereas dermatan sulfate proteoglycans (DSPG) promotes axon regeneration in hippocampal neurons [25]. FGF2, a growth factor in the CNS, is known to be up regulated after injury, and promotes the proliferation and stellation of astrocytes in culture [26].

The reactive astrogliosis and glial scar formation has some beneficial functions such as protection of neural cells, restriction of the spread of inflammation and infection, and promoting tissue repair [27]. However, reactive astrogliosis has potential detrimental effects such as inhibition of axon regeneration [27]. Consequently, developing a scaffolding environment that would preserve the beneficial and attenuate the potential detrimental aspects of reactive astrogliosis would be highly useful in the CNS regenerative medicine [27].

2.4 History of neural tissue engineering applications

Currently, there is no available treatment to restore the nerve function in the CNS (Figure 2.3). Research in the CNS regenerative medicine increased after the 1980s. The developments were complicated due to the controversial results from several studies. Embryonic spinal cord grafts and peripheral nerve tissue grafts were able to support regeneration in the CNS; however, the nerve fibers often did not grow back across the peripheral-central transition zone [28]. Therefore,

efforts are focused on designing an environment that is permissive to axonal regeneration. Recent research shows that the permissive environment has to contain not only biomolecular signals, but also physical guidance cues [29, 30].

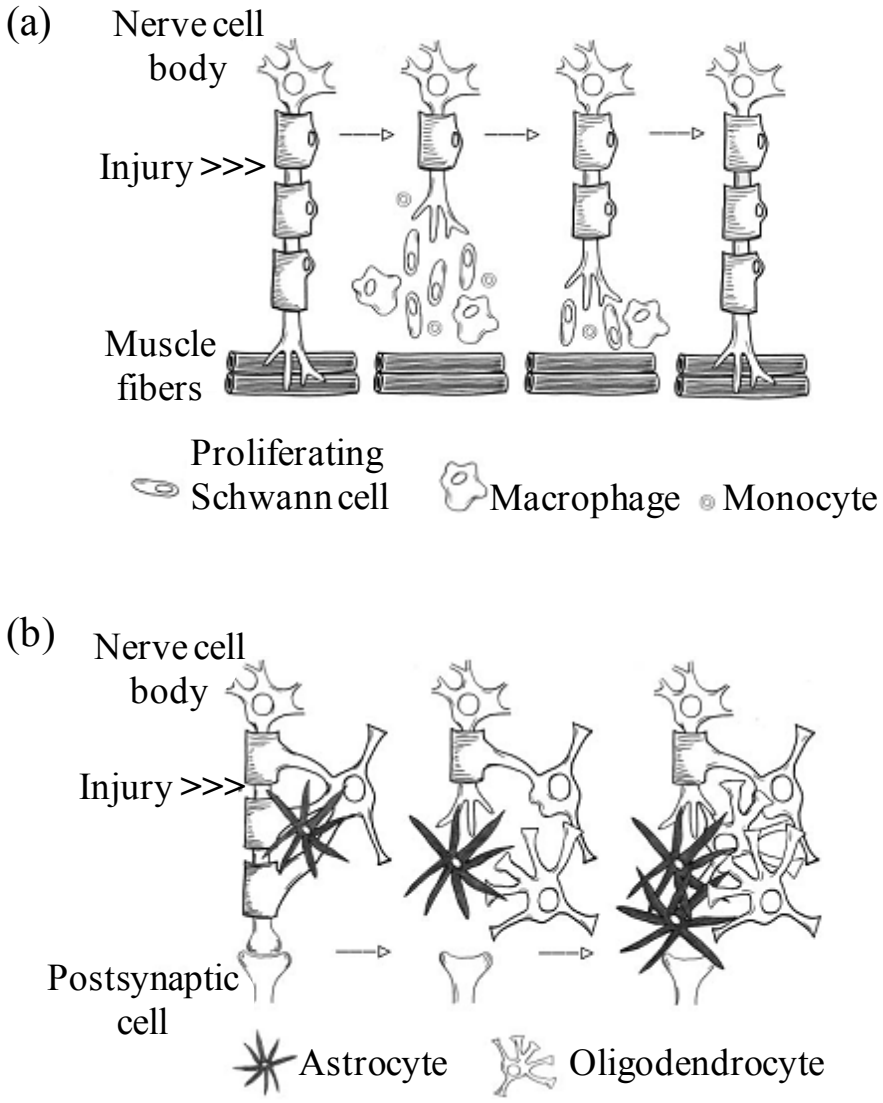

Figure 2.3: Comparison of regeneration in (a) PNS and (b) CNS. [29].

Physical guidance of axons is considered to be an important part of nerve repair. In the nineteenth century, autologous nerve grafts [31], metal tube [32], bone [33], and fat sheaths [34]

were used to physically guide the regeneration of the PNS. Autologous nerve grafts were accepted as the gold standard for treatment of PNS injuries in the late 1980s [35,36]. The other material types that are currently under research are nonautologus tissue, natural-based materials, and synthetic materials. Among those materials, synthetics are attractive because their physical and chemical properties such as surface roughness, surface energy, degradation rate, elasticity, and growth factor presentation can be optimized for specific applications. The challenges of the synthetic materials are the different inflammatory response of a body and compatibility with cell adhesion and tissue repair. Ideally, a synthetic material that would induce axonal regeneration should be biodegradable, semipermeable, and non-cytotoxic.

Recent research has identified an implantable scaffold composed of randomly oriented electrospun polyamide nanofibers that appears to have unusual wound healing properties for the CNS and that acts via modulation of the astrocyte response [12]. The polyamide nanofibers promote neuronal attachment and neurite generation [1], and produce no cytotoxicity *in vitro* [1] and *in vivo* [37]. They are also biodegradable, but not rapidly [37], which is an advantage because the materials has to remain until full recovery. Furthermore, the polyamide nanofibrillar scaffolds are flexible and therefore ideal for neural tissue engineering applications. Finally and more importantly, polyamide nanofibrillar scaffolds have shown promising results for the repair of spinal cord injury [38]. The present dissertation further investigates both the nanophysical properties of the polyamide nanofibrillar scaffolds and the neural cell responses to these scaffolds.

Chapter 3

Scanning probe microscopy

3.1 Atomic Force Microscopy

Scanning probe microscopy began with the invention of the scanning tunneling microscope (STM) in 1982 [39]. The invention of this instrument opened a new era of surface science. The STM tunneling current between the probe and the sample is kept constant while the probe scans over the surface of the sample. The vertical movement of the z piezo is recorded at each x,y coordinate, which yields an image of the sample topography. One of the limitations of this instrument is that the sample has to be electrically conductive. Although images of low-conductivity samples with STM have been obtained [40], it is not easy to establish a tunneling current with low-conductivity samples such as biological samples.

AFM, or scanning force microscopy, is another type of scanning probe microscope. AFM was developed within four years of the invention of STM. An AFM system consists of scanning, probe, sensor, vibration isolation, controller, and computer systems. The principle of AFM is to scan the surface of a sample with an AFM probe that is attached to a cantilever. The cantilever is flexible and has a specific spring constant. The probe is kept atomically close to the surface. The tip scans the specimen line by line by an accurate piezo-scanner. The top of the cantilever has a polished region, and the vertical movement of the tip is measured by transmitting a laser beam to the polished surface, and then detecting the reflected laser light from the cantilever.

In this thesis, the SPM technique that was primarily used was AFM. Contact mode AFM, tapping mode AFM, and SPRM were used to image the cell cultures and to investigate the nanophysical properties of culture surfaces.

3.1.1 Contact mode AFM

Contact mode was the first developed imaging mode of AFM, and it can be used to capture images of non-conductive samples. In this mode, a probe attached to the end of a cantilever is scanned over the sample surface while a split photodiode detector measures the magnitude of cantilever deflection from the reflected laser beam. The photodiode measures the intensity of laser light on top minus the intensity of laser light on the bottom divided by the total incident light. The feedback loop maintains constant deflection via the input from the photodiode detector [41]. A contact mode schematic representation of AFM is shown in Figure 3.1.

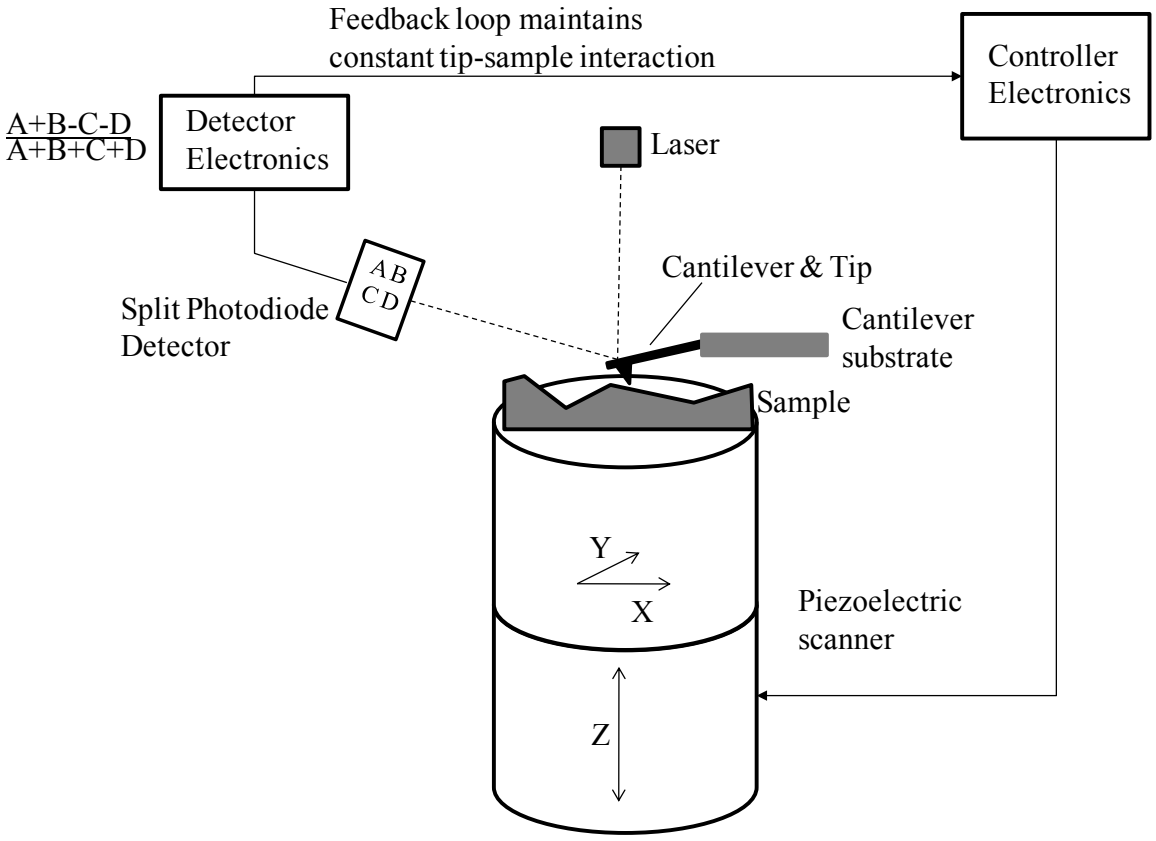

Figure 3.1: Schematic of contact mode AFM. [41].

The force that the tip applies to the sample can be calculated using Hooke's law in contact mode AFM:

$$F = kx \tag{3.1}$$

where F, k, and x are the force, spring constant and cantilever deflection, respectively. The constant deflection means a constant force is applied to the sample. AFM height data is constructed by recording the voltage applied to the z piezo at the same time the probe's (x,y) position. The deflection data in contact mode AFM is obtained by recording the cantilever deflection that occurs prior to re-establishing the constant force.

Contact mode AFM investigation can be performed in ambient air and liquid environment. However, lateral and normal forces may reduce spatial resolution and may damage biological samples.

3.1.2 Tapping Mode AFM

In tapping mode AFM [41], the cantilever is oscillated approximately at its resonance frequency and an amplitude range of typically from 20 nm to 100 nm. The tip lightly "taps" the specimen, and the tip contacts the surface at its minimum point of the cycle. The tip sample distance affects both the amplitude and the frequency of the tip. The change in frequency gives information about the sample. The feedback loop keeps the amplitude constant based on the four cell photodiode RMS amplitude measurement. At each lateral (x,y) point the vertical z point is recorded that maintains the setpoint amplitude. The z point recordings generate the topography of the sample. A phase image is obtained when the frequency change or the phase shift of the tip is recorded at each (x,y) point. The phase shift is very sensitive to the material and topographic properties.

In tapping mode AFM lower forces are applied to sample as compared to the contact mode, which means less damage to soft tissues. The scan speed is slightly slower than contact mode AFM.

3.2 Applications of AFM

AFM is an instrument that can reach macromolecular resolution with relatively short sample preparation time and over a wide temperature range. High-resolution imaging capability led AFM to have many applications for biomedical sciences. AFM is a marker-free imaging tool for obtaining sample topography. The tapping mode, pico-newton imaging system of AFM, was

developed after the nanonewton forces of contact mode was shown to damage the soft biological tissues in some cases. The successful operation of AFM in liquid environment allowed biomedical scientists to perform experiments in nearly native environment conditions [42,43].

There are some disadvantages of AFM that are also important to realize. AFM requires complementary investigations such as CLSM to obtain sub-surface information. The scanning speed of AFM is slow compared to optical and fluorescence microscopy and SEM. A typical scan in AFM requires several minutes, which may be longer depending on the resolution and scan rate. The relatively slow rate of AFM may also reflect thermal drift of the sample [44]. Finally the lateral resolution is limited by the shape of probe. AFM image is affected by the radius of the probe curvature and tip sidewall angles. The effect of AFM probe shape on the AFM height image is illustrated in Figure 3.2.

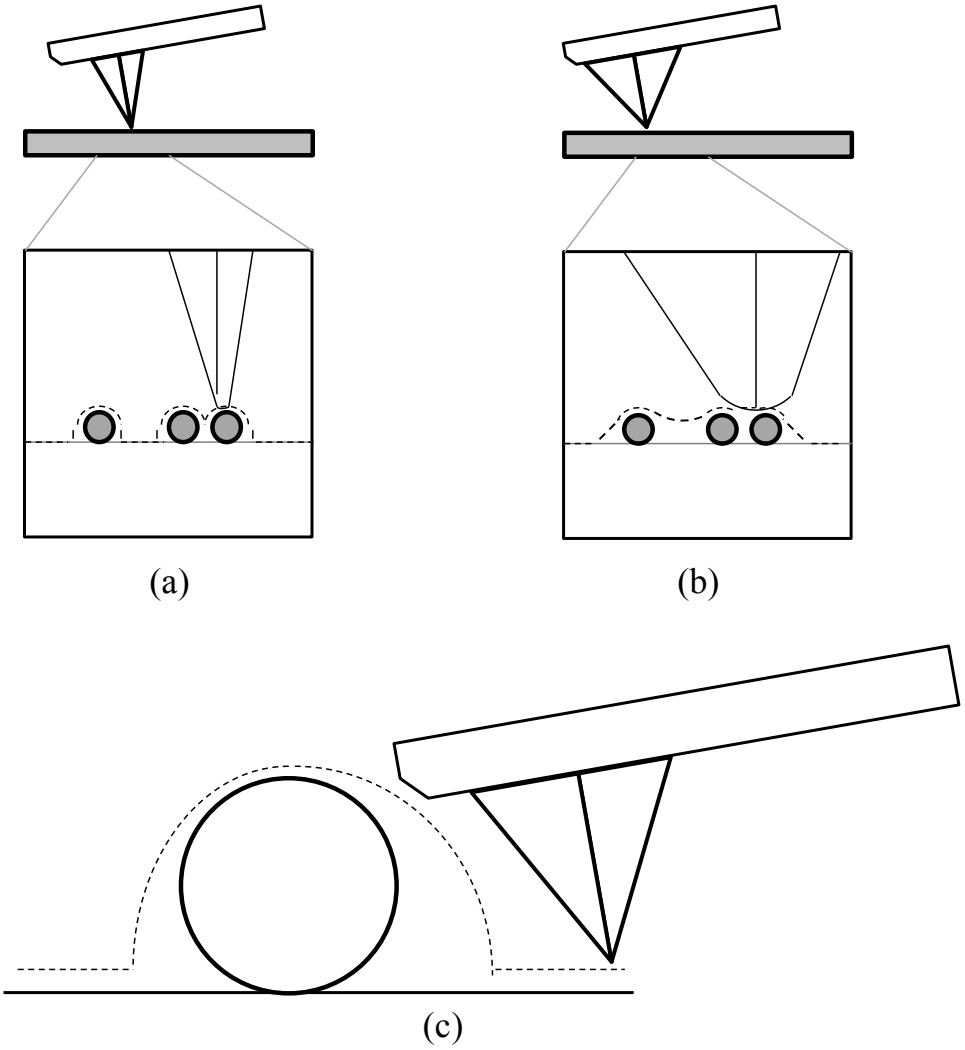

Figure 3.2: ((a) and (b)) The effect of AFM probe cone angle on the tip dilation artifact in AFM. (c) Dashed lines show the measured AFM height data and the solid lines show the real surface data. [41].

AFM is not only an instrument to visualize samples with macromolecular resolution. AFM force curves can be used to investigate material properties such as elasticity, Hamaker constant, adhesion, and surface charge densities, which was elegantly reviewed [45]. Therefore, AFM is an instrument that is likely to contribute to the biomedical sciences.

Numerous publications have been done with the contribution of AFM in biomedical sciences. The surface biology of DNA by AFM was investigated by Hansma [46]. AFM was used to

investigate the morphology of quiescent astrocytes cultured on different cell substrates [12]. It was used to image the molecular structure of aggrecan [47] and laminin on a planar surface [48]. AFM was also used to determine the elasticity of living tissue [49]. These applications and others demonstrate the capabilities of the instrument in the biomedical sciences. The increased scan speed of AFM in novel commercial instruments indicates the contributions of this instrument would likely to continue in the future.

3.3 SPRM and its applications

Scanning probe recognition microscopy (SPRM) is a new scanning probe microscopy capability developed recently in an NSF GOALI collaborative partnership with Veeco Instruments (now Bruker). In SPRM, the scanning probe microscope system itself is given the power to auto-track specific regions of interest through feature recognition coupled with adaptive scan plan generation and implementation. 'Feature' is not just topography, e.g. nanoscale elasticity was investigated as a physical property feature. SPRM is an approach that works directly with the interaction sensing capability of a scanning probe microscope, which inherently has atomic to nanometer scale resolution. The human operator interaction is now focused to the decision-making level rather than the execution level, and the research emphasis evolves from sample imaging to feature/property investigation.

For AFM based surface roughness measurements, if the region of interest is not rectangular, such as nanofibers, the surface roughness measurements need to be repeated many times. SPRM allows adaptively following along individual nanofibers within a nanofibrillar tissue scaffold. The comparison of SPRM auto-track imaging versus traditional AFM imaging was demonstrated

and histograms of various scaffold surface roughness were analyzed by Fan et al. [50]. This work has demonstrated the advantages of SPRM for nanoscale tissue scaffold investigations.

SPRM was recently used [51] for nanoscale elasticity measurements to collect local force curves at nanofiber median points with the tip normal to the nanofiber cylinder axis. Measurements from several nanofibers were compiled into a statistical representation of the nanofibrillar matrix. The measurements were related to a Young's modulus using a Hertz model.

SPRM was used to investigate the surface roughness along individual nanofibers and given in Chapter 6 of this thesis.

Chapter 4

Confocal Laser Scanning Microscopy

Confocal laser scanning microscopy (CLSM) is a technique that captures high-resolution in-focus images from selected depths of a sample. Images are acquired at each point on the focal plane and reconstructed by a computer, which yields three-dimensional images of samples. The image quality is enhanced compared to optical microscopy because images are acquired from multiple depths and are not superimposed. The principle of the CLSM was patented by Marvin Minsky in 1957 [52], but the development of this instrument was not achieved until the late 1980s, when laser scanning systems became available.

4.1 The principle of CLSM

In CLSM, the laser beam passes through an aperture and then focuses on the small focal volume of the sample. Scattered, reflected, or fluorescent laser light from the illuminated spot is collected by an objective lens. A beam splitter reflects some of the collected light into the detection apparatus, which is usually a photomultiplier tube. The light intensity is then recorded by a computer. The detector aperture passes only the light that is coming from the focal point and prevents passing of the out-of-focus light (Figure 4.1). This yields sharper images than those of conventional fluorescence microscopy and enables capturing images of focal planes at various depths within the sample. Series of these images are called z-stacks [53].

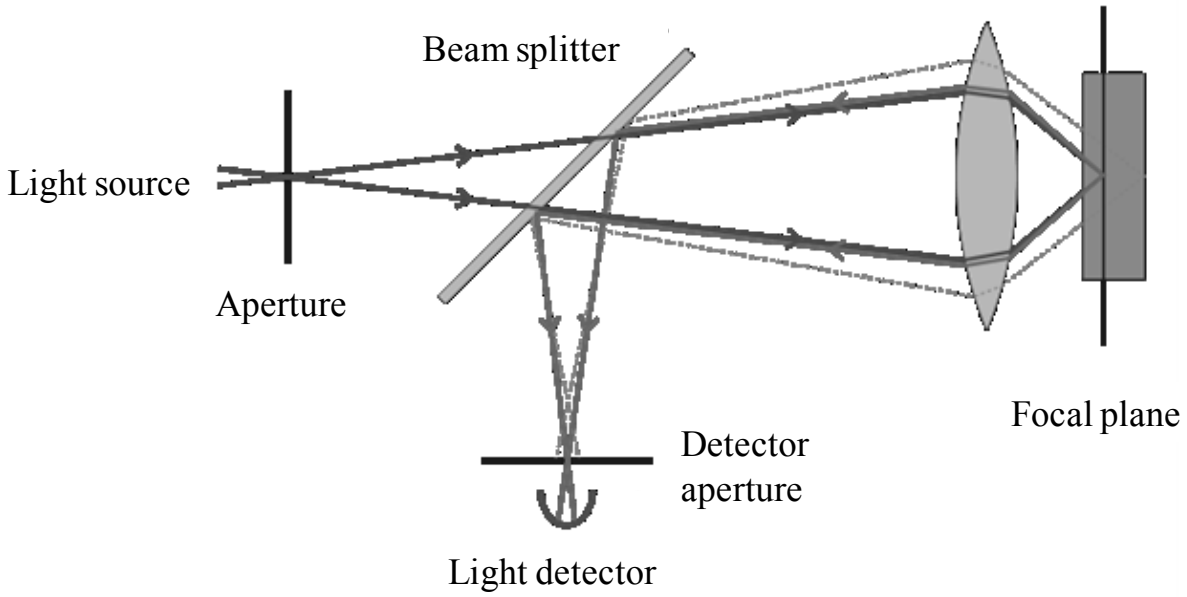

Figure 4.1: Schematic of confocal microscopy. The detector aperture obstructs the light that is not coming from the focal point, as shown by the dotted line. [53].

The detected light captured from the focal point within the sample represents one pixel in the final image. The laser beam is scanned over the horizontal plane of the sample by using servo-controlled oscillating mirrors. The focal plane is changed by raising or lowering the microscope stage, and a computer assembles the multiple successive focal plane images into a three-dimensional image of the sample. The lateral and axial resolution of CLSM can be as low as 66 nm and 175 nm, respectively [54].

4.2 Applications of CLSM

CLSM is currently used in many biological science disciplines, quantum optics, and nano-crystal imaging. In this research, CLSM was used to estimate the total expression of the cytoskeletal protein GFAP in astrocytes. In the healthy CNS, the level of GFAP expression in astrocytes may

not be detectable [27]. However, after injury to the CNS, the astrocytes are activated, or become reactive, and the level of GFAP is known to be up-regulated. Therefore, to determine the level of reactivity of astrocytes it is necessary to estimate the total GFAP expression within them. This requires a microscopy technique that is able to illuminate entire cytoplasm and detect protein levels in astrocytes individually. This can be achieved by CLSM. In this research, CLSM was used to estimate the total GFAP expression of astrocytes cultured on standard tissue culture surfaces and polyamide nanofibrillar scaffolds. Tubulin expression was also investigated. Cell nuclei were also stained to determine cell density.

Chapter 5

Nanophysical Properties of Tissue Scaffolds

When injury sites are supplied with appropriate biomaterials that physically and biochemically mimic the ECM, cells can regenerate and re-establish functional connections with surrounding tissue. However, studies indicate that tissue regeneration requires a very high level mimicry of nature [55].

The tissue scaffolding material under investigation in this research is a synthetic non-woven electrospun polyamide nanofibrillar matrix that has demonstrated promise for the repair of the injured spinal cord both *in vivo* and *in vitro* [37, 38]. A fundamental set of nanoscale properties of nanofibrillar scaffolds serve as the primary cues for the re-establishment of cell systems. The nanoscale cues for tissue scaffolds [56] were previously defined as surface roughness, surface energy, elasticity, and growth factor coverage, which are discussed below.

5.1 Surface Roughness

Surface roughness of the tissue scaffolds can influence cell adhesion and fates [57]. Human mesenchymal cells are more sensitive to exogenous signals when grown on surfaces with periodic surface roughness [58]. Lipski et al. have demonstrated that glass substrates coated with 50- to 300-nm diameter silica nanoparticles influenced cell morphology and metabolism in bovine aortic endothelial cells (BAECs) and mouse calvarial preosteoblasts (MC3T3-E1) [8].

These studies show that it is necessary to consider the surface roughness of the synthetic tissue scaffolds. The surface roughness is the root mean square of the height values in a specific region and is given by:

$$RMS = \sqrt{\frac{\sum_{i=1}^{N}(Z_i - Z_{ave})^2}{N}} \tag{5.1}$$

where N is the total number of pixels in the region, Z_i is the height value of the pixel, and Z_{ave} is the average height value for AFM height data.

For AFM-based surface roughness measurements, if the region of interest is not rectangle, such as nanofibers, the measurements need to be repeated many times. The comparison of SPRM auto-track imaging versus traditional AFM imaging was demonstrated and histograms of various scaffold surface roughness values were analyzed by Fan et al. [50]. This work demonstrated the advantages of SPRM for surface roughness investigations of nanofibrillar scaffolds along individual nanofibers.

The surface roughness investigations of polyamide nanofibrillar scaffolds and comparative culture surfaces are presented in Chapter 6 of this thesis in combination with the astrocyte morphological and protein expression responses to this property.

5.2 Local elasticity

Elasticity is the physical property of the material that returns into its original shape after the deforming stress is removed. Stress is the force per unit area exerted on an object, and strain is

the relative deformation or change in shape and size of the object. If there is a linear relationship between stress and strain, the material is in the linear elastic regime, e.g., a metal spring. Stiffness is a measure of the resistance offered by an elastic object to deformation, which is:

$$k = \frac{F}{\delta} \tag{5.2}$$

where k is stiffness, F is the force applied to the object, and δ is the displacement produced by the force.

The elasticity of the cellular environment regulates cell adhesion, cell spreading, and cell differentiation [6]. Pelham and Wang [59] examined the responses of 3T3 cells to mechanical properties of a collagen-coated polyacrylamide substrate, and found that cells on flexible substrates had less spreading behavior and higher lamellipodial and motility activity than cells on rigid surfaces. A recent study showed that the stiffness of the scaffold material influenced the tissue bridging and axonal ingrowth for spinal cord injury [60]. These studies indicate that elasticity is a significant physical parameter for a tissue scaffold design.

The elasticity range of the cellular environment varies with tissue type [61]. The range of elasticity of cellular microenvironments is shown in Figure 5.1.

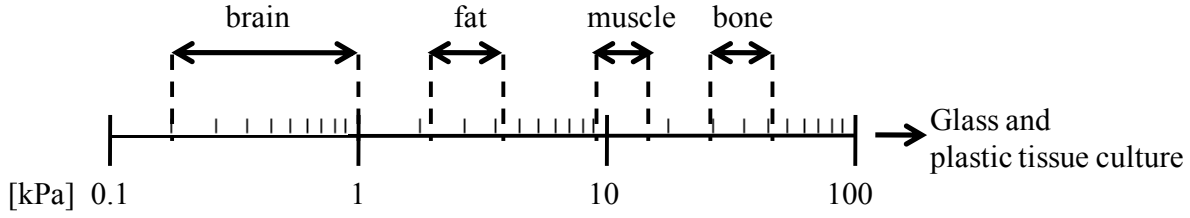

Figure 5.1: Elasticities of cellular microenvironments. The glass and plastic tissue cultures are stiffer than the stiffest bone tissue. [61].

The overall elasticity of the nanofibrillar scaffold that is sensed by the cell is dependent on the elasticity of individual nanofibers and the mesh density. AFM can be used to measure the elasticity of individual cells or culture surfaces by acquiring force curves on the surface [49].

To determine the elasticity of a material with AFM, force versus z-piezo displacement curves from a tissue culture are collected using the force mode analysis in Nanoscope Software version 5.30r3.sr3. The deflection sensitivity is determined on a silicon wafer, which is known to be stiffer than the planar culture surface [62]. The mean value of approximately ten measurements from the wafer is determined. The force versus z-piezo displacement data are then converted to force versus distance data, where distance is the gap between the atom at the far end of the AFM probe and the sample. Using the cantilever stiffness of the AFM provided by the manufacturer (0.58 N/m), the elasticity of tissue cultures was calculated from the retraction curve according to the Derjaguin, Muller, and Toporov (DMT) model [63].

$$\delta = \frac{a^2}{R} \tag{5.3}$$

$$a = \left((F_n + F_{ad}) \frac{R}{K} \right)^{1/3} \tag{5.4}$$

$$F_{ad} = 2\pi W_{132} R \tag{5.5}$$

$$\frac{1}{K} = \frac{3}{4} \left(\frac{1-\nu_{tip}^2}{E_{tip}} + \frac{1-\nu_{sample}^2}{E_{sample}} \right) \tag{5.6}$$

where δ is the indentation depth, a is the contact radius, R is the tip radius, F_n is the applied force, F_{ad} is the adhesion force, K is the total elastic modulus of the tip-substrate, W_{132} is the work of adhesion required to separate the AFM tip (subscript $_2$) from the cell substrate (subscript $_1$) in air (subscript $_3$) [64], ν_{tip} is the Poisson's ratio of the AFM tip, ν_{sample} is the Poisson's ratio for the sample, E_{tip} is the Young's modulus of the AFM tip, and E_{sample} is the Young's modulus of the sample. The calculations were implemented in MATLAB. Examples of AFM force curves that are relevant to these investigations are shown in Figure 5.2. These are: typical force curves from a "soft" material (Figure 5.2 (a). and from a "harder" material with a large adhesive component Figure 5.2 (b). All force curves investigated in this thesis resembled the second type, with an actual example given in Figure 5.2 (c). This motivated the use of the DMT model for extraction of the Young's modulus.

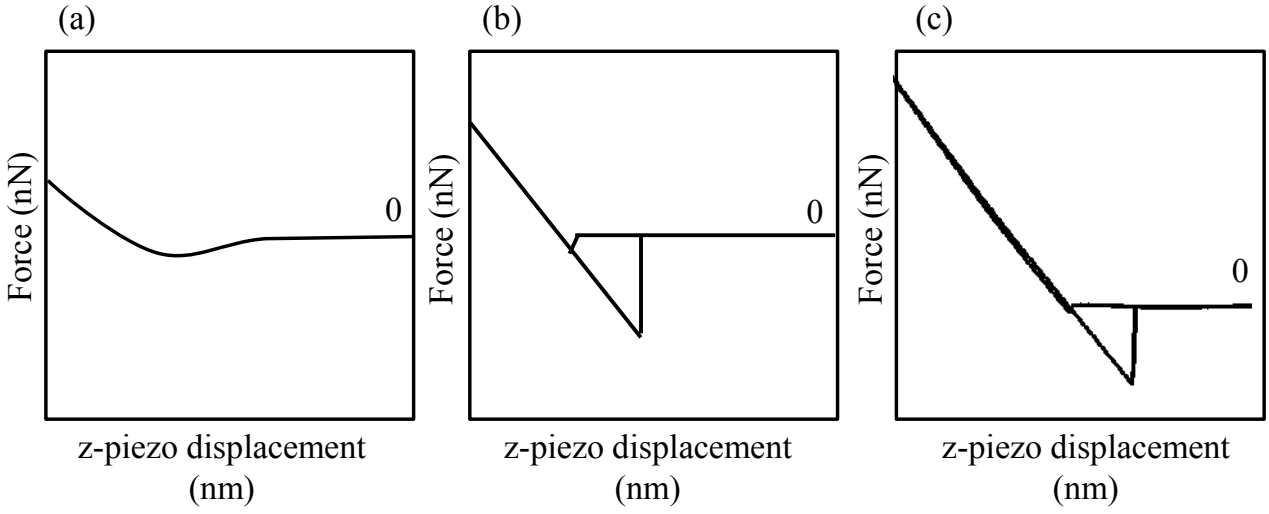

Figure 5.2: AFM force versus z-piezo displacement (F-z) curves including retraction and extension parts. (a) Typical F-z curve of a soft material, (b) typical F-z curve of a material with large adhesion component, and (c) F-z curve of PLL Aclar substrate.

To measure the elasticity of individual nanofibers, it is necessary to auto-track the nanofibers for statistically reliable measurements. SPRM can directly interact with an individual nanofiber without using a zoom box. The elasticity of individual tubules within a tissue scaffold was investigated by SPRM [65]. In another work, the elasticity histograms of a series of electrospun carbon nanofiber tissue scaffolds were performed with SPRM by Fan et al. [14].

The local elasticity of polyamide nanofibrillar scaffolds and comparative culture surfaces are investigated and are presented in Chapter 6 of this thesis in combination with the astrocyte morphological and protein expression responses to this property.

5.3 Contact angle

The surface energy is the free energy change γ when the surface area of a medium is increased by unit area. The contact angle of a liquid droplet can be used to determine the surface energy of a material. The equilibrium contact angle θ_C is determined from Young's equation:

$$0 = \gamma_{SG} - \gamma_{SL} - \gamma_{LG} \cos\theta_C \tag{5.7}$$

where γ_{SG} is the solid-vapor interfacial energy, γ_{SL} is the solid-liquid interfacial energy, γ_{LG} is the liquid-vapor interfacial energy, and θ_C is the equilibrium contact angle. A schematic of a liquid drop on a solid surface is given in Figure 5.3.

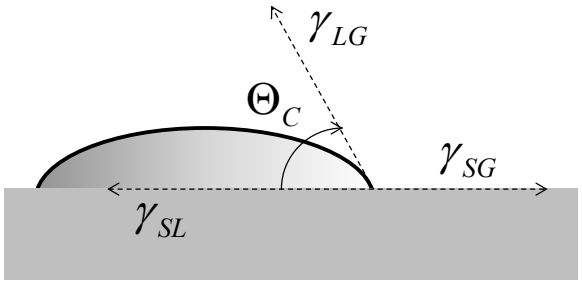

Figure 5.3: Schematic of a contact angle measurement. The contact angle θ_C depends on interfacial energies between solid and liquid (γ_{SL}), solid and vapor (γ_{SG}), and liquid and gas (γ_{LG}).

Hallab et al. suggested that for 3T3 fibroblast cells the surface energy may be a more important determinant of cell adhesion and proliferation [66], and may be more useful than surface roughness for influencing cell adhesion and cell colonization on engineered tissue scaffoldings (Figure 5.4).

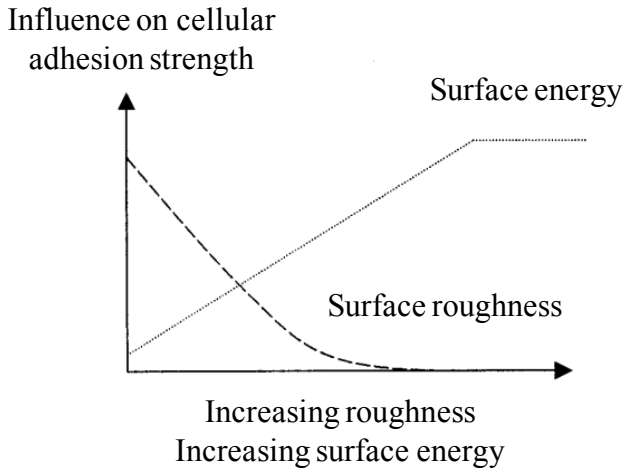

Figure 5.4: The relationship between surface roughness, surface energy, and their influence on cell adhesion. [66].

The contact angle measurements of polyamide nanofibrillar scaffolds and comparative culture surfaces are presented in Chapter 6 of this thesis in combination with the astrocyte morphological and protein expression responses to this property.

5.4 Work of adhesion

The surface energy of a material can also be calculated by measuring the work of adhesion using an AFM. Work of adhesion is the work needed to separate the AFM tip from the culture surface in ambient air. The adhesive component of the AFM force curves can be extracted and used to investigate the work of adhesion as previously given in Equation 5.5.

The work of adhesion of polyamide nanofibrillar scaffolds and comparative culture surfaces are presented in Chapter 6 of this thesis in combination with the astrocyte morphological and protein expression responses to this property.

5.5 Growth factor coverage

Growth factors are compounds that stimulate nearby target cells to grow and reproduce. Cells can receive and respond to the growth factors produced by other cells in their surroundings. Growth factors act as signaling molecules between cells. Cytokines and hormones are examples of growth factors that bind to specific receptors on the surface of target cells.

Transforming growth factor-β, glial cell line-derived neurotrophic factor, leukaemia inhibitory factor, and basic fibroblast growth factor are examples of growth factors that are involved in the blood brain barrier. FGF-2 is produced by astrocytes and induces specific functions in endothelial cells and astrocytes. It has proliferation and stellation effects on astrocytes. Delgado-Rivera et al. have demonstrated that FGF-2-modified nanofibrillar scaffolds are more permissive to neurite outgrowth than unmodified nanofibers and standard tissue culture surfaces [10]. This study showed the potential of both nanofibrillar scaffolds and the growth factors for neural tissue engineering.

Growth factor coverage characterization of tissue scaffolds can be obtained with AFM. Tapping mode AFM images of unmodified and covalently cross-linked FGF-2 polyamide nanofibrillar scaffolds are shown in Figure 5.5. The close-up images in (c) and (d) revealed the increased surface roughness of the FGF-2 cross-linked nanofibers. The increased surface roughness may be due to changes in both topography and surface chemistry of the modified nanofibrillar scaffolds [10].

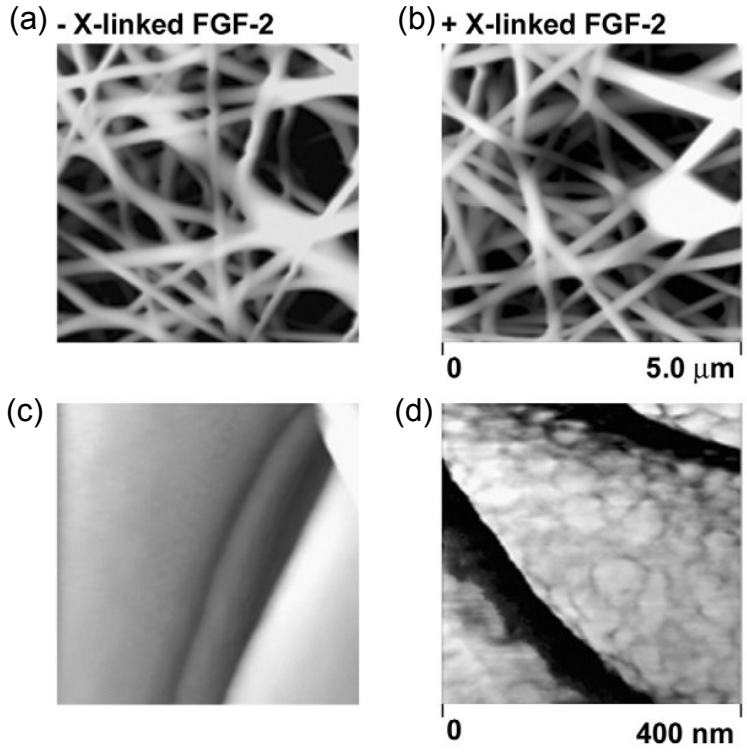

Figure 5.5: Tapping mode AFM images of unmodified polyamide nanofibers (a and c) and nanofibers covalently cross-linked with FGF-2 (b and d). Images in (a) and (b) are height and (c) and (d) are amplitude images. The difference in surface roughness of FGF-2 modified nanofibers is apparent in amplitude images. Images on same row have same scale bar. [10].

5.6 Effect of aging on nanofibrillar scaffolds

The physical properties of tissue scaffolds can change over time. This issue of tissue scaffold shelf life, with possible changes in directive signals to cells, was studied by Ayres et al. [67]. The

aging behavior of polyamide material was tested by Roggendorf [68], who concluded that one year after implantation, amorphous polyamide-6 sheets showed increased brittleness, crazing, and crystallization of the material. The effect of aging on biomaterial properties is under investigation by several groups [69]. The questions how scaffolds change over time, and how these changes may induce the cellular responses, are crucial for tissue scaffold design.

The nanoscale physical properties of newly electrospun polyamide nanofibrillar matrices < 1 year old versus those that were > 3 years old were investigated with TEM, contact angle measurements, and Raman spectroscopy. Significant differences in hydrophobicity and chemistry were observed. The cell responses of cerebellar granular neurons (CGNs) to the changed nanophysical properties of the new versus aged tissue scaffolds were also investigated using AFM. CGNs were selected because this is a comparatively homogeneous CNS cell population. In a healthy situation, CGNs respond by well-fasciculated (branched) neurite (dendrites and axon) outgrowth. CGNs can also display a guidance response to nano-patterning in their environment, including nanofibers [37]. CGN neuron outgrowth on the new versus aged tissue scaffolds were shown to differ. A new result was that a strong CGN drive toward obtaining a 3-dimensional environment, achievable with the aged nanofibrillar scaffolds, was observed.

5.6.1 Experimental Procedures

5.6.1.1 Preparation of scaffold samples

The polyamide nanofibrillar scaffolds electrospun on Aclar substrates were purchased from Donaldson Co., Inc. (Minneapolis, MN). The polyamide nanofibers were electrospun on Aclar

substrates for use as cell culture surfaces. Astrocyte cell cultures were prepared as previously reported [10, 37]. The old and new nanofibrillar scaffolds were kept in dark storage at room temperature for about 3 years and 1 year, respectively, except for experimental usage.

5.6.1.2 Preparation of cell cultures

Purity-enhanced cultures of primary CGNs were prepared from postnatal day 8 (P8) Sprague Dawley rats and grown to confluence in 75 cm^2 tissue culture flasks. The culture medium was composed of Dulbecco's Modified Eagle's Medium (DMEM, Invitrogen, Carlsbad, CA) + 10% fetal bovine serum (Invitrogen), 1% penicillin, and streptomycin, (Sigma-Aldrich, St. Louis, MO) to which 25 mM KCl was added. CGNs were then subcultured in 0.5 mL medium at a density of 30,000 cells/well directly on Aclar coverslips coated with nanofibers in 24 well plates. Cells were fixed with paraformaldehyde at 24 h.

5.6.1.3 Analytical techniques

AFM height images of the neuron cell cultures were captured with a Nanoscope IIIA (Bruker AXS Inc, Madison WI, formerly Veeco Metrology). TEM investigations of old and new nanofibers were performed using both a JEOL 100CX TEM operated at 100 kV and a JEOL FS2200 TEM operated at 200 kV (Japan Electron Optics Laboratories, Tokyo, Japan). The JEOL FS2200 TEM was used to obtain the selected area electron diffraction (SAED) of nanofibers with the camera length set to 60 cm. TEM sample preparation was as follows. For the plan-view TEM, the nanofibers were gently detached from the nanofibrillar surface with tweezers and suspended in 100% ethanol. The dispersion was then ultrasonicated for 30 sec (Branson

Ultrasonic Corporation, Danbury, CT). A droplet was placed on a lacey film coated TEM grid by pipette and dried in ambient air. For the cross-section TEM, nanofibrillar matrix samples electrospun onto 200 μm plastic coverslips were embedded in Poly/Bed 812 epoxy resin (Polysciences) and polymerized for 24h at 60 °C. Thin sections (70 nm thickness) of embedded nanofibers, were obtained using a MTX ultramicrotome (RMC, Boeckeler Instruments, Tucson, AZ) and using glass knives. Glass knives were prepared with a Glass Knife Maker (RMC, Boeckeler Instruments, Tucson, AZ). Thin sections were placed on 200 mesh copper grids and positively stained with 2% uranyl acetate in 50% ethanol and lead citrate (Reynold's formulation). Positively stained samples resulted in high contrast TEM images [70].

Contact angle measurements of culture surfaces were acquired using VCA Optima contact angle analysis equipment (AST Products Inc., Billerica, MA). One sample from each of five randomly selected areas per culture was analyzed.

Raman spectroscopy investigation was performed with a Kaiser Optical Systems HoloProbe Micro-Raman Spectrograph (Kaiser Optical Systems Inc., Ann Arbor, MI) coupled to an Olympus BX-60 optical microscope (Olympus, Center Valley, PA). For surface enhanced Raman spectroscopy (SERS), glass coverslips were coated with approximately 20-nm-thick gold in an Emscope Sputter Coater model SC 500 (Ashford, Kent, England) purged with argon gas. Old and new nanofibers were deposited by direct scraping with a clean razor blade to avoid chemical contamination.

5.6.2 Experimental Results

5.6.2.1 TEM and SAED investigation of new and aged nanofibers

TEM investigation of individual nanofibers did not show obvious structural differences between the new and aged nanofibers, e.g., the hollow, bamboo, and solid core structures described [14]. A light contrast interior with darker contrast walls suggestive of a hollow core structure was observed for both, as shown in the representative examples of Figure 5.6 (a) and (b). A similar conclusion of structural homogeneity was drawn from AFM investigation of new and aged nanofibrillar matrix surfaces. Dark contrast inclusions (arrows, Fig. 5.6 (a)) were also noted for the aged nanofibers investigated in this study. SAED results indicated that many nanofibers both new and aged were substantially crystalline and there were differences in the crystallinity between the new and the aged nanofibers (Figure 5.6 (e) and (f)).

The contact angles of the new and aged nanofibrillar surfaces were measured on five randomly selected regions. The new and aged nanofibers had 52.3 ± 2.2 ° and 63.3 ± 2.5 ° (mean ± standard deviation) contact angles, respectively. These results indicated that the polyamide nanofibrillar scaffolds became less hydrophilic with age.

5.6.2.2 Raman spectroscopy investigation

SERS Raman investigation of seven regions of each sample showed a typical polyamide spectrum with an Amide I: C=O stretch at about 1300 cm^{-1} and an Amide III: C=O/C=N stretch at about 1630 cm^{-1} for both new and aged samples. A cis N-H peak at about 1400 cm^{-1} , which has previously been reported for polyamide nanofibers, was also observed for both samples.

However, full width at half maximum (FWHM) increases on the polyamide peaks and the development of a broad disordered carbon peak [71] for the aged sample clearly indicated that changes in chemical bonding had occurred over time. It was noted that the Amide I C=O stretch appeared to be stronger in spectra from the aged nanofibrillar matrices. Representative spectra from both new and aged nanofibrillar matrices are shown in Figure 5.6 (c) and (d).

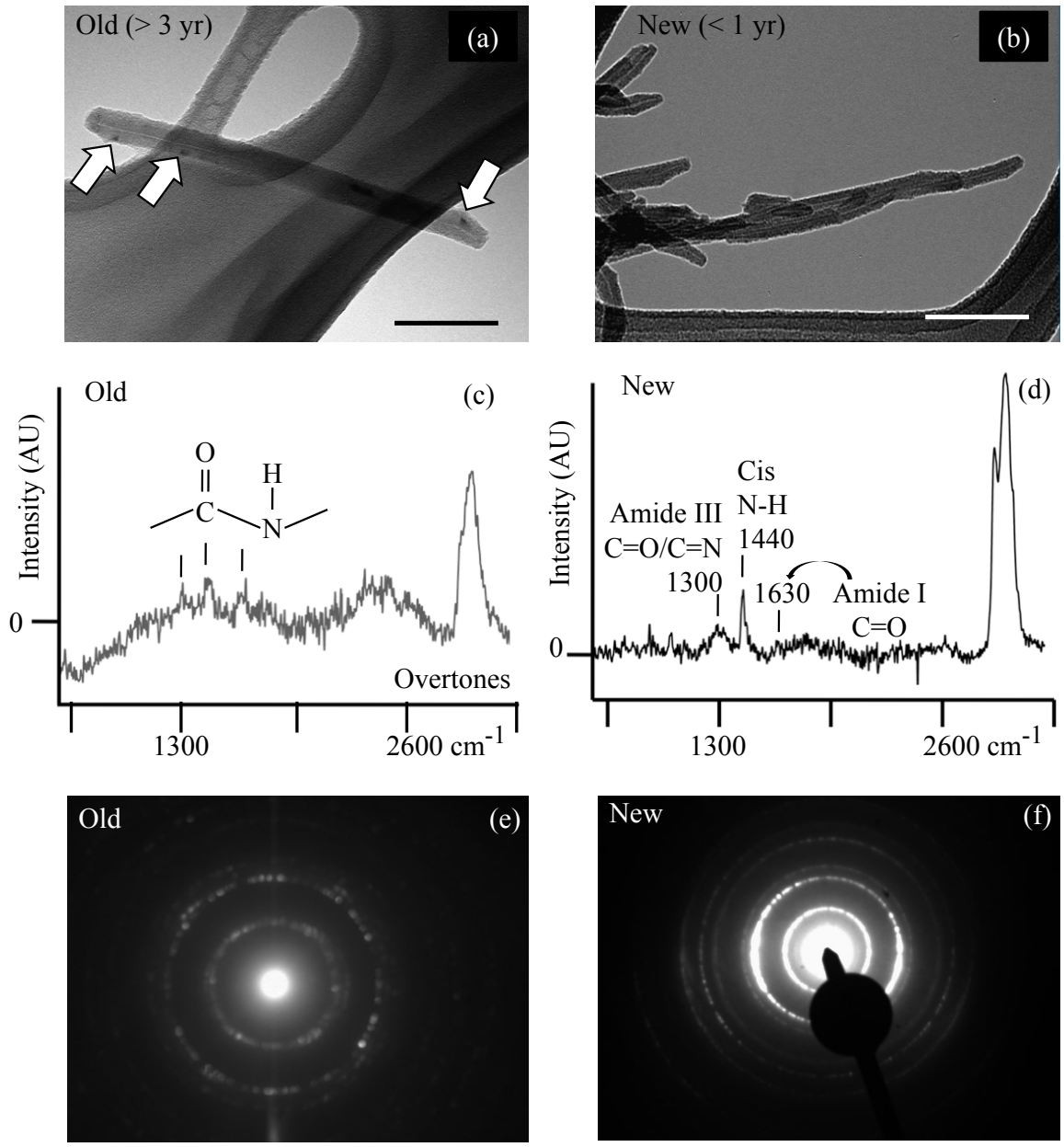

Figure 5.6: TEM, Raman spectroscopy, and SAED results of aged ((a), (c), and (e)) and new ((b), (d), and (f)) polyamide nanofibers. No structural differences were evident in TEM images of (a) aged and (b) new nanofibers. Arrows in the aged nanofibers (a) show dark contrast inclusions. Scale bars, 100 nm. Raman spectroscopy, given in (c) and (d), showed FWHM increases on the polyamide peaks and development of a broad disordered carbon peak for the > 3 yr samples (c). AU: arbitrary units. Both SAED in (e) and (f) showed demonstrated evidence of crystallinity within the nanofibers that were investigated. Directionality in SAED of new nanofiber (f) further indicates potential crystal texture. [67*].

5.6.2.3 AFM investigation of cerebellar granular neuron responses

High pass filtered AFM height images of CGNs are shown in Figure 5.7. The most frequently observed result for CGNs cultured on the aged (> 3 yr old) scaffolds was that the neurons burrowed beneath the scaffold (Figure 5.7 (a) and (b)). CGNs on aged scaffolds extended neurites as shown in Figure 5.7 (a). In contrast, CGNs cultured on the newly electrospun (< 1 yr old) scaffolds were clustered and lacked neurite outgrowth (Figure 5.7 (c)).

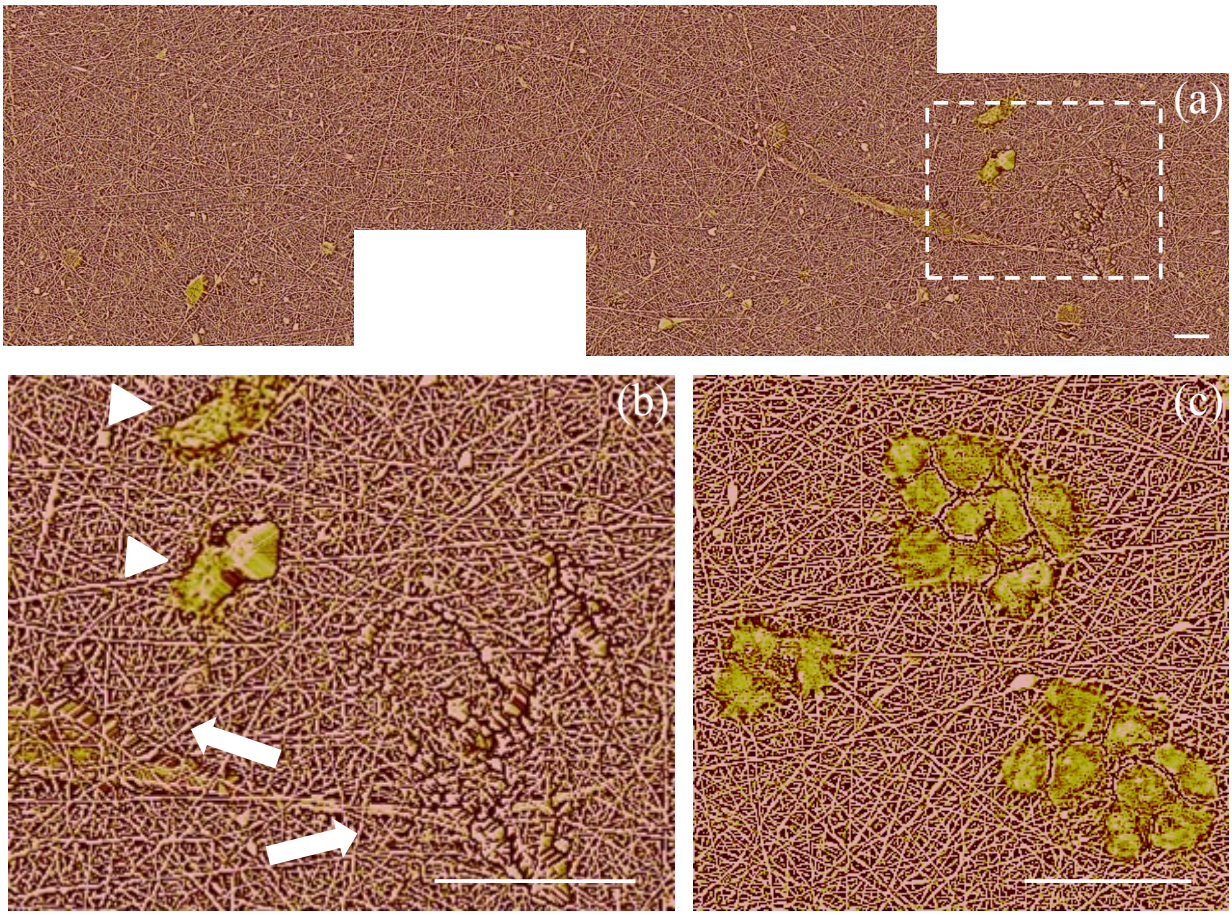

Figure 5.7: A composite AFM image (a) shows the burrowing response of a cerebellar granular neuron (CGN) on aged (> 3 yr old) nanofibrillar scaffolds. The neurite length is approximately 0.5 mm. The close-up of the dashed box in (a) as shown in (b) shows that the neurons with associated neurite outgrowth are underneath the nanofibers (arrows). Arrow heads show cell debris or some CGN which lacked neurite. (c) Neurons cultured on new nanofibers clustered on the top and lacked neurite outgrowth. Scale bars, 20 μm. [67*].

5.6.3 Discussion

This study demonstrated that the age of tissue scaffolds affects CGN migration and neurite outgrowth. Careful investigation of the nanofibrillar layers on the Aclar surfaces, after the burrowing response was observed, showed no obvious breaks. The neurons were therefore strongly driven to reach a three-dimensional environment, either by penetrating through the nanofiber meshes or by infiltrating between the nanofiber and the Aclar layers at their edges and then migrating considerable distances (0.5-1.0 mm) to reach some of the regions investigated by AFM. Contact angle measurements showed that there was a measurable difference in the surface polarity of new and aged scaffolds. Raman spectroscopy results confirmed the degradation of the basic polyamide chemistry over time. The dark contrast inclusions identified by arrows in Figure 5.5 (a) were noted in all of the aged samples. Similar inclusions were not observed in any of the new samples.

The experimental results suggest that local crystallization may be present both in the aged and new nanofibers (Figure 5.5). Facilitation of neuron growth cone development into axons on hydrogel matrices with compliances comparable to those of brain tissue (100-400 Pa, considered soft) has been reported [72]. It was further reported [72] that neuron single cultures grew *only* on soft hydrogels, which suggests a strong response to the mechanical environment. In the present study, healthy neuron morphologies with neurite outgrowth were observed in association with the aged scaffolds while non-process-bearing morphologies were observed on the new scaffolds. The properties of the aged nanofibrillar scaffolds evoked a response in neurons, which burrowed into a more three-dimensional environment and showed neurite outgrowth.

Chapter 6

The Effect of Nanophysical Properties on Untreated and dBcAMP-treated Astrocyte Differentiation

In this chapter, the effect of tissue scaffold nanophysical properties on the untreated and dBcAMP-treated astrocytes was investigated. The purpose of the untreated and dBcAMP treated astrocytes were to obtain astrocytes like quiescent and reactive astrocytes in vivo. The promising results of polyamide nanofibrillar scaffolds motivated the investigation of reactive-like astrocyte differentiation in response to the external physical cues provided by the nanofibrillar scaffolds and additional comparative culture surfaces. The four substrates were used in the present study: (1) the electrospun polyamide nanofibrillar scaffolds and three comparative culture surfaces, (2) poly-L-lysine (PLL) functionalized glass, (3) PLL functionalized Aclar, and (4) unfunctionalized Aclar. These scaffold environments themselves present an array of potentially directive physical properties.

6.1 Nanofibrillar scaffolds induce preferential activation of Rho GTPases in cerebral cortical astrocytes

Astrocytes cultured on electrospun polyamide nanofibers whose nanophysical properties may reproduce key aspects of native extracellular matrices have demonstrated promising results in both in vitro and in vivo situations. In vitro, astrocytes cultured on nanofibrillar scaffolds assumed morphologies that appeared to recapitulate those observed in native tissues.

Furthermore, autocrine up-regulation of FGF-2 was demonstrated by Western blot, along with increased neurite outgrowth by co-cultured neurons [10]. In vivo, the same scaffolds introduced into spinal cord wound sites promoted accelerated hindlimb recovery measured by standardized observational scoring (Beattie, Basso, Breshnahan – BBB score) with aligned and fasciculated axon development and re-vascularization throughout wound sites [37, 38]. Furthermore, low levels of astrocytic scarring were observed at three and five weeks after injury in comparison to injury-only controls, with reduced levels of glial fibrillary acidic protein, a marker for reactive astrocytes, and chondroitin sulfate proteoglycans, a group of molecules expressed by both glial and fibroblastic components of a glial scar and believed to be inhibitory to axonal regrowth [73, 74]. The in vitro and in vivo results suggest that nanofibrillar scaffolds could induce preferential astrocyte differentiation leading to minimized glial scar formation. Attenuation of scarring may be due to the nanofibrillar nanostructure that closely resembles features of naturally occurring extracellular matrix/basement membrane scaffolds and may therefore cause the nanofibers to look like 'self', or to the nanofibrillar chemistry, or to both. It is therefore important to investigate the physical properties of the nanofibrillar environment and to elucidate their directive effects on neural cell responses.

The present research explores the hypothesis that external physical cues of the nanofibrillar scaffolds can trigger the initiation of specific signaling cascades with morphological consequences. The external physical cues of surface polarity and surface roughness were investigated in this study. Previous investigations suggested that surface polarity might be an influential parameter of neural cell responses [75]. Because the macroscopic surface roughness introduced by the nanofibrillar scaffolds differed significantly from previous investigations [76, 77], this parameter was also considered. Additionally, new nanoscopic investigations of surface

roughness were performed. Contact angle measurements were used to assess surface polarity and AFM was used to investigate both macroscopic and nanoscopic surface roughness.

In this research, the morphological response of cerebral cortical astrocytes to nanofibrillar scaffolds was investigated at high-resolution using AFM. The three dimensional capability of AFM was also used to characterize cell spreading. An initial study of the corresponding activation of GTPase upstream regulators was performed using immunocytochemistry. For each immunolabel, phalloidin staining of F-actin was also performed to allow assessment of colocalization with the cytoskeleton. The immunocytochemistry study focused on investigation of the main GTPase regulators for the observed morphological responses: filopodia, lamellipodia, and stress fiber formation, and stellation. Immunolabeling with Cdc42, Rac1, and RhoA was performed as these are upstream regulators of filopodia, lamellipodia, and stress fiber formation, respectively [78, 79]. Inhibition of the RhoA effector kinase (ROCK) through depression of RhoA is one pathway that is associated with the cessation of stress fiber formation and the onset of stellation [80].

As only external cues were used to trigger cell responses, astrocyte responses to nanofibrillar surfaces were studied in comparison with their responses to three additional culture surfaces: poly-L-lysine-functionalized planar glass (PLL glass), unfunctionalized planar Aclar (Aclar), and PLL-functionalized planar Aclar (PLL Aclar). PLL glass is a standard astrocyte culture surface, and astrocyte responses to it are well characterized [1]. The polyamide nanofibrillar scaffolds were electrospun on Aclar substrates; therefore, astrocyte responses to Aclar surfaces were investigated to distinguish responses to the nanofibrillar scaffolds from possible responses to the underlying Aclar substrate. Astrocyte responses to PLL Aclar surfaces were studied to clarify the role of the underlying substrate versus surface functionalization.

The results of the morphological investigations and immunocytochemistry experiments consistently indicated that preferential activations of Rho GTPases were induced by the variations in the physical environments. These were directive for specific cell morphologies and responses.

6.1.1 Material and methods

6.1.1.1 Nanofibrillar Scaffolds

Polyamide (proprietary blend) nanofibers (median diameter ~180 nm) were electrospun from a blend of two polymers [$(C_{28}O_4N_4H_{47})_n$ and $(C_{27}O_{4.4}N_4H_{50})_n$] onto Aclar coverslips by Donaldson Co., Inc. (Minneapolis, MN) [81]. The resulting non-woven polymeric nanofibrillar scaffold was approximately 2 μm thick when measured on edge by optical microscopy. The matrix comprised approximately ten layers of randomly oriented nanofibers and appeared to be uniformly dense, with ~25 nanofiber segments per 5x5 μm^2 scan area per surface layer when measured by AFM [10] and no direct openings to the coverslip surface. Astrocytes could attach to the nanofibrillar surfaces but not migrate into them. The nanofibrillar scaffolds in the present study were not chemically modified.

6.1.1.2 Planar Culture Surfaces

Glass coverslips (12 mm, No. 1 coverglass, Fisher Scientific, Pittsburgh, PA) and Aclar coverslips (Ted Pella, Redding, CA) were used as underlying planar substrates. Glass or Aclar coverslips were placed in a 24-well tissue culture plate (one coverslip/well) and covered with 1

ml of PLL solution (50 μg PLL/ml in dH_2O) overnight. The coverslips were then rinsed with dH_2O, sterilized with UV light, and used for the cultures. One set of Aclar coverslips was left unfunctionalized.

6.1.1.3 Primary Astrocyte Culture

Purity-enhanced cultures of primary astrocytes were established as previously reported [10, 37, 38]. All procedures were approved by the Rutgers Animal Care and Facilities Committee (IACUC Protocol #02-004). This includes a number of steps taken to assure the purity of the primary astrocyte cultures. Briefly, rat cerebral cortical astrocytes were prepared from postnatal day P2 Sprague Dawley rats and grown to confluence in astrocyte medium in 75 cm^2 tissue culture flasks. This enhances astrocyte purity because, after birth, the neurons in the cerebral cortex are post mitotic and do not grow in tissue cultures (tissue for culturing cortical neurons tissue is obtained from embryos). Astrocyte medium was composed of Dulbecco's Modified Eagle's Medium (DMEM, Invitrogen, Carlsbad, CA) + 10% fetal bovine serum (Invitrogen), 1% penicillin and streptomycin (Sigma-Aldrich, St. Louis, MO), which does not support growth of primary, dissociated neurons in culture. Cultured astrocytes were then harvested with 0.5% Trypsin/EDTA (Sigma-Aldrich) and re- seeded at a density of 30,000 cells/well directly on 12 mm Aclar or PLL Aclar coverslips, PLL glass coverslips, or on Aclar coverslips coated with nanofibers in 24 well trays in astrocyte medium (0.5 ml), and then stained for F-actin, Cdc42, Rac1 and RhoA. The sub-culturing processes further purified the primary cultures. Parallel cultures were immunostained with GFAP, a marker for astrocytes, and more than 95% were found to be GFAP positive.

6.1.1.4 Contact Angle Measurements

Contact angle measurements of culture surfaces were acquired using VCA Optima contact angle analysis equipment (AST Products Inc., Billerica, MA). Two samples from each set of culture surfaces were analyzed by five randomly selected measurements from each sample. Variations in contact angle data among the culture surfaces were analyzed using ANOVA followed by pairwise post hoc comparisons with Tukey's test [82]. Significance levels were set at $P < 0.05$.

6.1.1.5 Optical Microscopy

Differential Interference Contrast (DIC) images (8 per substrate) using an Olympus Software FV10-ASW Version 03.01.02.02 (Olympus, Center Valley, PA) were captured to ensure that representative specimens were considered for AFM investigation. The 30,000 cell plating density versus the cell adhesion density for the individual substrates was also investigated.

6.1.1.6 Atomic force microscopy

AFM images of individual astrocytes at 24 h were acquired using a Veeco Instruments Nanoscope IIIA (Bruker AXS Inc, Madison WI, formerly Veeco Metrology) operated in ambient air. Three scanners were used as noted in the text: a J scanner with 125x125x5.548 μm x-y-z scan range, an E scanner with 13.5x13.5x3.08 μm x-y-z scan range and an A scanner with 1x1x0.66 μm x-y-z scan range. Both contact mode, using silicon nitride tips with a nominal tip radius of 20 nm and cantilever spring constant k = 0.58 N/m, and tapping mode, using silicon tips with a nominal tip radius of 10 nm and drive frequency of ~320 kHz, were used. The closed-loop Multimode scanner (iCXY100Z15-MM, nPoint Inc., Middleton, WI) with

100x100x15 μm x-y-extended z scan range was used in order to investigate astrocyte morphology on Aclar surfaces.

As the heights of the cellular processes investigated on the nanofibrillar scaffolds were on the same order as the background nanofibers, it was not possible to clearly distinguish them in conventional height, amplitude, or phase images. Frequency domain Gaussian high pass filtering (GHPF) was therefore used to segment the cellular extensions from the nanofibrillar background in height images [83]. AFM images of at least 30 astrocytes for each culture surface were evaluated to ensure that the results were representative. Astrocytes with having stellate morphologies were counted to obtain the percentage stellation for each cell culture used in this work using the sum criteria as previously reported [84]. Astrocytes having at least one process longer than the width of the cell soma were considered as stellate.

AFM surface roughness analysis of the scaffolds was performed by Nanoscope Software version 5.30r3.sr3. Square 1x1 μm^2 and 10x10 μm^2 regions were randomly selected, and five measurements were taken from each sample. The flatten command was used to remove the bow of the AFM height images. Surface roughness data along individual nanofibers were collected using SPRM [14, 51]. Variations in RMS surface roughness data among the culture surfaces were analyzed using ANOVA followed by pairwise post hoc comparisons with Tukey's test [82]. Significance levels were set at $P < 0.05$.

6.1.1.7 Antibody and F-actin staining of astrocytes

The astrocytes cultured on coverslips were fixed with 4% paraformaldehyde for 10 minutes, permeabilized with 0.5% Triton X-100 for 5 minutes, and blocked with 10% normal goat serum

for 30 minutes. After removing the normal goat serum, the cells were double stained with one of the primary antibodies mouse anti-Cdc-42 (1:200), mouse anti-RhoA (1:200), or mouse anti-Rac1 (1:25) (all from Cytoskeleton, Denver, CO)), and phalloidin (Invitrogen, Carlsbad, CA). The incubation in the primary antibodies was done overnight at room temperature in a humidity chamber. Coverslips were then washed with phosphate buffered saline (PBS) and stained with goat anti-mouse Alexa 568 IgG secondary antibody (ex 579 nm, em 603 nm, Invitrogen) at a 1:500 dilution for 1 hour. Following the antibody staining the cells were rinsed, stained with Phalloidin-488 (ex 498 nm, em 520 nm, Invitrogen) at a 1:100 dilution for 1 hour, mounted on microscopic slides with GelMount (Biomeda, Foster City, CA), and observed under an Olympus IX81 inverted microscope (Olympus, Center Valley, PA).

6.1.1.8 Image Capture Conditions for Immunocytochemistry Structural Investigation

A first set of six representative projection images for each substrate and immunolabeling condition: Cdc42, Rac1, RhoA, each with corresponding phalloidin staining, were captured using fluorescence microscopy, at scales and pixel resolutions that gave optimal representation of structural features (72 cells total).

6.1.1.9 Image Capture Conditions for Protein Expression Estimate

A second set of maximum intensity level grayscale images were captured specifically for protein estimation. These had identical scale bars and pixel resolutions as required for accurate comparative analysis of activation intensity patterns. Five images (via 20X objective) were captured for each of the three antibodies on each of the four culture surfaces. At this

magnification, each image typically continued several whole cells and a total of 240 cells were investigated. Images of the astrocyte cultures were captured using Metamorph software (Molecular Devices Sunnyvale, CA). For each condition, a minimum of five images was captured from different regions of three coverslips to ensure that the results were representative for the cultures as a whole. The amount of detected protein was quantified by selecting a constant rectangular region and measuring the total fluorescence intensity. The mean background intensities of the fluorescence images were calculated and then subtracted from the total fluorescence intensity value. ImageJ software version 1.44p was used for the quantitative analysis of light intensity. Intensity data were analyzed using ANOVA followed by pairwise post hoc comparisons with Tukey's test. Significance levels were set at $P < 0.05$.

6.1.1.10 Analysis of Cytoskeletal Colocalization

Colocalization analysis of RhoA and F-actin was performed on the first set of images using Olympus Software FV10-ASW Version 03.01.02.02 (Olympus, Center Valley, PA). A Pearson Coefficient (PC) measure of the colocalization of two proteins was calculated as [54]

$$r = \frac{\sum_i \left(F_{1,j} - \overline{F_{1,J}}\right).\left(F_{2,j} - \overline{F_{2,J}}\right)}{\sqrt{\sum_i \left(F_{1,j} - \overline{F_{1,J}}\right)^2 . \left(F_{2,j} - \overline{F_{2,J}}\right)^2}} \tag{6.1}$$

for six examples from each of the three combinations. $F_{1,i}$ is average brightness of wavelength λ_1 at i-th pixel, $F_{2,i}$ is average brightness of wavelength λ_2 at i-th pixel, $\overline{F_{1,J}} = \frac{1}{N}\sum_i F_{1,j}$

is average brightness of wavelength λ_1 and $\overline{F_{2,J}} = \frac{1}{N}\sum_i F_{2,j}$ is average brightness of wavelength λ_2.

Prior to the calculation of each PC, the background was removed by setting the threshold level manually subsequent to cell segmentation. Individual values were used to calculate a mean value PC ± standard deviation. All results met two separate reliability criteria: a mean PC value > 0.5 and a standard deviation of less than 25%.

6.1.2 Results

6.1.2.1 Contact Angle Measurement Results of Culture Surfaces

The hydrophobicity of tissue cultures has been suggested as a possible material property for reduced astrocyte growth [76]. In this work, the hydrophobicity of the PLL glass, nanofibrillar scaffolds, Aclar, and PLL Aclar surfaces were characterized by contact angle analysis (Figure 6. 1).

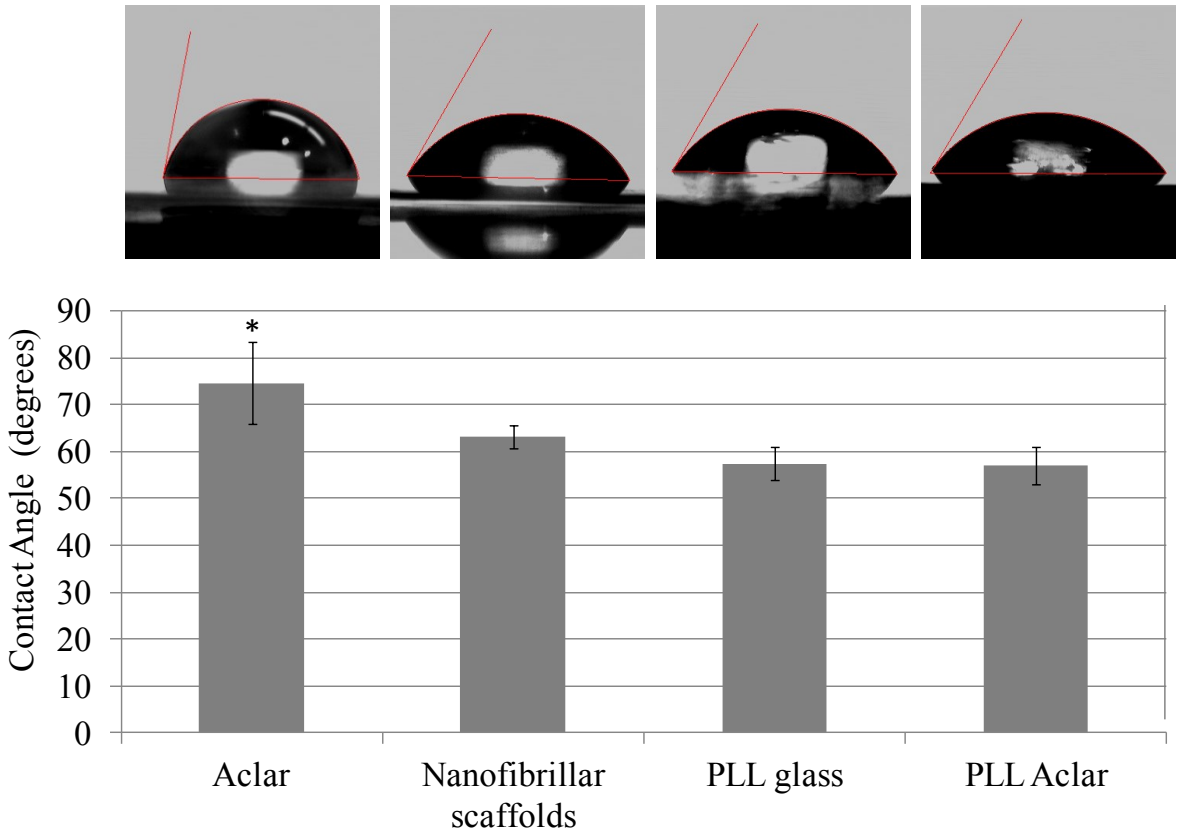

Figure 6.1: Contact angle measurements of culture surfaces. Aclar was significantly less hydrophilic than nanofibrillar scaffolds, PLL glass and PLL Aclar. No significant differences were identified from pairwise comparisons among the PLL Aclar, PLL glass, and nanofibrillar scaffolds. [12*].

The contact angle was significantly different among the different surfaces (ANOVA, P=0.0002). Post hoc pairwise comparisons with Tukey's test demonstrated that the contact angle on Aclar surfaces was significantly different than each of the other surfaces (max P=0.017). Aclar surfaces were significantly less hydrophilic than nanofibrillar scaffolds, PLL glass, and PLL Aclar surfaces.

6.1.2.2 AFM Surface Roughness Results

Surface roughness measured with AFM showed that two scales of surface roughness were present on the nanofibrillar surfaces: a large overall RMS roughness and a much smaller RMS

roughness along the nanofibers (Figure 6.2). The overall nanofiber roughness was more than an order of magnitude greater than the roughness of any of the other surfaces (ANOVA, followed by post hoc pairwise comparisons with Tukey's test, all $P<0.0001$). A separate analysis followed by pairwise comparisons of the surface roughness among PLL glass, PLL Aclar, and Aclar surfaces indicated that each was different than the other (max $P=0.0111$).

SPRM [14, 51] was used to investigate the surface roughness along individual nanofibers. SPRM AFM data was obtained by raster-scan auto-tracking along individual nanofibers. The RMS surface roughness was calculated on each pixel based on a local neighborhood region, after curvature removal by Kasa circle fit [85]. The local neighborhood region was a rectangular box around each pixel whose box size was set to be close to the nanofiber diameter. Multiple sets of overlapping surface roughness information were generated, with the provision that any box that extended outside the nanofiber boundaries was automatically truncated. Based on a sampling of over 1000 data points from multiple nanofibers, the mean value of the RMS surface roughness along the individual nanofibers was midway between the values for PLL glass and Aclar. The AFM surface roughness results therefore indicated that the nanofibrillar surfaces had significantly higher RMS surface roughness at the macroscopic level but lower RMS surface roughness at the cell receptor level with values that were comparable to those of PLL glass. Representative high-resolution A-scanner AFM height images of the four surfaces are shown in Figure 6.2 (a-d) and the mean values for RMS surface roughness ± standard deviation are shown in Figure 6.2 (bottom).

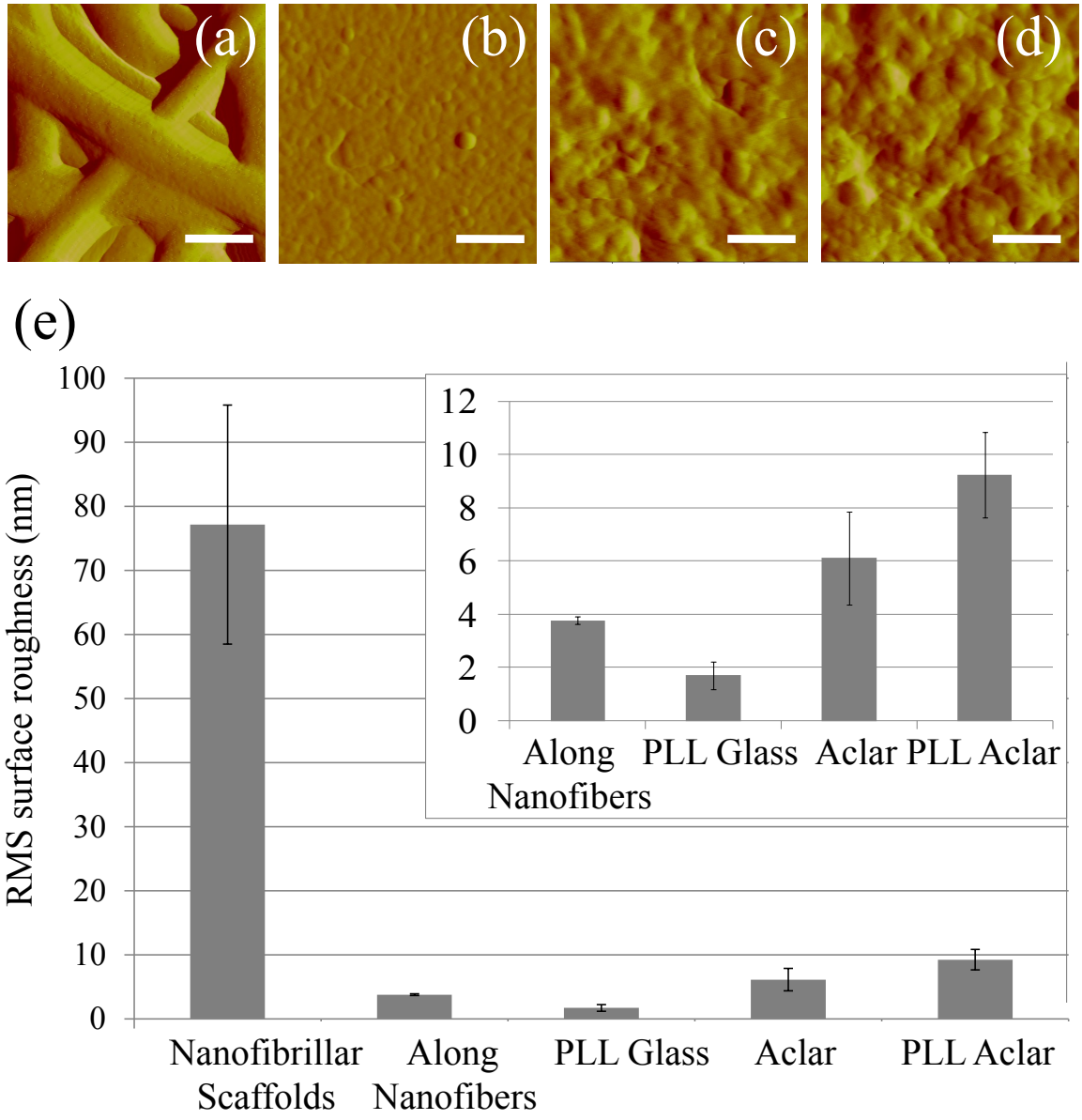

Figure 6.2: AFM surface roughness investigation of culture surfaces. High-resolution AFM deflection images of (a) nanofibrillar scaffold, (b) PLL glass, (c) Aclar, and (d) PLL Aclar by an A scanner. Scale bars, 250 nm. RMS surface roughness measurement results (e) of nanofibrillar scaffolds, along nanofibers, PLL glass, Aclar, and PLL Aclar. The mean RMS surface roughness measurements showed that nanofibrillar scaffolds had the highest surface roughness but surface roughness along individual nanofibers was comparable to the planar surfaces (inset (e)). Error bars show the standard deviation. [12*].

6.1.2.3 Optical Microscopy Survey of Astrocyte Morphology and Cell Density

Differential Interference Contrast (DIC) images (8 per substrate) were captured to ensure that representative specimens were considered for AFM investigation. The results shown in Figure 6.3 indicated that relatively homogeneous populations of astrocytes with different morphologies were present on each substrate. The 30,000 cell plating density versus the cell adhesion density for the individual substrates was also investigated. The mean value results in cells per mm^2 were: PLL glass: 86; nanofibrillar scaffolds: 56; Aclar: 90; and PLL Aclar: 91. It is noted that DIC and brightfield images were unable to resolve the cell morphologies of astrocytes on nanofibrillar scaffolds (Figure 6.3 (b)). This is because the cellular edges and processes are approximately the same order in height as the background nanofibers, ~100 to 200 nm. As discussed in Chapter 7, this issue was resolved for corresponding AFM images. The adhesion density for astrocytes on nanofibrillar scaffolds was therefore estimated from GHPF AFM images.

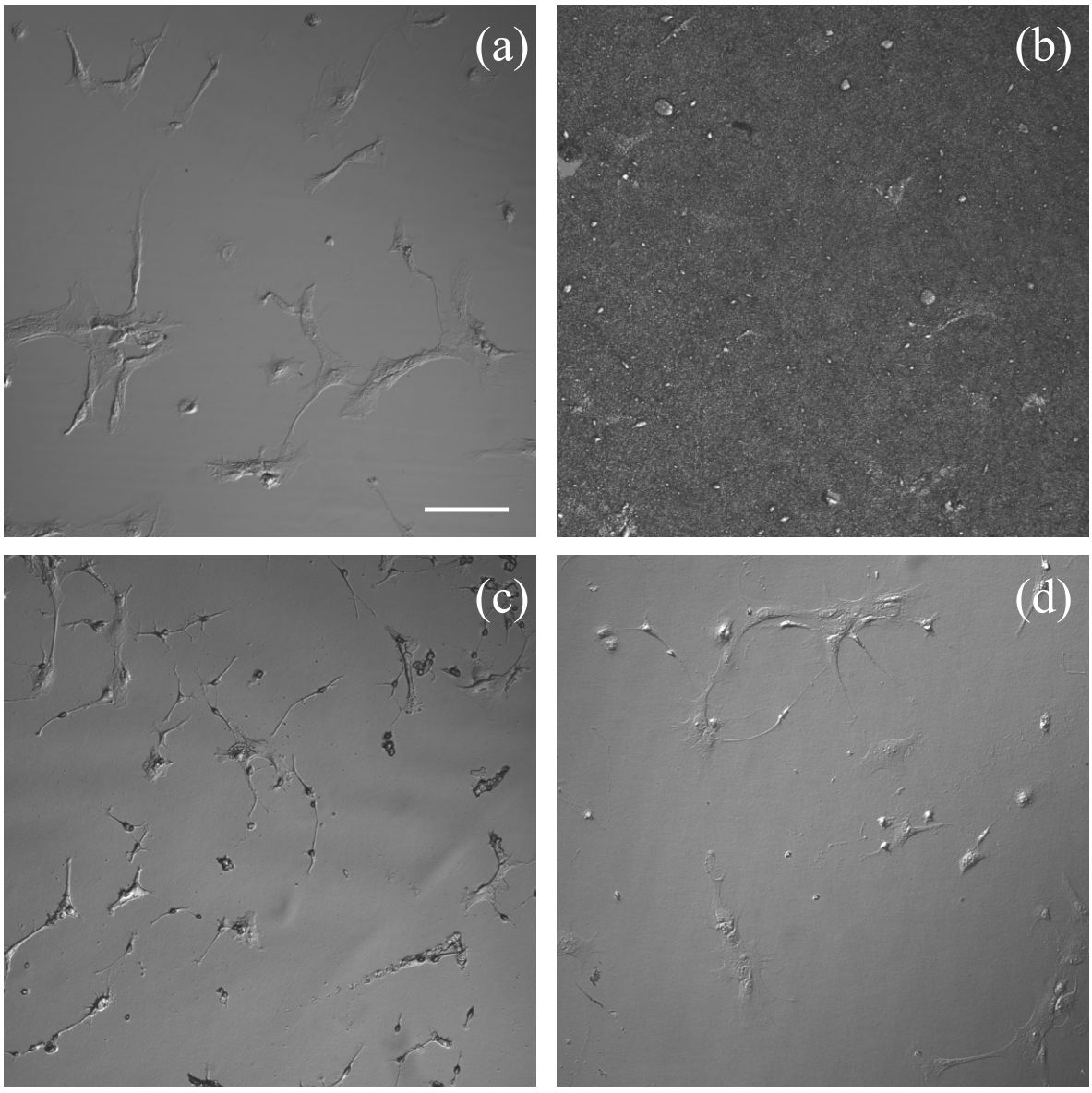

Figure 6.3: DIC images of astrocytes cultured on (a) PLL glass, (b) nanofibrillar scaffolds, (c) Aclar, and (d) PLL Aclar. Scale bar, 100 μm. [12*].

6.1.2.4 Astrocyte Responses to Poly-L-lysine-functionalized Glass Surfaces

Different stages of attachment and growth were observed simultaneously at 24 h, as shown in the representative seven-member group shown in Figure 6.4 (a). Most cells had lamellipodial vertices, suggesting activation of Rac [86]. Fan-shaped astrocytes were also observed; this is a morphological indicator of a migratory phenotype via lamellipodial leading edges [87]. Cell

clusters were observed, such as shown in the upper left. Potentially apoptotic cells were occasionally observed, as shown in the lower right. Close-ups of areas marked by arrows in Figure 6.4 (a) show details of: (b) a lamellipodial migration leading edge, with stress fibers evident; (c) filopodial anchor spikes; and (d) interacting lamellipodia between two cells.

AFM profile measurements of cell soma typically showed well-delineated nuclear and cytoplasmic regions. Representative section measurements across cells (along the dotted lines of Figure 6.4 (a)) are shown in Figure 6.4 (e-f). Nuclear regions in these desiccated samples had maximum heights of 0.5-1.0 μm.

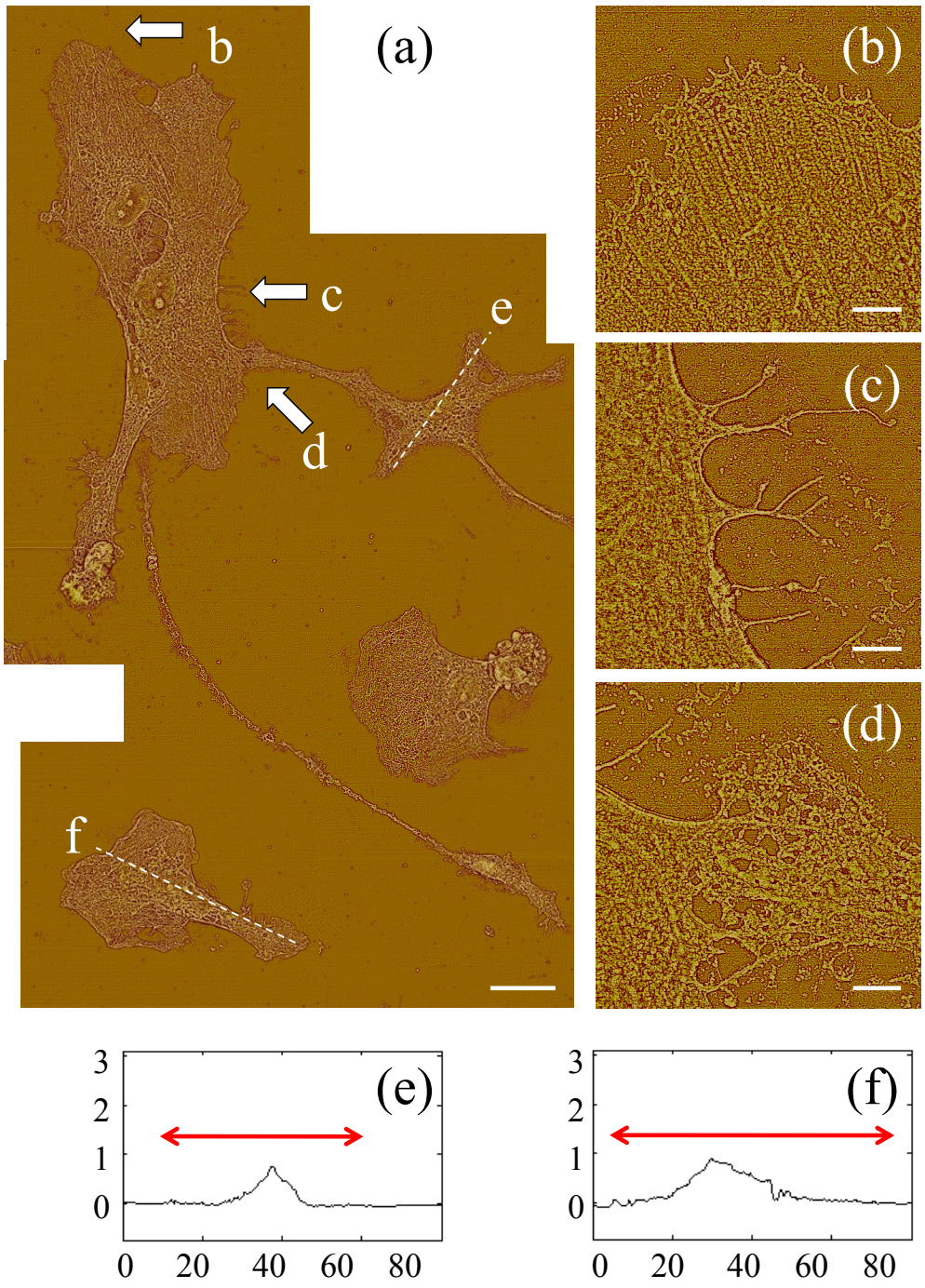

Figure 6.4: AFM astrocyte morphology investigation on PLL glass. (a) AFM high pass filtered composite height image of astrocytes by J scanner show lamellipodia formation (scale bar, 20 µm). (b–d) Close-ups by E scanner of arrow regions a–d shown in (a): stress fibers (b); filopodia anchors (c); and cell–cell interaction (d) (scale bars, 2 µm). (e and f) Cross-section profiles of cells e and f in (a). Axis units are in µm with astrocyte soma extent identified by red arrow. [12*].

6.1.2.5 Astrocyte Responses to Nanofibrillar Scaffolds

Astrocyte responses to the nanofibrillar scaffolds were different from those observed for PLL glass. Astrocytes cultured on nanofibrillar surfaces typically had stellate morphologies, as shown in the composite AFM images of Figures 6.5 (a) and 6.6 (a). Also, for most cells at 24 h, one vertex had developed into a process that traversed most or all of the distance to a neighboring cell as shown in Figure 6.5 (a). AFM section measurements of cell somata showed well-delineated nuclear regions about 1-2 μm in height with elevated perinuclear regions [84]. Representative profiles taken along the dotted lines in Figure 6.5 (a) are shown in Figure 6.5 (b-d).

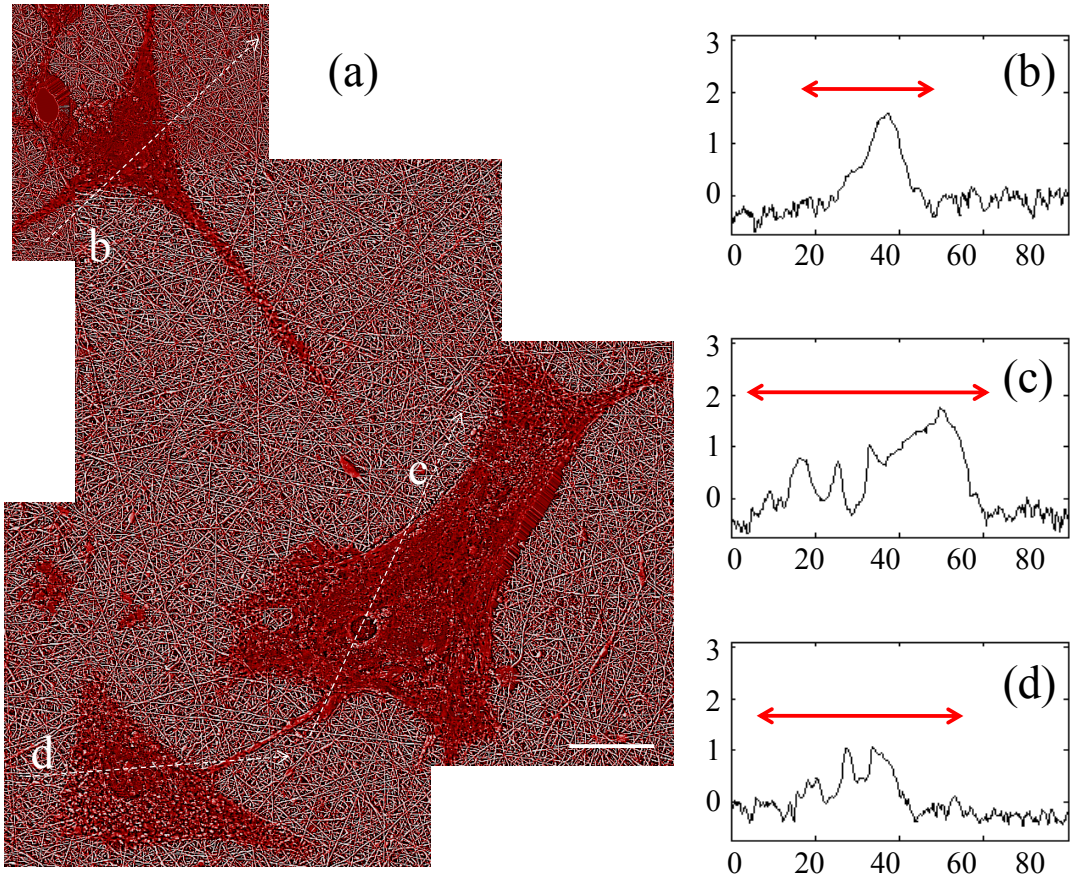

Figure 6.5: AFM astrocyte morphology investigation on nanofibrillar scaffolds. (a) AFM GHPF composite height image of astrocytes cultured on nanofibrillar surfaces by J scanner. Scale bar, 20 µm. (b–d) Cross section profiles of cells b–d in (a). Axis units are in µm with astrocyte soma extent identified by red arrow. [12*].

Process-mediated cell-cell interactions appeared to result from contacts between neighboring cells. Multiple examples of process growth were studied with the following observations. Processes typically tapered to ~1 µm wide and ~100 nm tall at their narrowest points and then developed broadened tips (~8-15 µm wide) within about 5 µm of a neighboring cell, as shown by the interacting cell pair in Figure 6.6. Ribbon-like elongations from the broadened tips formed the actual physical contact to the neighboring cell. In the example shown in Figure 6.6, the ribbon-like structures are visible on the top surface of a neighboring cell (boxed region Figure 6.6 (a) and its close-up (b)); in other cell-cell interactions, they extended across an open gap to

contact a cell at their tips. Interdigitating, 10 nm-diameter villar-like structures were typically observed near the contacted region as shown in Figure 6.6 (c), which is a close-up image of the boxed region in Figure 6.6 (b).

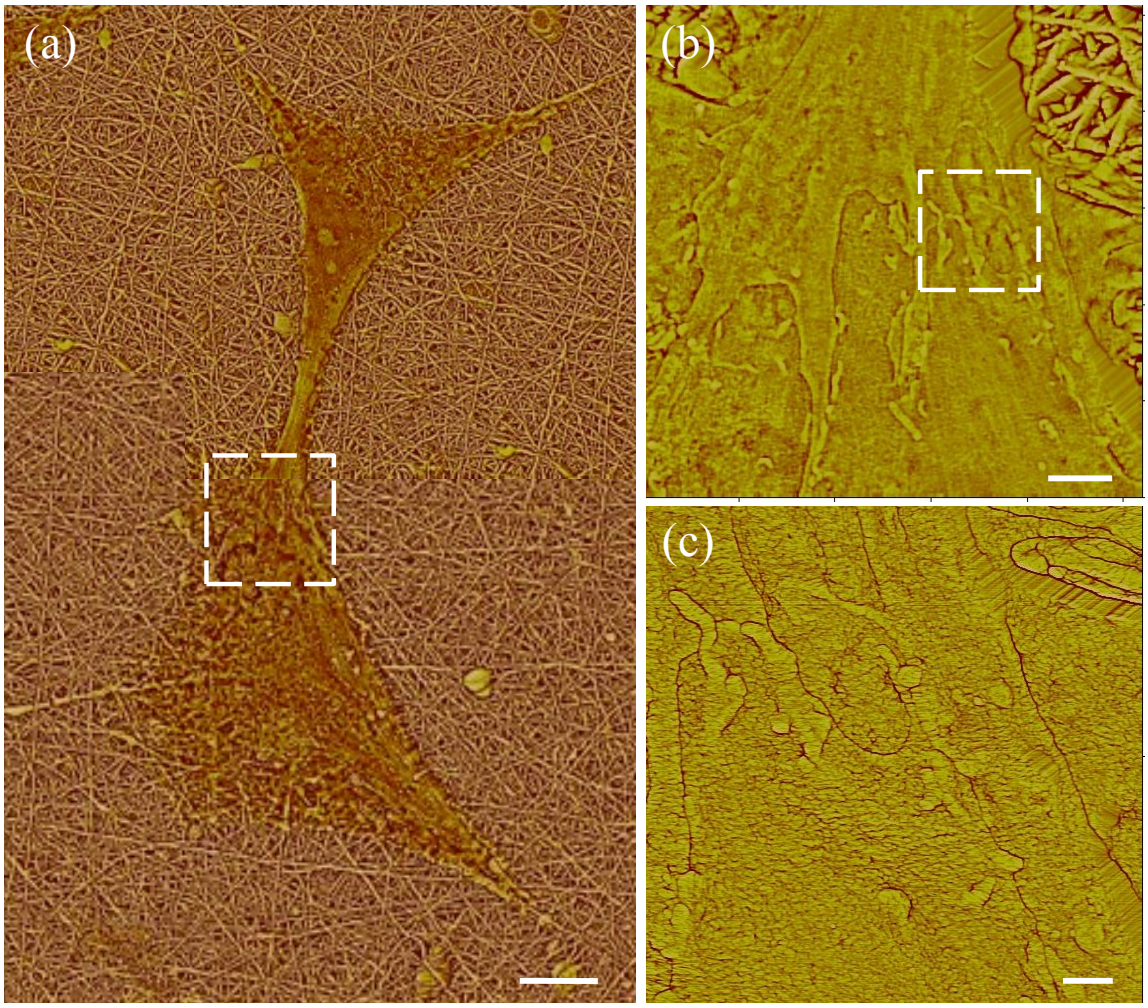

Figure 6.6: AFM high pass filtered composite height images of astrocytes cultured on nanofibrillar scaffolds. (a) Dashed box identifies the intercellular connection. (b) Close-up of the intercellular connection by E scanner. Dashed box identifies a contacted area. (c) Close-up of a contacted area by E scanner. The scale bars show 10, 2, and 0.5 μm in (a), (b), and (c), respectively. [12*].

6.1.2.6 Astrocyte Responses to Unfunctionalized Aclar Planar Surfaces

Astrocyte responses to the Aclar surfaces were different from those observed for both PLL glass and nanofibrillar scaffolds. Extensive networks of astrocyte processes about 100-150 nm in diameter were observed between astrocytes, as shown in the composite AFM image of Figure 6.7 (a). The three dimensional AFM investigation demonstrated that the cell somata were not well spread, as shown in the representative section measurements of Figure 6.7 (b-d), taken along the dotted lines in Figure 6.7 (a). Maximum somata heights frequently exceeded 3 μm, requiring use of an extended z-range scanner.

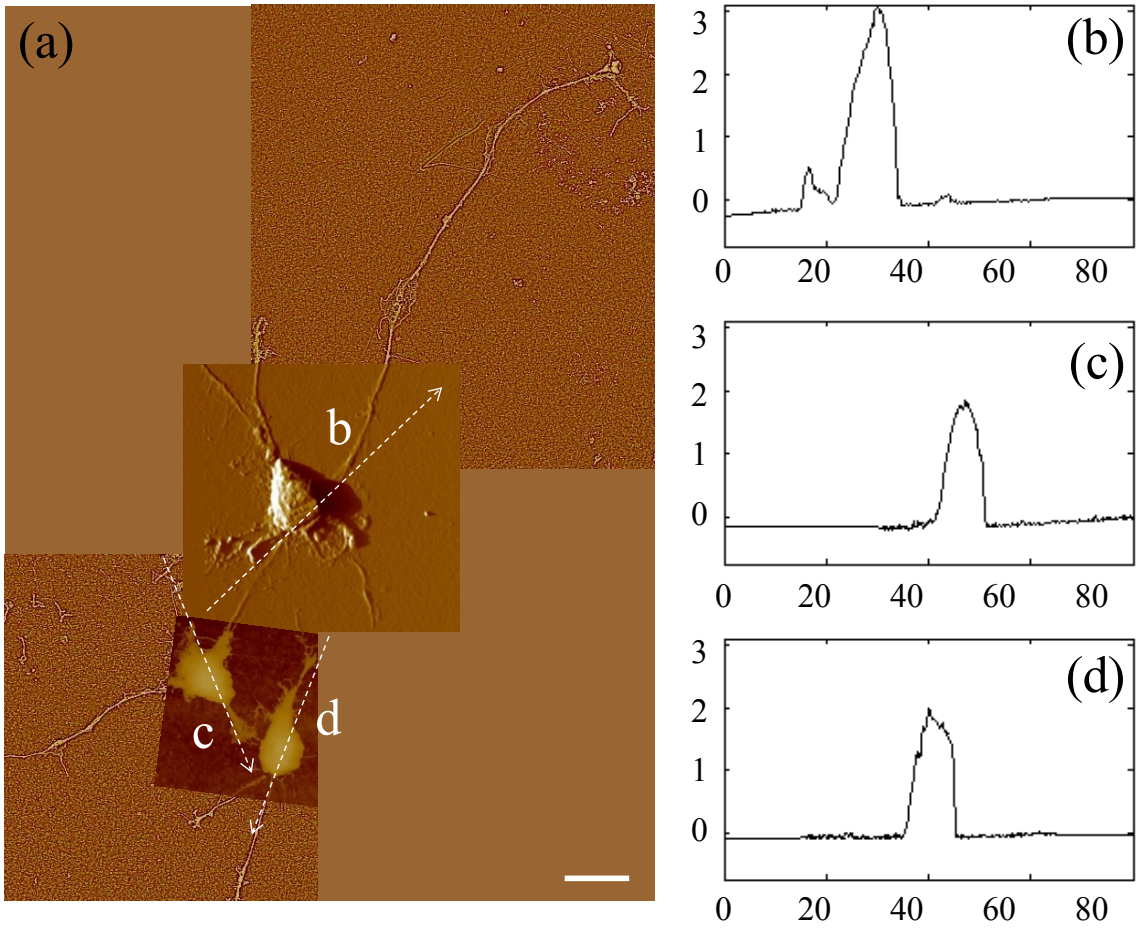

Figure 6.7: (a) AFM GHPF composite height image of astrocytes cultured on Aclar surfaces by J scanner. The cross sections shown by b–d in (a) were given in corresponding section profiles. Scale bar shows 20 µm and axis units are in µm. [12*].

6.1.2.7 Astrocyte Responses to PLL functionalized Aclar Planar Surfaces

PLL functionalization of Aclar surfaces induced astrocyte behavior similar to that observed for cells cultured on PLL glass. Astrocytes were once again observed in clusters as shown in Figure 6.8 (a) and were well spread. The typical heights of the well-defined nuclear regions were also similar, 0.5-1.0 µm, as shown in Figure 6.8 (b-c). The chief difference between the astrocyte responses to PLL Aclar versus PLL glass was the increased cell edge interaction with the substrate. High resolution AFM investigation of cell edges revealed branched structures that

appeared to infiltrate along the valleys created by the surface roughness, as shown in Figure 6.8 (d).

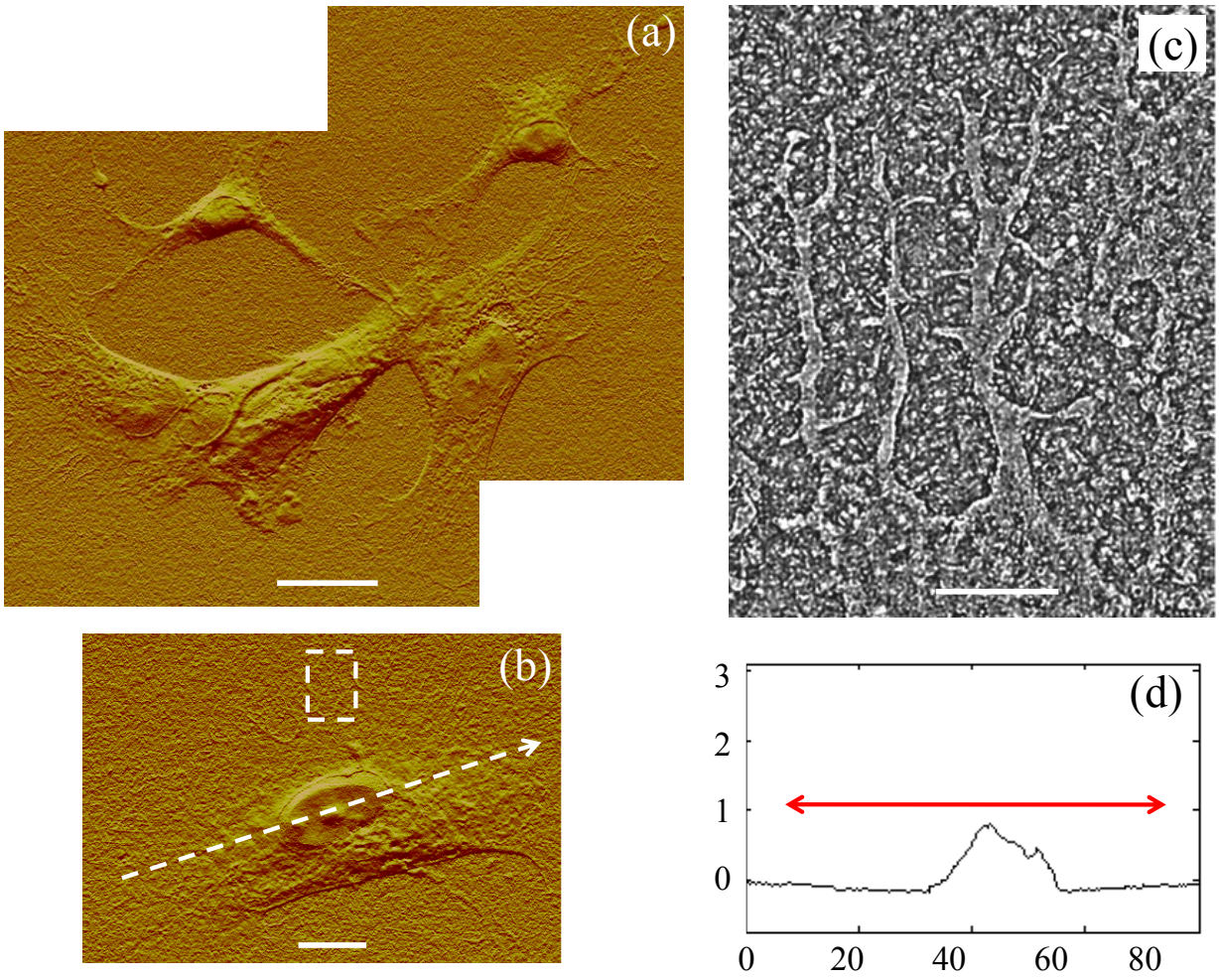

Figure 6.8: AFM investigation of astrocytes cultured on PLL Aclar surfaces. (a) Composite AFM deflection image of astrocytes by J scanner. Scale bar, 20 µm. (b) AFM deflection image of an astrocyte by J scanner. Scale bar, 10 µm. Dotted arrow identifies cross section. Dashed box identifies a cell edge. (c) Corresponding cell edge showing nanoscale filopodia by E scanner. Scale bar, 2 µm. (d) Corresponding cross section profile. Axis units are in µm with astrocyte soma extent identified by red arrow. [12*].

6.1.2.8 AFM-based Assessment of Astrocyte Stellation Response

A stellation response, defined as in Cox et al. as the development of a process longer than the cell body, was assessed based on AFM images of 35-45 cells per each culture surface. Use of the

GHPF as described in Tiryaki et al. enabled accurate assessment of process lengths on nanofibrillar surfaces [83]. The stellation responses based on GHPF AFM height images or on AFM deflection images are shown in Table 6.1. The highest percentage of stellate cells was found on the nanofibrillar scaffolds.

Table 6.1: Quantitative astrocyte stellation response results. [12*].

Cell substrate	# Cells	# Stellate cells	% Stellate
PLL glass	45	25	56
Nanofibrillar scaffolds	44	31	70
Aclar	35	20	57
PLL Aclar	36	15	42

6.1.2.9 Immunocytochemistry

Rac1, Cdc42, and RhoA are Rho GTPase family members that are involved in actin and microtubule dynamics [88, 89]. Cdc42 produces filopodial extensions [78], Rac1 induces lamellipodia formation and membrane ruffling [86], and RhoA causes actin bundles and focal adhesions in non-neuronal cells [90]. Kalman et al. have shown that Rac1 and RhoA GTPases induce growth of hippocampal astrocyte processes [91]. The four key morphologies observed in varying proportions on the different surfaces using AFM suggested preferential Rac1, Cdc42 and RhoA involvement. The expression of these GTPase proteins, as well as F-actin organization, was investigated with immunocytochemistry and phalloidin staining, respectively.

6.1.2.10 Immunocytochemistry Structural Investigation

An immunocytochemistry structural investigation was performed to investigate whether protein expression was generally consistent with the observed AFM morphology results. Six representative images for each substrate and immunolabeling condition were captured and studied, with typical results shown in Figure 6.9. From analysis of the phalloidin results, astrocytes on PLL glass displayed prominent stress fibers. Astrocytes on nanofibers displayed a stellate response with obviously less stress fiber formation. Astrocytes on PLL Aclar consistently displayed extensive filopodia formation. Astrocytes on Aclar appeared to display less filopodia formation; however, the full extent of the branched networks shown in Figure 6.9 consistently required AFM for observation. The phalloidin results of the immunocytochemistry structural investigation therefore generally supported the results of the AFM morphology study.

Analysis of the immunolabeling results suggested up-regulation of RhoA for astrocytes on PLL glass versus down-regulation of RhoA for astrocytes on nanofibers. It also indicated possible differences in the sequestration of the protein expression, i.e. whether the greatest intensity was observed near the cell periphery or the cell interior. A semi-quantitative protein expression estimate and a co-localization analysis were therefore performed to address these two points.

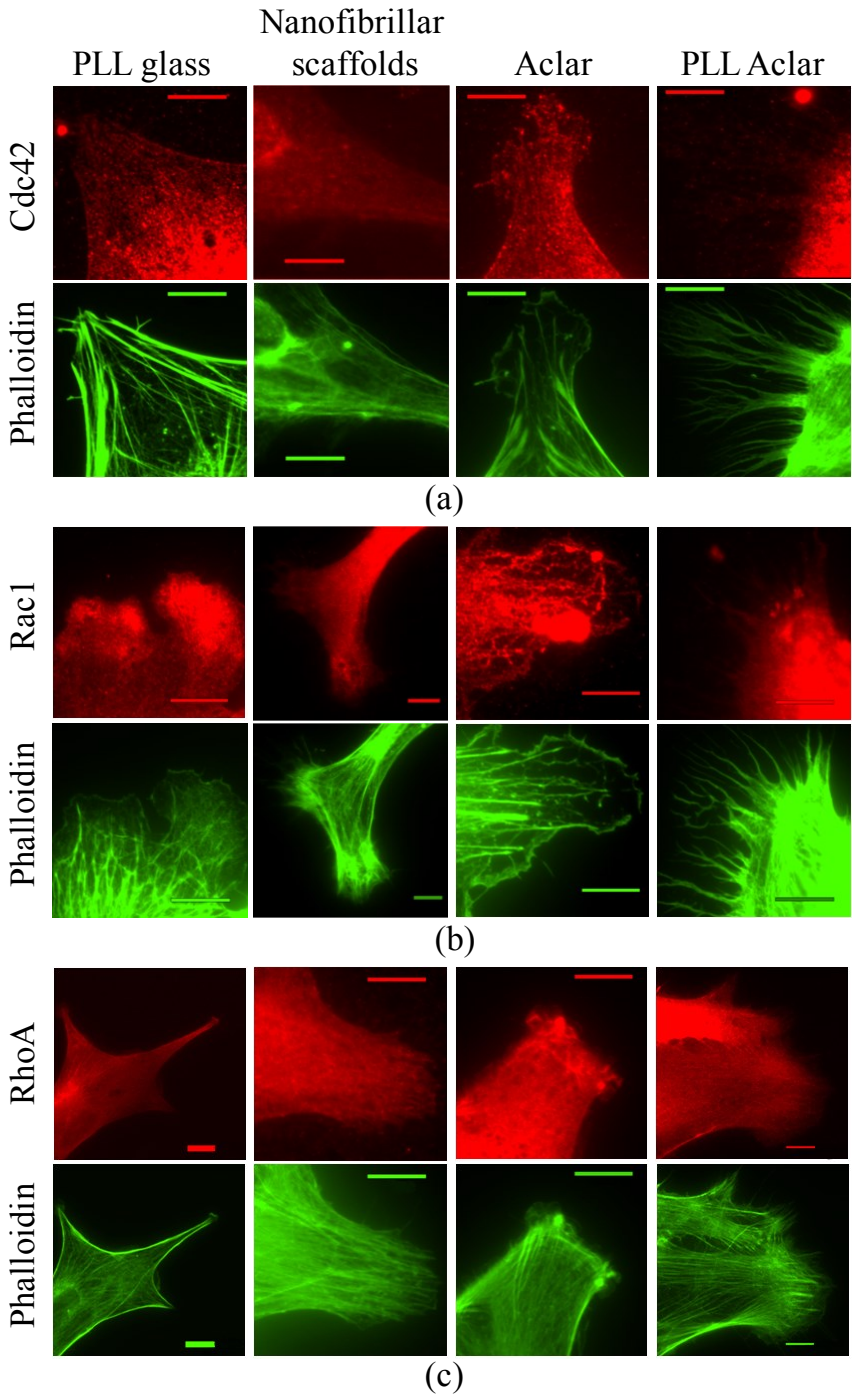

Figure 6.9: Immunocytochemistry structural investigation results. Left to right: fluorescence images of astrocytes cultured on PLL glass, nanofibrillar scaffolds, Aclar, and PLL Aclar substrates. Immunolabeling and corresponding phalloidin are represented in red and green, respectively. Astrocytes were labeled with (a) anti-Cdc42, (b) anti-Rac1, and (c) anti-RhoA. Scale bars, 10 µm. [12*]. Fluorescent images by I. Ahmed, Shreiber laboratory with analysis in this thesis.

6.1.2.11 Protein Expression Estimate

A protein expression estimate based on maximum intensity level images was performed. A second set of maximum intensity level grayscale images was captured specifically for quantification analysis and estimation. These had identical scale bars and pixel resolutions and were therefore accurate for the comparative analysis of activation intensity patterns. Twenty whole cell images (via 20X objective) for each of the three antibodies co-stained with phalloidin on each of the four culture surfaces were investigated using maximum intensity levels (240 cells total). The ImageJ software [92] free-hand tool was used to individually outline the area of each cell. ImageJ software was further used to calculate a mean intensity defined as the total intensity divided by the selected area. The results were compiled into an average mean intensity with standard error for each antibody type on each culture surface. The average mean intensities of the maximum intensity levels were used to investigate the activation intensity patterns for each surface.

The activation intensity patterns for Cdc42, Rac1, and RhoA are shown in Figure 6.10. For each surface, significant differences were observed in the intensity of immunostaining among Cdc42, RhoA, and Rac1 (ANOVA, max $P = 0.023$), which regulate actin dynamics and cell adhesion. For astrocytes cultured on PLL glass, post hoc analysis with Tukey's test revealed that the intensity of RhoA labeling was significantly greater than Cdc42 ($P = 0.0005$) and Rac1 ($P = 0.0289$). Labeling of Cdc42 and Rac1 were not statistically different ($P = 0.366$). For astrocytes cultured on nanofibers, the intensity of Cdc42 immunolabeling was significantly greater than RhoA ($P = 0.0154$). No significant differences were detected between Cdc42 and Rac1 ($P = 0.663$) or Rac1 and RhoA ($P = 0.120$).

For astrocytes cultured on Aclar, Cdc42 immunolabeling was significantly greater than Rac1 (P=0.041). No differences was observed in labeling of Cdc42 and RhoA (P=0.995). Large differences were observed between Rac1 and RhoA expression on Aclar, but the P-value following Tukey's test (P=0.051) did not reach the significance threshold of P<0.05. For cells cultured on PLL Aclar, the intensity of each immunolabel was significantly different from the other two (max P= 0.001).

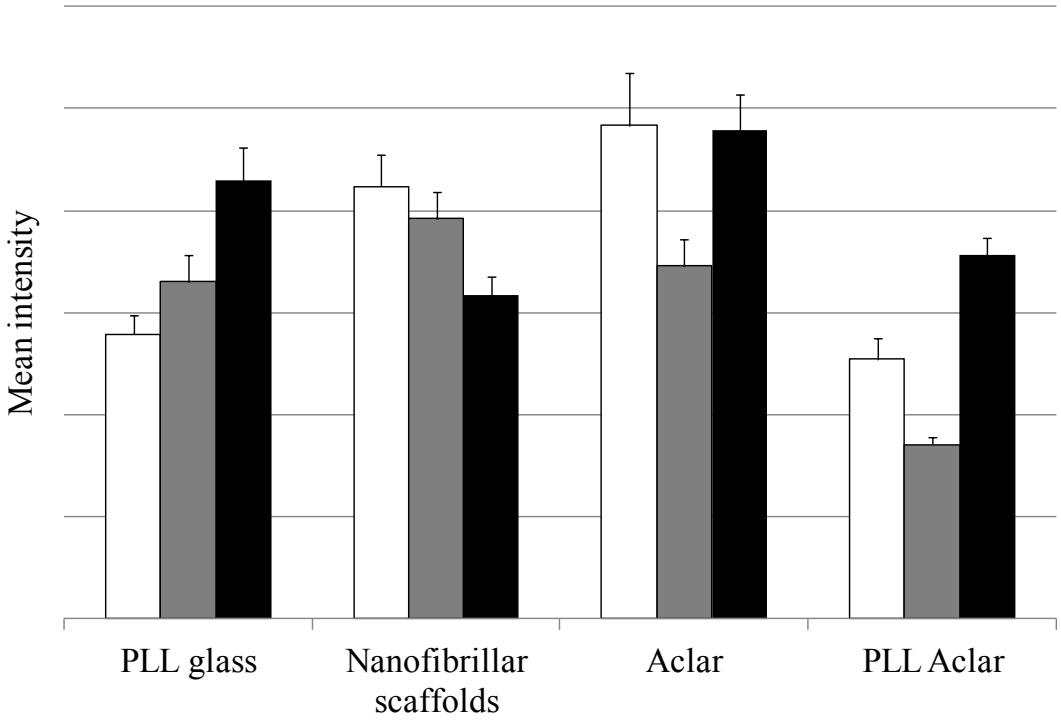

Figure 6.10: The white, gray, and black bars show the Cdc42, Rac1, and RhoA intensities, respectively. The data is based on maximum intensity level images. Bars show the mean, and error bars show standard error of n = 20 cells. [12*].

The results for astrocytes on PLL glass shows RhoA > Rac1 > Cdc42. This result is consistent with the AFM morphology and immunocytochemistry structural investigations, and indicated that RhoA activation had occurred by 24 h. The results for astrocytes on nanofibrillar scaffolds were reversed: Cdc42 > Rac1 > RhoA. The depression of RhoA relative to Rac1 is

consistent with the stellate formation of the astrocytes, as RhoA negatively regulates stellation [93]. The activation intensity results for astrocytes on Aclar and PLL Aclar are similar to each other but different from the PLL glass and nanofiber patterns, with Rac1 was depressed relative to both Cdc42 and RhoA: Cdc42 > Rac1 < RhoA.

6.1.2.12 Colocalization Analysis

The possible colocalization of actin with RhoA was investigated, using six 100X magnification fluorescence microscopy images of leading edges. Nanofiber auto fluorescence apparent in the Cdc42 channel was minimized prior to PC calculation as discussed in the Materials and Methods section.

Investigation of the colocalization of RhoA with F-actin yielded reliable results for astrocytes cultured on the nanofibrillar and PLL glass surfaces, with PCs equal to 0.656 ± 0.153 and 0.584 ± 0.096, respectively. While both exhibited partial colocalization, its character appeared to be different. Scatter plots obtained from astrocytes on the nanofibrillar surfaces consistently showed a weak tendency toward negative colocalization, which was supported by the appearance of the corresponding colocalization images. Scatter plots obtained from astrocytes on the PLL glass surfaces consistently showed partial colocalization but tended to be noisy. The slopes of the scatter plots were also different, astrocytes on the nanofibrillar surface has shown higher intensity of RhoA whereas the PLL glass surfaces has indicated higher intensity of F-actin (Figure 6.11).

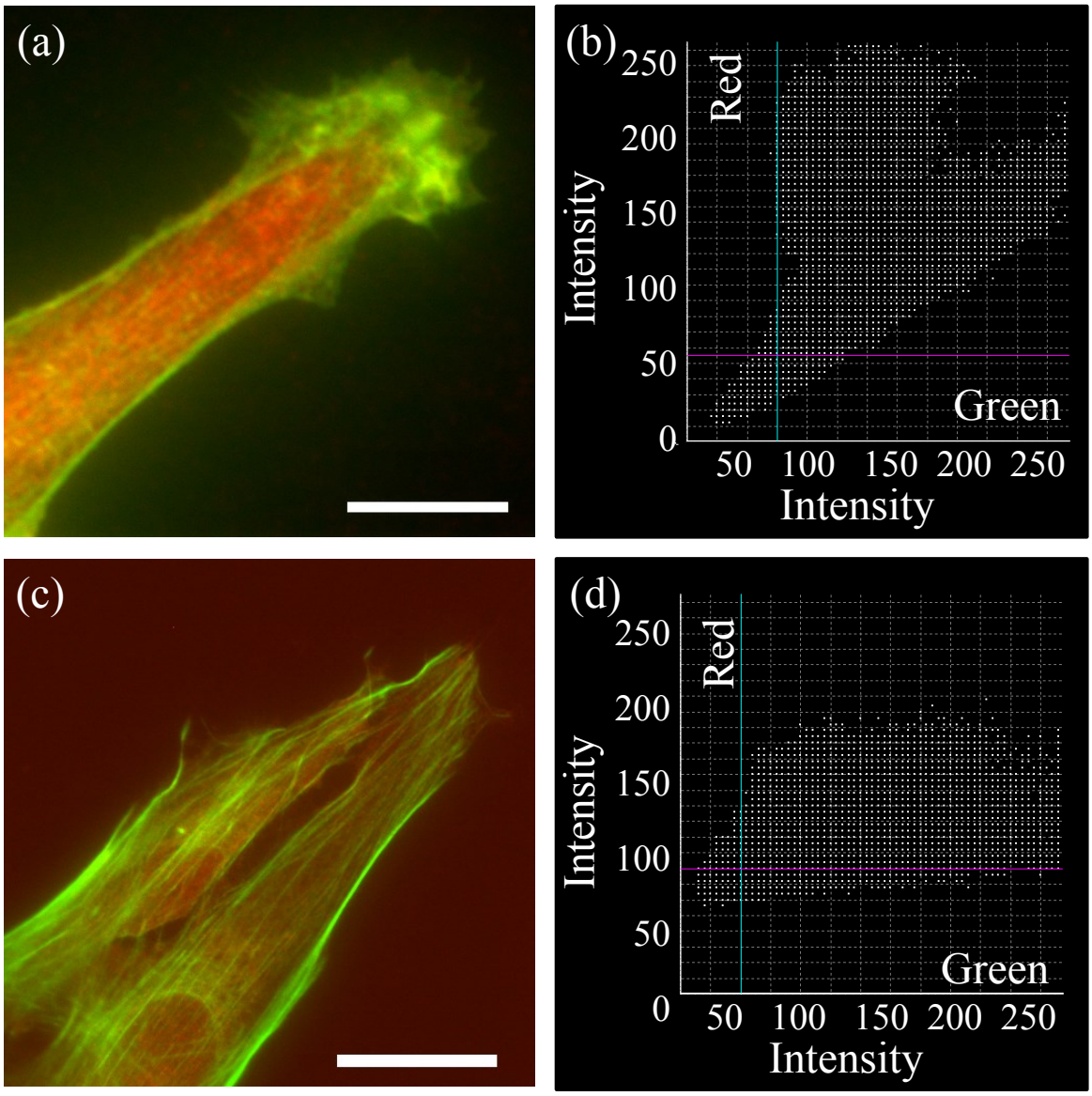

Figure 6.11: Overlaid fluorescence images of astrocytes cultured on (a) nanofibrillar scaffolds and (c) PLL glass labeled with phalloidin (F-actin) and anti-RhoA. The fluorescence was represented in green for F-actin and red for RhoA in (a) and (c). The scatter plots of F-actin and RhoA for nanofibrillar scaffolds (b) and PLL glass (d) showed partial colocalization with a mean PC of 0.66 and 0.58 respectively. Scale bar in (a) and (c) show 10 µm and 20 µm, respectively. [12*]. Fluorescent images by I. Ahmed, Shreiber laboratory with colocalization analysis in this thesis.

6.1.3 Discussion

Investigation of the morphological responses of cerebral cortical astrocytes to the four different culture surfaces demonstrated a series of responses, which involved combinations of filopodia, lamellipodia, and stress fiber formation, and stellation. The three-dimensional nature of AFM imaging demonstrated that differences in cell spreading were involved. Preferential activation of Rho GTPase upstream regulators known to be associated with the morphological responses was demonstrated using immunocytochemistry. The observed responses were induced by the four different culture surfaces without the introduction of any chemical agents. The results therefore support the hypothesis that the extracellular environment can trigger preferential activation of members of the Rho GTPase family with demonstrable morphological consequences for cerebral cortical astrocytes.

The maximum intensity level images of immunolabeling results of Cdc42, Rac1, and RhoA indicated that preferential activation of Cdc42 compared with RhoA occurred for the astrocytes on the nanofibrillar surfaces, while the opposite, preferential activation of RhoA compared with Cdc42, occurred for the astrocytes on the PLL glass. Partial colocalization of RhoA and F-actin was also demonstrated by astrocytes on the PLL glass. The standard interpretation of the immunolabeling results for PLL glass would be that at 24 h, the astrocytes on the PLL glass surfaces had formed contractile stress fibers [94]. The morphological response observed by the AFM and phalloidin imaging showed prominent stress fiber formation, consistent with the standard interpretation. In contrast, astrocytes on the nanofibrillar surfaces showed a different morphological response. The astrocytes on nanofibrillar scaffolds displayed the highest percentage of stellate response, with long processes instead of the lamellipodia/filopodia observed on the PLL functionalized surfaces. This is consistent with previously reported results

[1, 10, 37, 38, 72]. There was also a difference in the typical cell body shape, with vertices instead of a rounded, lamellipodial morphology. Using GHPF AFM, it was also shown that by 24 h direct cell-cell interaction by long processes with specialized contacting structures had occurred. The immunocytochemistry results indicated that RhoA was depressed relative to Cdc42. This would be consistent with stellation induced by inhibition of the RhoA effector kinase ROCK through depression of RhoA [80]. It has been reported that stellation can proceed via either protein kinase C (PKC) or cyclic AMP dependent protein kinase A pathways [84]. Additional investigations suggest that RhoA is an effector of the PKC signaling pathway [93]. A possible hypothesis consistent with the present results is that stellation was associated with inhibition of Rho kinase [80] achieved through depression of RhoA levels, potentially with alteration to the PKC cycle [93].

As no chemical agents were used, the differences in the responses were attributed to differences in the physical environments. The contact angle measurements demonstrated that the nanofibrillar scaffolds had surface polarities that were about 10% more hydrophobic than those of the PLL glass and PLL Aclar surfaces. This enables some of the known properties of PLL functionalization to be extrapolated to the unfunctionalized nanofibrillar scaffolds. PLL functionalization is known to add positive charge to culture surfaces. The net charge behavior of cell membranes is dominated by negatively charged sialic-acid-containing glycoproteins [95, 96]. Therefore, the expected interaction between the astrocytes and the PLL functionalized surfaces would be to maximize the Coulomb interaction, resulting in an increase of the cell-substrate interaction area and spreading of the cell body; and this was the effect that was observed. Astrocytes on the nanofibrillar surfaces displayed less cell spreading, while astrocytes on the Aclar surfaces, about 30% more hydrophobic than the PLL surfaces, were characterized

by a marked lack of cell spreading. These results and others [97] suggest that astrocytes may be fairly sensitive to the charge characteristics of their environments, which is a hypothesis that can be tested in future work.

The surface roughness variations considered in the present work were those that existed "naturally" in the four culture environments. These measurements demonstrated that two scales of surface roughness were present on the nanofibrillar surfaces: a large-scale RMS roughness between nanofibers and a small-scale RMS roughness along the nanofibers. The RMS roughness along the individual nanofibers was close in value to that of the PLL glass surfaces. Therefore, one distinguishing physical property for the nanofibrillar surfaces was the large-scale component of their surface roughness. This suggests that multiple receptor types may be involved in the astrocyte response to nanofibrillar scaffolds.

Astrocyte responses to the PLL glass and PLL Aclar surfaces appeared to reflect the differences in their surface roughness. The AFM surface roughness measurements demonstrated that significant differences in RMS surface roughness existed between the PLL glass and PLL Aclar surfaces although similarity in their surface polarity, confirmed by the contact angle measurements, was achieved through PLL functionalization. The AFM results indicated that there was a stronger stimulation of filopodia formation on the PLL Aclar surfaces although the cell clustering and cell spreading behavior was similar for the astrocytes on the PLL glass and PLL Aclar surfaces. The AFM images further demonstrated that the astrocyte filopodia appeared to infiltrate the valleys on PLL Aclar (Figure 6.8 (c)). The immunocytochemistry results indicated that Cdc42 activation was significantly greater than Rac1 activation for the PLL Aclar surfaces, which is consistent with a filopodia response. The Cdc42 activation was significantly less than Rac1 activation for the PLL glass surfaces. These results suggest a possible link

between the nanoscale surface roughness and activation of Cdc42 with consequent filopodia formation as an exploratory response.

Surface roughness may be a meaningful parameter for certain response aspects rather than a dominant factor for an overall response in astrocytes. As the latter may be an aggregate of all meaningful parameters, not just one, the nanoscale influence of surface roughness should continue to be investigated.

6.1.4 Conclusion

Morphological differences among astrocytes cultured on PLL glass, nanofibrillar scaffolds, Aclar, and PLL Aclar surfaces were demonstrated with AFM and phalloidin staining of F-actin. The differences and similarities of the morphological responses were consistent with differences and similarities of the surface polarity and surface roughness of the four surfaces investigated in this work. An initial quantitative immunolabeling study further identified significant differences in the activation of Rho GTPases. Astrocytes cultured on nanofibrillar scaffolds showed a response that included stellation, cell-cell interactions by stellate processes and evidence of depression of RhoA. The astrocyte response to the nanofibrillar scaffolds was unique among four surfaces studied. The results support the hypothesis that the extracellular environment can trigger preferential activation of members of the Rho GTPase family with demonstrable morphological consequences for cerebral cortical astrocytes, and suggest that the large-scale component of the nanofibrillar scaffold surface roughness (a form of nano-patterning) is a possible environmental trigger.

6.2 Differentiation of reactive-like astrocytes cultured on nanofibrillar and comparative culture surfaces

Repair of traumatic injury to the CNS remains a challenging problem. One of the hurdles that must be overcome is the glial scar, which is established after traumatic injury in mammalian systems and creates a barrier to regeneration of axons [98, 99]. A glial scar consists mainly of reactive astrocytes and proteoglycans. Reactive astrocytes at a wound site form chain-like clusters, and also undergo a morphological change, extending interwoven processes [100]. Furthermore, they express tenascins [101], and inhibitory chondroitin (C)- and keratan (K)-sulfate proteoglycans [102]. Uninterrupted expression of myelinating proteins by oligodendrocytes adds to the blockage. The result is a permanent scar that biomechanically and biochemically blocks axonal elongation and reconnection [30].

The effect of a physical environment on cell adhesion and differentiation has recently been recognized, especially in neural cells. Collectively, studies of cell responses to nano-patterning [12, 103, 104, 105, 106, 107], elasticity [72, 108, 109, 110, 111], surface roughness [5, 77], and surface polarity [75] suggest that controlling aspects of the physical environment holds potential for inducing preferential differentiation of reactive astrocytes into non-inhibitory pathways. During the last decade, promising results have been obtained using nanofibrillar scaffolds [10, 112, 113] and hydrogels [114] for regenerative repair of traumatic CNS injuries. The scaffold environments themselves present an array of potentially directive physical properties.

The promising results of polyamide nanofibrillar scaffolds motivated the investigation of reactive-like astrocyte differentiation in response to the external physical cues provided by the nanofibrillar scaffolds and additional comparative culture surfaces. Cerebral cortical astrocytes, a relatively uniform population, were treated with dibutyryladenosine cyclic monophosphate

(dBcAMP), and used to investigate the responses of reactive-like astrocytes to external physical cues. Astrocytes treated with dBcAMP develop morphologies that resemble the reactive astrocytes [115]. The same four substrates used in the recent investigation of untreated cerebral cortical astrocytes responses to surface polarity and surface roughness variations [12] were used in the present study: (1) the electrospun polyamide nanofibrillar scaffolds and three comparative culture surfaces, (2) poly-L-lysine (PLL) functionalized glass, (3) PLL functionalized Aclar, and (4) unfunctionalized Aclar. This enabled investigation of the differences between the untreated and dBcAMP-treated astrocyte responses to the same culture environments and properties. In the present study, the local elasticity and surface energies of the substrates were investigated and the results were added to the previous investigations of surface polarity and surface roughness. The physical property trends were then compared with the morphological and protein expression responses.

Morphological differentiation of dBcAMP-treated astrocytes was investigated using AFM and immunocytochemistry. GFAP is an intermediate filament protein thought to be involved in the structure and function of the astrocyte cytoskeleton although its function is not well understood. Up-regulation of GFAP is typically considered as an indication of increased reactivity. Quantification of GFAP expression was performed using the confocal laser scanning microscopy (CLSM) z-series. Astrocyte stellation is a tubulin-dependent rearrangement of cytoskeleton [84]. Tubulin expression was also quantified using confocal z-series. Immunolabeling of dBcAMP-treated astrocytes with the Rho GTPase upstream regulators for filopodia, lamellipodia, and stress fiber formation, namely Cdc42, Rac1, and RhoA [78], was also performed, enabling comparisons of these cytoskeletal proteins with the previously reported

results for untreated astrocytes [12]. The protein expressions were quantified using maximum intensity level images acquired by fluorescence microscopy.

The study was organized as follows. Investigations of the physical properties of each culture environment, assessed in terms of local elasticity, work of adhesion, RMS surface roughness, and surface polarity, are presented first. The results indicated that the culture surfaces, including the nanofibrillar scaffolds, occupied distinct ranges of physical property parameter space. Investigations of the astrocyte responses, assessed in terms of morphology and protein expression, are presented next. The morphological response and Rho GTPase expression for the dBcAMP-treated astrocytes are also compared with those of untreated astrocytes [12]. Quantitative analyses for morphological and protein expression estimates are given. Results from investigations of two proteins associated with astrocyte reactivity, GFAP and tubulin, are then presented. The GFAP and tubulin investigations were performed exclusively for the dBcAMP-treated astrocytes.

The results indicate that the nanophysical cues of the extracellular environment can modulate the reactive response of dBcAMP-stimulated cerebral cortical astrocytes, and that different cues could have more directive importance for astrocytes in scarring mode versus in untreated mode. DBcAMP-treated astrocytes cultured on the nanofibrillar scaffolds showed a unique Rho GTPase and morphological non-response. Cdc42, Rac1, and RhoA expressions and consequent morphologies were almost unchanged from their untreated values while the Rho GTPase expressions and morphologies of the three comparative culture surfaces were greatly changed. Furthermore, dBcAMP-treated astrocytes cultured on the PLL Aclar surfaces exhibited responses that were reminiscent of glial scar formation. The comparison of dBcAMP-treated and untreated astrocyte responses suggested that different nanophysical cues may have more directive

importance in a wound-healing situation. The elasticity property was indicated as potentially more directive for dBcAMP-treated astrocytes than for untreated astrocytes [116].

6.2.1 Materials and Methods

6.2.1.1 Nanofibrillar Scaffolds

Polyamide nanofibers (median diameter ~180 nm) were electrospun from a blend of two polymers [$(C_{28}O_4N_4H_{47})_n$ and $(C_{27}O_{4.4}N_4H_{50})_n$] onto Aclar coverslips by Donaldson Co, Inc (Minneapolis, MN). The resulting non-woven nanofibrillar scaffold was approximately 2 μm thick when measured by optical microscopy [12].

6.2.1.2 Planar Culture Surfaces

Glass coverslips (12 mm, No 1 coverglass; Thermo Fisher Scientific, Waltham, MA) and Aclar coverslips (Ted Pella, Inc., Redding, CA) were used as underlying substrates. The substrates were placed in a 24-well tissue culture plate and covered with 1 mL of PLL solution (50 μg PLL/mL in dH_2O) overnight. The coverslips were then rinsed with dH_2O, sterilized with ultraviolet light, and used for the cultures. One set of Aclar coverslips was left unfunctionalized [12].

6.2.1.3 Primary dBcAMP-treated astrocyte cultures

The cerebral hemispheres of new born Sprague Dawley rats (postnatal day 1 or 2) were isolated aseptically. The cerebral cortices were dissected out, freed of meninges, and collected in HBSS. They were minced with sterile scissors and digested in 0.1% trypsin and 0.02% DNase for 20 min at 37°C. The softened tissue clumps were then triturated by passing several times through a fine bore glass pipette to obtain a cell suspension. The cell suspension was washed twice with culture media (DMEM+10% FBS) and filtered through a 40 μm nylon mesh. For culturing, the cell suspension was placed in 75 cm^2 flasks (one brain/flask in 10 mL growth medium) and incubated at 37ºC in a humidified CO_2 incubator. After 3 days of incubation the growth media was removed, cell debris was washed off, and fresh medium was added. The medium was changed every 3-4 days. After reaching confluency (about 7 days), the cultures were shaken to remove macrophages and other loosely adherent cells. To obtain reactive-like astrocytes, 0.25mM dBcAMP was added to the culture medium and the serum concentration was reduced to 1%. The cultures in dBcAMP containing medium were incubated for 7-8 more days with a media change every 3-4 days. The morphology of the cells was observed on alternate days under a phase contrast microscope. In the control cultures, the cells were fed with DMEM + 1% FBS (without dBcAMP). All procedures were approved by the Rutgers Animal Care and Facilities Committee (IACUC Protocol #02-004).

After completing dBcAMP treatment, reactive-like astrocytes were then harvested with 0.25% Trypsin/EDTA (Sigma-Aldrich) and re-seeded at a density of 30,000 cells per well directly on 12 mm Aclar or PLL Aclar coverslips, PLL glass coverslips, or on Aclar coverslips coated with nanofibers in 24-well plates in astrocyte medium containing dBcAMP (0.5 mL),

fixed with paraformaldehyde and then stained for F-actin, Cdc42, Rac1, and RhoA. Parallel cultures were immunostained with GFAP, an identification marker for astrocytes, and more than 95% were found to be GFAP-positive. Another set of parallel cultures were immunostained for GFAP/β-tubulin.

6.2.1.4 AFM

AFM images of astrocytes were captured using a Veeco Instruments Nanoscope IIIA (Bruker AXS Inc, Madison, WI; formerly Veeco Metrology) operated in ambient air. A J scanner with 125 μm × 125 μm × 5.548 μm x-y-z scan range and an E scanner with 13.5 μm × 13.5 μm × 3.08 μm x-y-z scan range were used. The AFM was operated in contact mode silicon nitride tips with a nominal tip radius of 25 nm and cantilever spring constant k = 0.58 N/m (Nanoprobe SPM tips, Bruker AXS Inc, Madison, WI; formerly Veeco Metrology). Frequency domain Gaussian high pass filtering (GHPF) was used to segment the astrocytes from the substrate backgrounds in AFM height images [83]. AFM images of at least 20 astrocytes for each culture surface were evaluated to ensure that the results were representative.

6.2.1.5 Astrocyte Cell Shape Index

Cell soma investigations by AFM indicated that the reactive-like astrocytes had comparable cell spreading. Therefore, the appropriate cell shape index (CSI) is defined as the ratio of the perimeter squared to the two-dimensional cell area [117]:

$$CSI = \frac{P^2}{4\pi A} \tag{6.2}$$

where P is the cell perimeter and A is the cell area. This definition describes stellation as a departure from $CSI = 1$ for a circular cell. The cell perimeter and area were calculated following manual segmentation of cells from GHPF AFM height images. The procedure was implemented in MATLAB version 7.7.0 (R2008b) using Image Processing Toolbox (The MathWorks).

6.2.1.6 Astrocyte Soma Height Measurements

Untreated and dBcAMP-treated astrocyte maximum soma height values were measured using the section analysis of Nanoscope Software version 5.30r3.sr3 and NanoScope Analysis 1.10 (Bruker AXS Inc, Madison, WI; formerly Veeco Metrology). Twenty cells from each set of culture surfaces were analyzed by section profile through the nucleus region. Variations in maximum soma height data among the culture surfaces were analyzed using analysis of variance (ANOVA) followed by pairwise post hoc comparisons with Tukey's test [82]. Significance levels were set at $P < 0.05$.

6.2.1.7 Astrocyte Process Measurements and Number of Astrocyte Processes

Untreated and dBcAMP-treated astrocyte cell process lengths were measured based on AFM height and GHPF AFM height images. Twenty cells from each set of culture surfaces were analyzed by measuring the length of processes manually, and the number of processes of each astrocyte was counted. An extension longer than the diameter of a cell soma was considered to be a process. Variations in astrocyte process length and number of process data among the culture surfaces were analyzed using ANOVA followed by pairwise post hoc comparisons with Tukey's test [82]. Significance levels were set at $P < 0.05$.

6.2.1.8 AFM Force Curves of Culture Surfaces

The local elasticity of the polyamide nanofibrillar scaffolds and comparative culture surfaces were investigated by AFM force curves as described in Chapter 5.2 of this thesis.

6.2.1.9 Immunolabeling for Cdc42, Rac1, RhoA, and F-actin

The astrocytes cultured on coverslips were fixed with 4% paraformaldehyde for 10 minutes, permeabilized with 0.5% Triton X-100 for 5 minutes, and blocked with 10% normal goat serum for 30 minutes. After removing the normal goat serum, the cells were double stained with one of the primary antibodies mouse anti-Cdc-42 (1:200), mouse anti-RhoA (1:200), or mouse anti-Rac1 (1:25) (all from Cytoskeleton, Denver, CO), and phalloidin (Life Technologies, Grand Island, NY). The incubation in the primary antibodies was done overnight at room temperature in a humidity chamber. Coverslips were then washed with phosphate buffered saline (PBS) and stained with goat anti-mouse Alexa 568 IgG secondary antibody (ex 579 nm, em 603 nm; Life Technologies) at a 1:500 dilution for 1 hour. Following the antibody staining, the cells were rinsed, stained with Phalloidin-488 (ex 498 nm, em 520 nm; Life Technologies) at a 1:100 dilution for 1 hour, mounted on microscopic slides with GelMount (Biomeda, Foster City, CA), and observed under an Olympus IX81 inverted microscope (Olympus, Tokyo, Japan).

6.2.1.10 Image Capture Conditions for Cdc42, Rac1, and RhoA expression estimate

Maximum intensity level images were captured specifically for protein expression estimation using an Olympus IX81 inverted microscope (Olympus). The images had identical scale bars and pixel resolutions as a requirement for an accurate comparative analysis of activation intensity

patterns. Eight images (via 20× objective) were captured for each of the three antibodies on each of the four culture surfaces to ensure that the results were representative for the cultures as a whole. At this magnification, each image typically had several whole cells, and a total of 240 cells were investigated. Images of the astrocyte cultures were captured using Metamorph software (Molecular Devices LLC, Sunnyvale, CA). The amount of detected protein was quantified by segmenting each cell manually and measuring the average fluorescence intensity. The average background intensities of the fluorescence images were calculated, and subtracted from the average fluorescence intensity value. ImageJ software version 1.46r (National Institutes of Health, Bethesda, MD) was used for the quantitative analysis of light intensity. Intensity data were then analyzed using ANOVA followed by pairwise post-hoc comparisons with Tukey's test. Significance levels were set at $P < 0.05$.

6.2.1.11 Immunolabeling for GFAP and Tubulin

The astrocytes cultured on coverslips were fixed with 4% paraformaldehyde for 10 minutes, permeabilized with 0.5% Triton X-100 in PBS for 5 minutes, and blocked with 10% normal goat serum for 30 minutes. After removing the normal goat serum, the cells were double stained with one of the primary antibodies and phalloidin. Rabbit anti-GFAP (Dako, Carpinteria, CA) was diluted 1:500 while mouse anti-β-tubulin (Sigma-Aldrich, St. Louis, MO) was diluted 1:200. The incubation in the primary antibodies was done overnight at room temperature in a humidity chamber. Coverslips were then washed three times with PBS and stained appropriate secondary anti-body either goat anti-rabbit Alexa 568 IgG (Life Technologies) or goat anti-mouse Alexa 568 IgG (Life Technologies). Both secondary anti-bodies were diluted 1:500 and incubation was for 1 hour at room temperature. Secondary anti-body staining coverslips were rinsed three times with PBS. Following PBS rinse, the coverslips were stained with Alexa Fluor® 488 Phalloidin

(Life Technologies) diluted 1:100 for 1 hour, rinsed again with PBS as above, and stained with DAPI (Life Technologies) for 5 minutes. After completing staining, coverslips were mounted on microscopic slides with GelMount (Biomeda), and observed under an Olympus FluoView 1000 Laser Scanning Confocal Microscope system attached to an Olympus IX81 automated inverted microscope platform.

6.2.1.12 Quantitative GFAP and Tubulin expression estimate

Confocal z-series images were captured using an Olympus FluoView 1000 Laser Scanning Confocal Microscope system attached to an Olympus IX81 automated inverted microscope platform equipped with a 40× oil immersion objective (N.A.=1.3). The increments between the z-series were set to 1.13 μm in order to avoid oversampling of fluorophores. The z-series were acquired under identical imaging conditions, including the same high voltage (HV) and offset settings, same objective, and same resolution (1024×1024 pixels). The HV and offset levels were set to a level so that the pixels were not saturated. This is crucial to ensure the accuracy of the relative intensity comparisons. Images were analyzed using MATLAB version 7.7.0 (R2008b) Image Processing Toolbox (The MathWorks) and ImageJ version 1.46r (National Institutes of Health). The maximum intensity projection images were obtained from the z-series, the boundaries of the cells were determined manually, and then the total intensity and the number pixels were calculated by using the z-series and cell boundaries. The average background intensity values were calculated for each z-series because the autofluorescence was different on different culture surfaces. The average background intensity was then multiplied by the number of pixels of z-series, and subtracted from the total intensity. Finally, the total amount of GFAP or tubulin expression / cell was determined. At least 50 cells were analyzed for each culture surface. Variations in GFAP and tubulin expression estimation data among the culture surfaces were

analyzed using ANOVA followed by pairwise post hoc comparisons with Tukey's test [33]. Significance levels were set at $P < 0.05$.

6.2.2 Results

6.2.2.1 Local Elasticity Investigation of Culture Environments and Parameter Space Analysis

Reported investigations [72, 108, 109] have identified local elasticity as potentially directive. Local elasticity along individual nanofibers was characterized in the present work. AFM force curve measurements along individual nanofibers were taken and interpreted using the DMT elasticity interpretative model for the Young's modulus that included adhesion forces. Analysis of the Young's modulus results using both median-value box plots and mode-value distribution plots are shown in Figure 6.12.

Mode value analysis indicated that the Young's modulus comparison for the culture surfaces was

$$E_{PLL\ Glass} > E_{PLL\ Aclar} > E_{Aclar} \tag{6.3}$$

at room temperature and for interaction with an AFM tip. Both median and mode-value analyses indicated that the PLL glass substrate presented the most uniform elastic environment. Median versus mode value analysis suggested that PLL functionalization could result in a less uniform elastic environment for PLL Aclar, indicated by the emergence of tail values in the distribution.

The median value/mode value analysis further indicated that substrate elasticity dominated over the chemical functionalization effect since unfunctionalized and PLL functionalized Aclar had similar elasticity variances (shown as percentile boxes and lines) and distributions while PLL functionalized glass and PLL functionalized Aclar had different results for both.

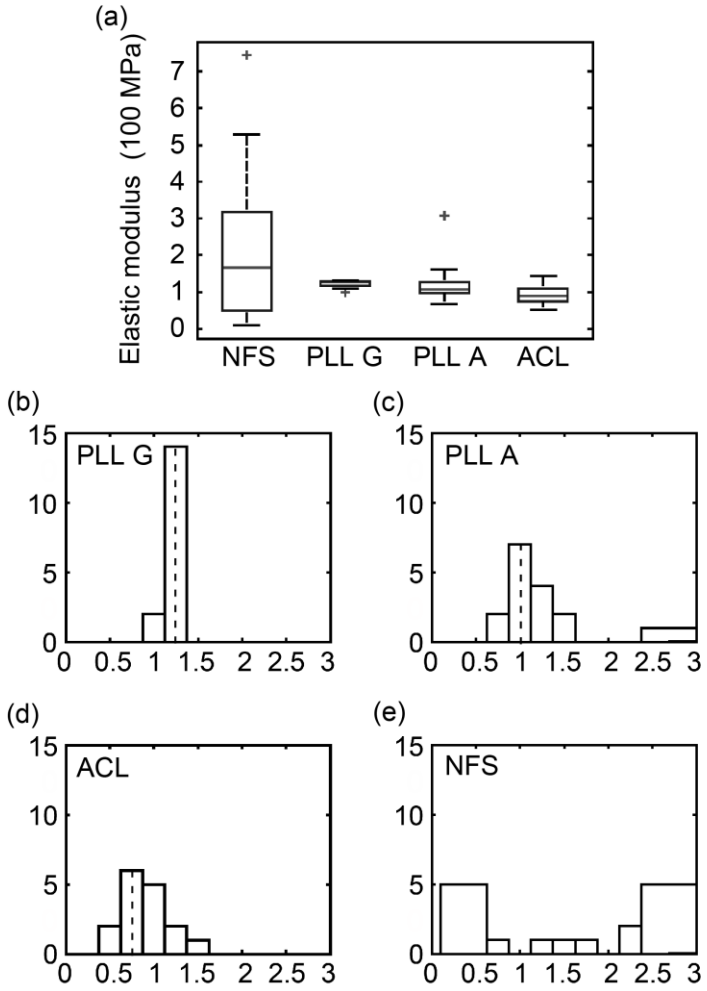

Figure 6.12: Elasticity of culture surfaces by AFM using DMT model for Young's modulus. (a) Young's modulus box plot: Solid lines show the median, and the box edges show the 25th and 75th percentiles. Histogram distribution plots of Young's modulus for (b) PLL glass, (c) PLL Aclar, (d) Aclar and (e) nanofibrillar scaffolds. Dashed lines show the mode values in (b), (c) and (d) in descending order. Unit x axis for (b), (c), (d), and (e) is 100 MPa. PLL G, PLL A, ACL, and NFS denote, PLL glass, PLL Aclar, Aclar and nanofibrillar scaffolds respectively. [117*].

The nanofiber median value Young's modulus was higher than that of PLL glass. However, mode value analysis showed that the median value resulted from its wide range of Young's modulus values. For the nanofibers, therefore, a median value analysis may not accurately represent the nanofiber elastic property. Specific investigation indicated that the higher elasticity values did not correspond to nanofiber crossings. However, the wide range of elasticity values may be due to the presence of hard and soft components in individual nanofibers, indicated by previously reported transmission electron microscopy analysis [70]. The wide range of elasticity values along individual nanofibers was accurately reflected in the percentile box and lines, compared with those for PLL glass, PLL Aclar, and Aclar.

6.2.2.2 Surface Energy Investigation and Parameter Space Analysis

Use of the DMT interpretive model further enabled investigation of the surface energies of the cell substrates by measuring the work of adhesion, W_{132}, between the tip and each culture surface [64]. W_{132} is the work that is needed to separate AFM tip from the culture surface in ambient air. The adhesive component of the AFM force curves was extracted, and used to investigate the work of adhesion.

Analysis of the work of adhesion using both median-value box plots and mode-value distribution plots, shown in Figure 6.13, revealed several features. First, despite the similar functionalization of PLL glass and PLL Aclar, the work of adhesion median value was higher for PLL Aclar (Figure 6.13 (a)). This resulted from the different distributions: the PLL glass distribution was single mode (Figure 6.13 (b)) with a narrow distribution and consistent median and mode values at about 0.16 J/m^2 The Aclar distribution (Figure 6.13 (c)) was also single

mode with consistent median and mode values at about 0.13 J/m^2. The widest range of work of adhesion values was observed for the nanofibrillar scaffolds (Figure 6.13 (d)). The majority were low work of adhesion values, which was reflected in the 0.119 J/m^2 median value and indications of a mode value at about 0.1 J/m^2 (Figure 6.13 (a) and (d)). The PLL Aclar distribution also displayed a range of work of adhesion values (Figure 6.13 (e)). Comparison of Aclar and PLL Aclar (Figure 6.13 (c) and (e)) indicated that this range resulted from the PLL functionalization. This suggests that the combination of chemical functionalization with surface roughness can result in higher work of adhesion, possibly through PLL conformation changes.

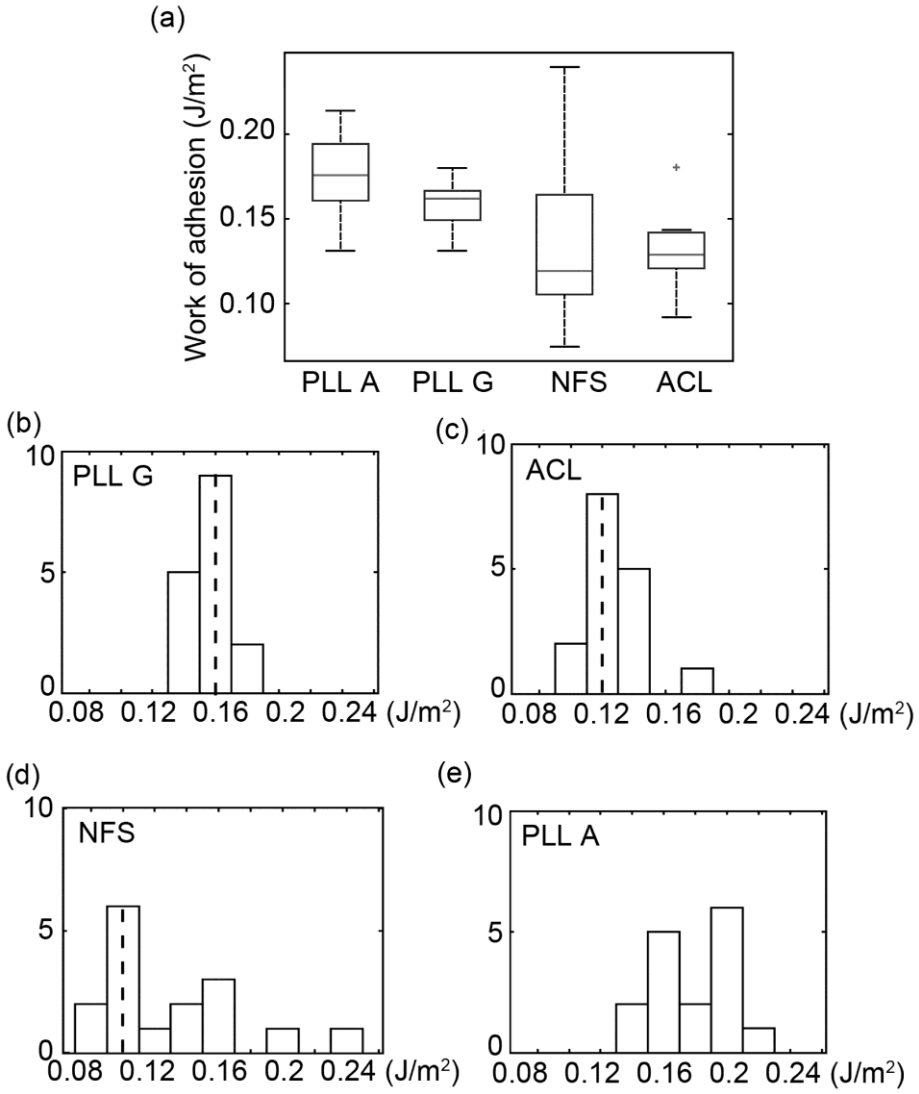

Figure 6.13: Work of adhesion characterization of culture surfaces. (a) Work of adhesion box plot. Solid lines show the median, and the box edges show the 25th and 75th percentiles. Histogram distribution plots of adhesion of (b) PLL glass, (c) Aclar, (d) nanofibrillar scaffolds and (e) PLL Aclar. Dashed lines show the mode values in (b), (c) and (d) in descending order. PLL G, ACL, NFS and PLL A, denote PLL glass, Aclar, nanofibrillar scaffolds and PLL Aclar, respectively. [117*].

The data ranges for the work of adhesion and RMS surface roughness [12] were analyzed as a two-dimensional parameter space as shown in Figure 6.14 (a). The results indicated that the culture surfaces, including the nanofibrillar scaffolds, occupied distinct ranges of physical property parameter space. Comparison of the work of adhesion and RMS surface roughness

(Figure 6.14 (a)) versus surface polarity [12] and surface roughness data ranges (Figure 6.14 (b)) suggested that the more local work of adhesion environment could present variations that would not be evident in the more macroscopic environment assessed by contact angle measurements.

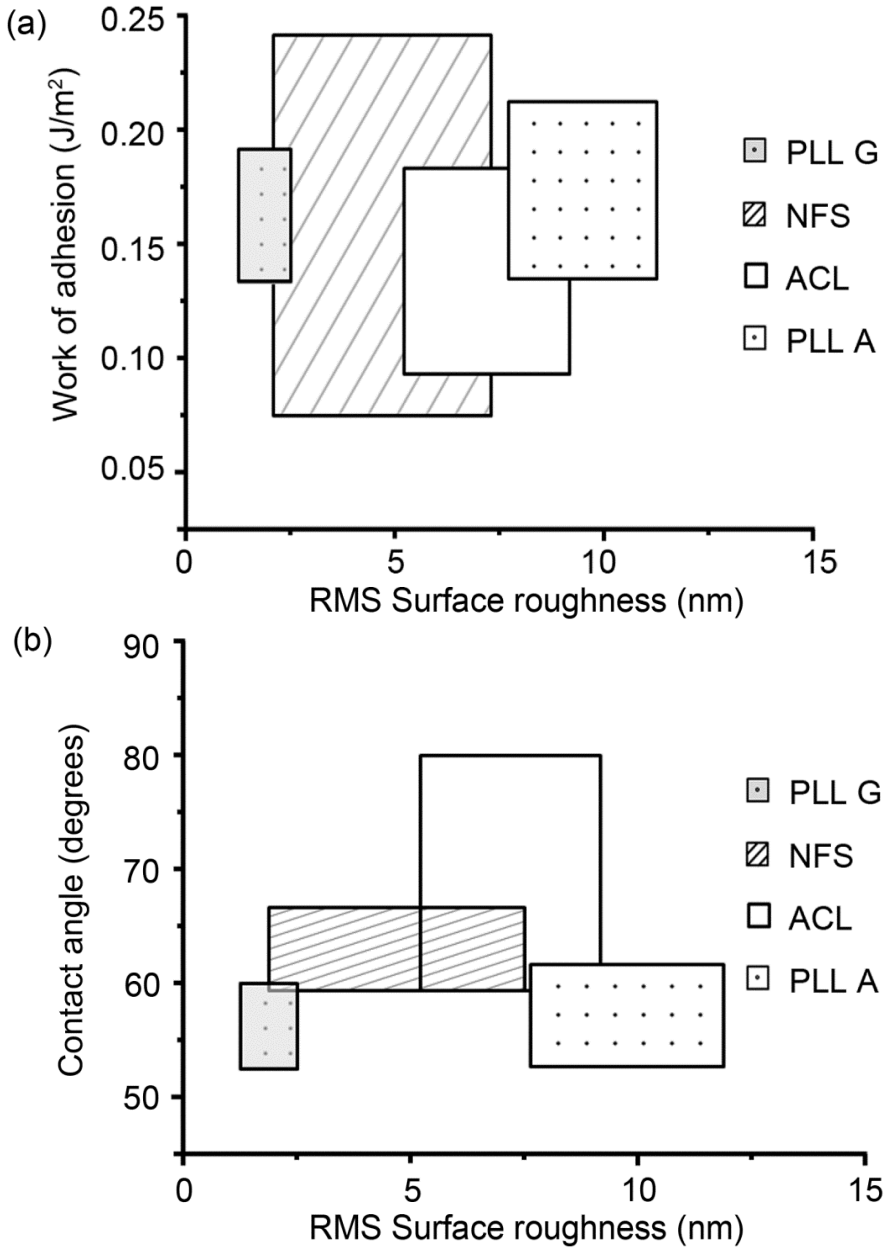

Figure 6.14: Two-dimensional parameter space representation of work of adhesion and surface roughness of culture surfaces. (b) Two-dimensional parameter space representation of surface polarity and surface roughness of culture surfaces. PLL G, NFS, ACL and PLL A denote PLL glass, nanofibrillar scaffolds, Aclar and PLL Aclar, respectively. [117*].

6.2.2.3 Astrocyte Responses: Morphology Investigation

6.2.2.3.1 Cell density

Cell density on different cell substrates was measured by counting the nuclei from at least 22 DAPI-stained images per culture surface. Initially, cell plating density on all surfaces was 66 cells/mm^2. The dBcAMP-treated astrocyte densities for each substrate in cells/mm^2 are given in Table 6.2.

Table 6.2: Reactive-like astrocyte cell density measurement results (mean±SEM). [117*].

	Aclar	PLL glass	PLL Aclar	Nanofibrillar scaffolds
Cell density [#cells/mm^2]	117±7	189±24	202±17	206±14

Cell density on Aclar was low compared to other substrates, indicating that the cell adhesion and/or proliferation on Aclar surfaces were negatively influenced by the properties of this substrate. The low cell density on Aclar may be due to its lower hydrophilicity resulting in lower cell adhesion [12]. The higher cell densities on the PLL functionalized surfaces were possibly because of increased cell adhesion by the positive charges introduced to the substrate by functionalization [118]. The highest cell density was observed on the nanofibrillar scaffolds, which indicated that these surfaces were able to successfully modulate cell adhesion and/or proliferation without requiring PLL functionalization.

6.2.2.3.2 Astrocyte morphology investigation by AFM

DBcAMP-treated astrocyte morphologies and astrocyte-astrocyte interactions by AFM provided details of the different morphological responses to the culture surfaces investigated in this work. The dBcAMP-treated astrocytes cultured on PLL glass surfaces developed astrocyte-astrocyte interactions via long processes that suggested contact spacing [119] (Figure 6.15 (a)). Extensive nanoscale process formation was also observed (inset). The nanoscale processes were about ~10-50 nm in diameter and were observed around both processes and somata.

The dBcAMP-treated astrocytes cultured on nanofibrillar scaffolds developed long processes in a stellate pattern (Figure 6.15 (b)). Astrocyte-astrocyte interactions suggestive of contact spacing were observed. Extensive cell clustering was not observed.

The dBcAMP-treated astrocytes cultured on Aclar surfaces developed 2-3 directional processes (Figure 6.15 (c)). Astrocyte-astrocyte interactions were few in number; when present, they were suggestive of contact spacing. As astrocyte-astrocyte interactions were not representative for this culture, AFM images of two individual cells that displayed commonly observed morphologies are shown in Figure 6.15 (c).

The dBcAMP-treated astrocytes cultured on PLL Aclar surfaces also developed long processes, but astrocyte-astrocyte interactions consisted of intertwined processes rather than contact spacing. This resulted in chain-like cell clusters reminiscent of glial scar formation (Figure 6.15 (d)).

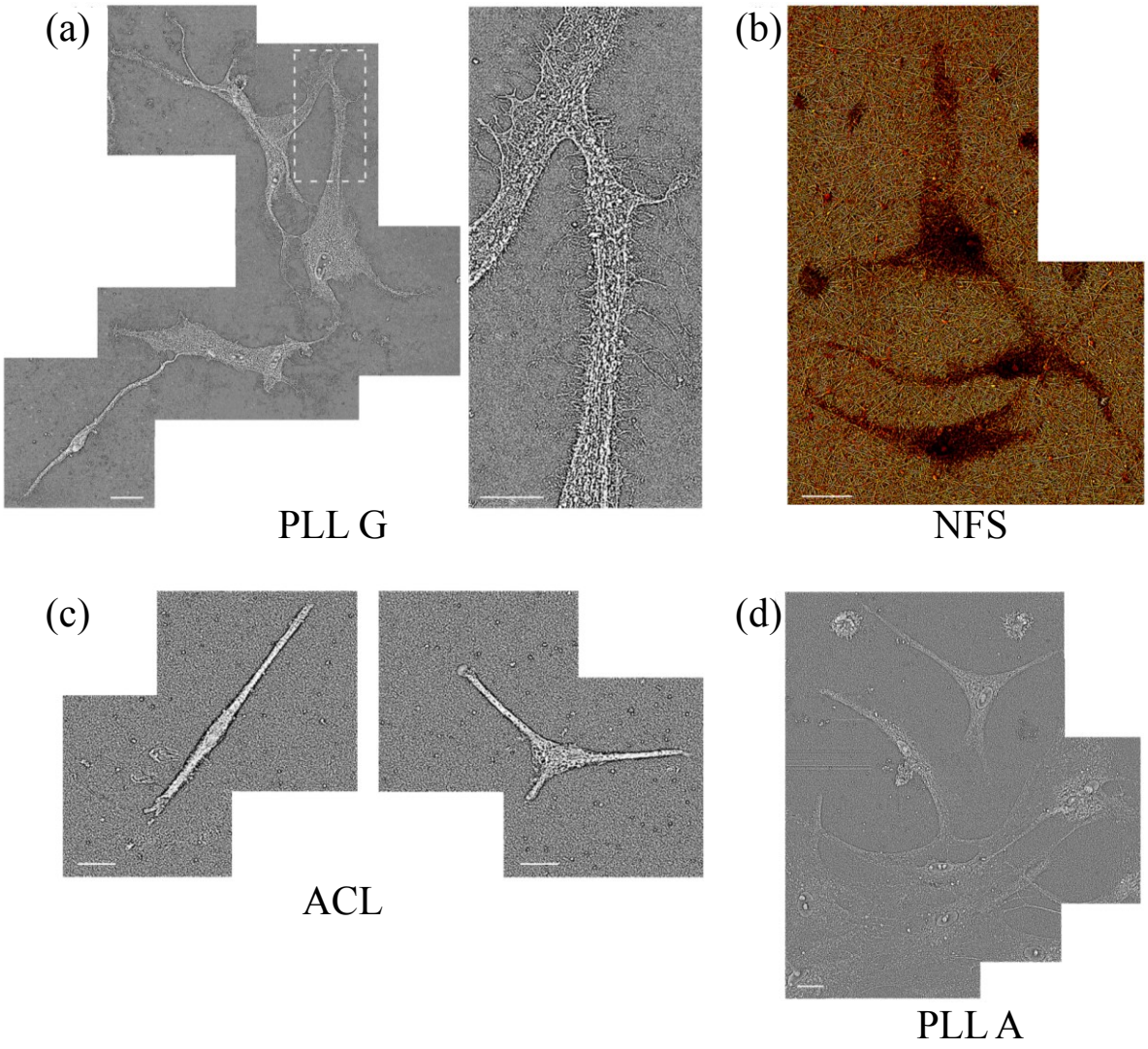

Figure 6.15: Morphology investigation of reactive-like astrocytes with AFM height GHPF images. (a) Astrocytes cultured on PLL glass, with close-up from dashed box region inset. The close up image shows the nanoscale process formation. (b) Astrocytes cultured on nanofibrillar scaffolds. (c) Representative morphologies for astrocytes cultured on Aclar. (d) Astrocytes cultured on PLL Aclar shows glial-scar like chain formation. PLL G, NFS, ACL, and PLL A, and denote PLL glass, nanofibrillar scaffolds, Aclar, and PLL Aclar, respectively. Scale bars, 20 μm. [117*].

6.2.2.3.3 Astrocyte quantitative morphology assessment and comparison

The morphological responses for the dBcAMP-treated astrocytes were quantified as process length, the number of processes, and maximum soma heights using measurements taken from the AFM height images. A cell shape index was also calculated from perimeter and area measurements taken from the AFM height images. These measures were investigated for statistically significant differences using Tukey's test pairwise comparisons with $P < 0.05$. Pairwise comparisons were made for the dBcAMP-treated astrocytes, untreated astrocytes, and dBcAMP-treated versus untreated astrocytes cultured on the same four culture surfaces. A total of 20 astrocytes per each culture were selected randomly from both dBcAMP-treated and untreated astrocyte samples. The results, shown in Figure 6.16, are displayed as mean-value bar graphs with standard error of the mean.

Analysis of process lengths is shown in Figure 6.16(a). For dBcAMP-treated astrocytes alone, post hoc analysis with Tukey's test revealed that the process lengths of astrocytes cultured on PLL glass were significantly longer than the ones on nanofibrillar scaffolds ($P < 0.0001$) and Aclar ($P = 0.0246$). The astrocyte process lengths on PLL Aclar were significantly longer ($P = 0.0088$) than the ones on nanofibrillar scaffolds. No significant differences were detected between PLL glass versus PLL Aclar ($P = 0.512$), PLL Aclar versus Aclar ($P = 0.4293$), and Aclar versus nanofibrillar scaffolds ($P = 0.4058$).

For untreated astrocytes alone, post hoc analysis with Tukey's test revealed that the process lengths of astrocytes cultured on PLL glass were significantly longer ($P = 0.0166$) than the ones on Aclar. Other pairwise comparisons, PLL glass versus PLL Aclar ($P = 0.292$), PLL glass versus nanofibrillar scaffolds ($P = 0.3556$), nanofibrillar scaffolds versus Aclar ($P = 0.5694$),

nanofibrillar scaffolds versus PLL Aclar (P = 0.9996), and PLL Aclar versus Aclar (P = 0.6254) were not significant.

For dBcAMP-treated versus untreated astrocytes, the process length statistical analysis showed that dBcAMP-treated astrocyte process lengths were significantly longer (max P = 0.00369) than untreated ones except for the astrocytes on nanofibrillar scaffolds (P = 0.28561). As shown in Figure 6.16 (a), the greatest process length increases were observed for the astrocytes cultured on the PLL functionalized surfaces, while the smallest increase was observed for astrocytes cultured on the nanofibrillar scaffolds.

Analysis of the number of processes is shown in Figure 6.16 (b). No significant differences in the number of processes were observed for dBcAMP-treated astrocytes alone, untreated astrocytes alone, or for comparisons of dBcAMP-treated versus untreated astrocytes.

Analysis of astrocyte maximum soma height investigation, shown in Figure 6.16 (c), was performed to investigate the cell spreading behavior. No significant difference in the maximum soma height of reactive-like astrocytes alone was observed (min P = 0.3477), which justified use of the two-dimensional CSI [120] analysis shown in Figure 6.16 (d). For untreated astrocytes alone, Tukey's all pairs comparison of untreated astrocytes showed that the maximum soma height of astrocytes cultured on Aclar was significantly higher than the ones of PLL Aclar (P<0.0001) and PLL glass (P < 0.0001). The maximum soma height of astrocytes on nanofibrillar scaffolds was significantly higher than the ones of PLL Aclar (P < 0.0001) and PLL glass (P < 0.0001). For reactive-like versus untreated astrocytes, the pairwise comparisons were all significant (max P = 0.00652), and indicated contraction for reactive-like astrocytes cultured

on Aclar and nanofibrillar scaffolds and swelling for the ones cultured on PLL Aclar and PLL glass.

Analysis of the two-dimensional CSI is shown in Figure 6.16 (d). A two-dimensional CSI uses a ratio of area to perimeter to describe stellation as a departure from CSI = 1 for a circular cell [40, 41]. The pairwise comparisons of reactive-like astrocytes alone showed the CSI of reactive-like astrocytes cultured on nanofibrillar scaffolds was significantly less than ones of PLL Aclar ($P = 0.0055$) and PLL glass ($P < 0.0001$). For untreated astrocytes alone, the statistical results of CSI analysis showed that no significant difference exists (min $P = 0.0611$). For reactive-like versus untreated astrocytes, the CSI increased on all surfaces (max $P = 0.033$) except Aclar ($P = 0.6$), which showed a decrease. The most significant CSI change was observed for reactive-like versus untreated astrocytes cultured on PLL Aclar ($P = 0.0037$).

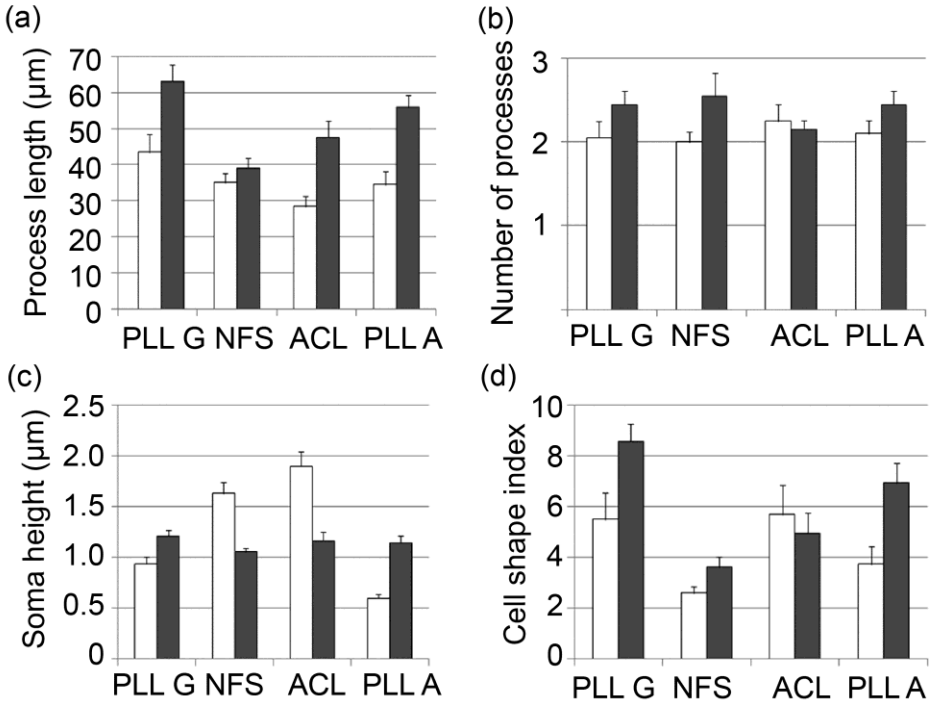

Figure 6.16: Quantitative morphology assessment of reactive-like and quiescent astrocytes cultured on PLL glass, nanofibrillar scaffolds, Aclar, and PLL Aclar. Gray bars: reactive-like astrocytes, White bars: quiescent astrocytes. (a) Average length of astrocyte processes. (b) Average number of processes. (c) Average maximum soma height. (d) Average CSI results. Error bars show standard error of n=20 cells. PLL G, NFS, ACL, and PLL A, and denote PLL glass, nanofibrillar scaffolds, Aclar, and PLL Aclar, respectively. [117*].

6.2.2.4 Astrocyte Responses: Protein Expressions

6.2.2.4.1 GFAP and Tubulin Staining Results

Wide area GFAP staining images of the reactive-like astrocytes are shown in Figure 6.17. The observed astrocyte-astrocyte interactions differed significantly as a function of culture surfaces and cell density. Reactive-like astrocytes cultured on PLL glass surfaces (Figure 6.17 (a)), nanofibrillar scaffolds (Figure 6.17 (b)), and Aclar surfaces (Figure 6.17 (c)) were typically not clustered, while the reactive-like astrocytes on the PLL Aclar surfaces (Figure 6.17 (d))

displayed pronounced astrocyte-astrocyte interactions that appeared to recapitulate the chain-like clustering of glial scar formation.

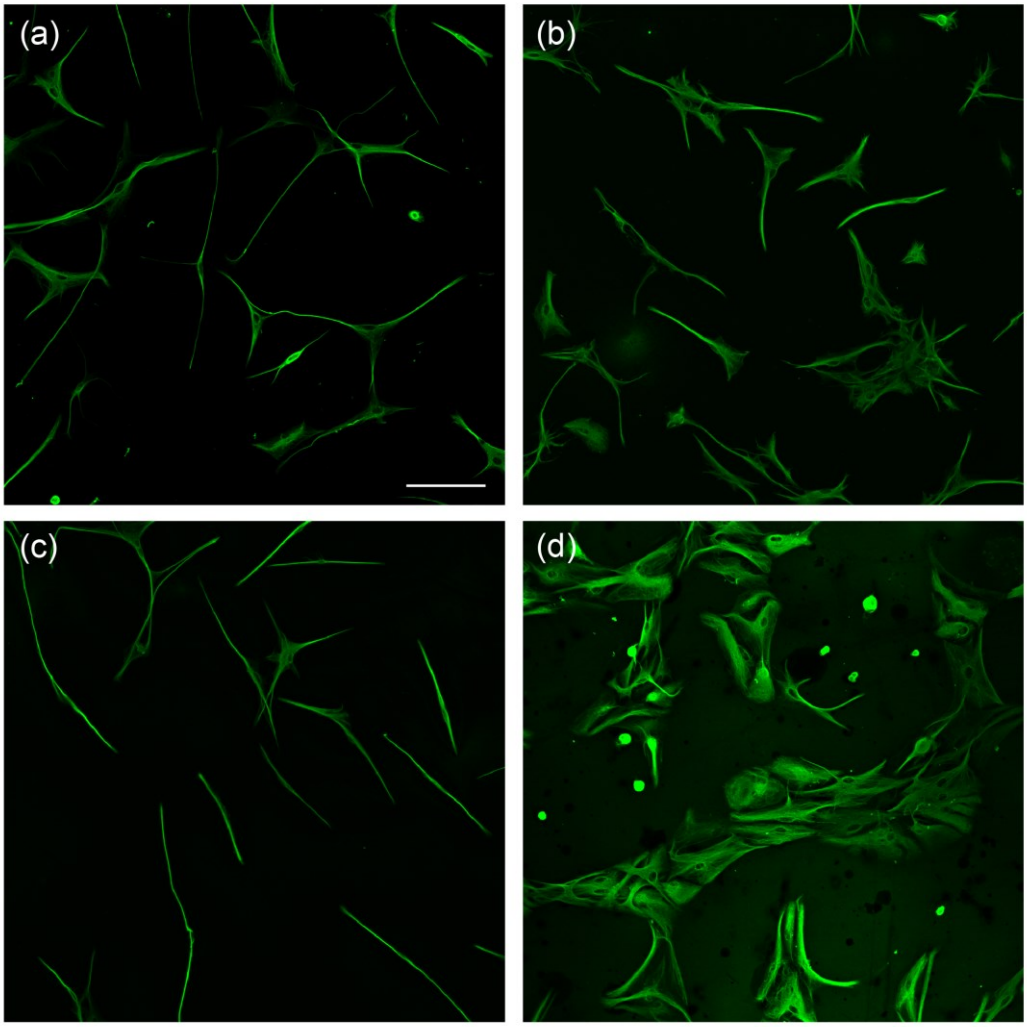

Figure 6.17: Wide area GFAP staining images of reactive-like cerebral cortical astrocytes in vitro. Maximum intensity projection images of reactive-like cerebral cortical astrocytes cultured on (a) PLL glass, (b) nanofibrillar scaffolds, (c) Aclar and (d) PLL Aclar. Scale bar, 100 μm. [117*].

Morphological and biochemical differentiation of reactive-like astrocytes was investigated by GFAP and tubulin staining. Representative GFAP, tubulin, and overlay images with nuclei

staining images of reactive-like astrocytes are shown in Figure 6.18. Overlay images of GFAP and tubulin consistently indicated an interaction between GFAP and tubulin.

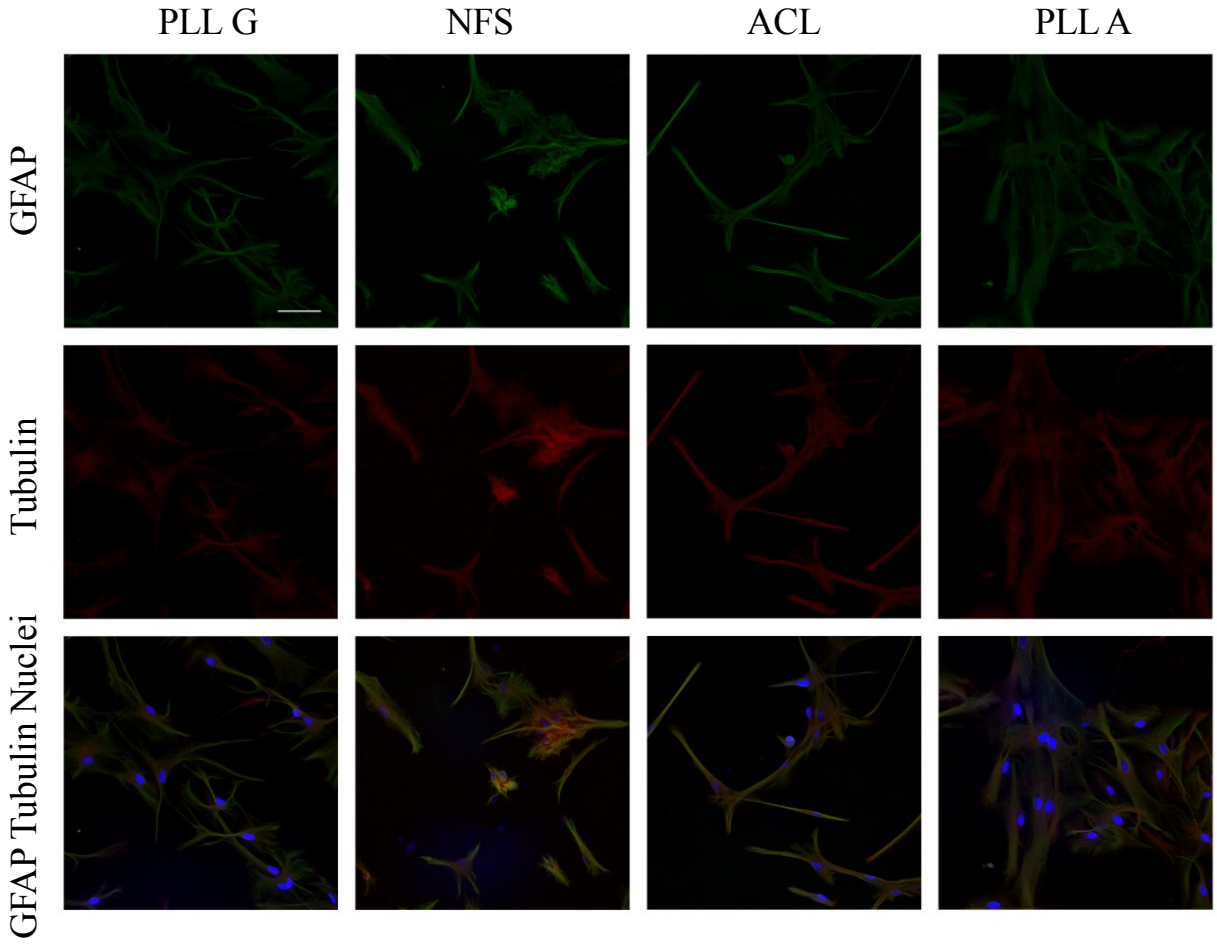

Figure 6.18: Close-up GFAP, tubulin, and DAPI staining images of reactive-like cerebral cortical astrocytes. Maximum intensity projection fluorescence images of astrocytes cultured on PLL glass, nanofibrillar scaffolds, Aclar and PLL Aclar. First, second and third rows show the GFAP, tubulin, and overlaid images of GFAP, tubulin, and nuclei. GFAP, nuclei, and tubulin, were represented in green, blue, and red, respectively. Scale bar, 50 μm. [117*].

6.2.2.4.2 GFAP and Tubulin Quantification Results

The total GFAP and tubulin expression of reactive-like astrocytes was investigated by confocal microscopy z-series. Both total GFAP and tubulin expression were modulated by the culture

surfaces. The results, shown in Figure 6.19, are displayed as mean-value bar graphs with standard error of the mean.

The astrocytes cultured on PLL Aclar had highest expressions of both GFAP (Figure 6.19 (a)) and tubulin (Figure 6.19 (b)). Reactive-like astrocytes cultured on PLL glass displayed comparatively low expression of GFAP but the second highest expression of tubulin. The reactive-like astrocytes cultured on nanofibrillar scaffolds had comparatively higher expression of GFAP but a lower expression of tubulin. Reactive-like astrocytes cultured on Aclar expressed the least amounts of tubulin and the second least amounts of GFAP.

For each surface, significant differences were observed in the total intensity of GFAP among astrocytes cultured on nanofibrillar scaffolds, Aclar, PLL Aclar, and PLL glass. Tukey's all pairs comparison results revealed that the total GFAP intensity of astrocytes cultured on PLL Aclar was significantly higher than PLL Glass ($P < 0.0001$) and Aclar ($P = 0.0386$). Tukey's all pairs comparison also showed that GFAP intensity on nanofibrillar scaffolds was significantly higher ($P = 0.007$) than PLL glass, whereas other pairwise comparisons were not significant.

Significant differences were observed in the intensity of tubulin among astrocytes cultured on the cell substrates. Tukey's all pairs comparison results showed that all pairwise comparisons were significant (max $P = 0.0349$) except nanofibrillar scaffolds versus Aclar.

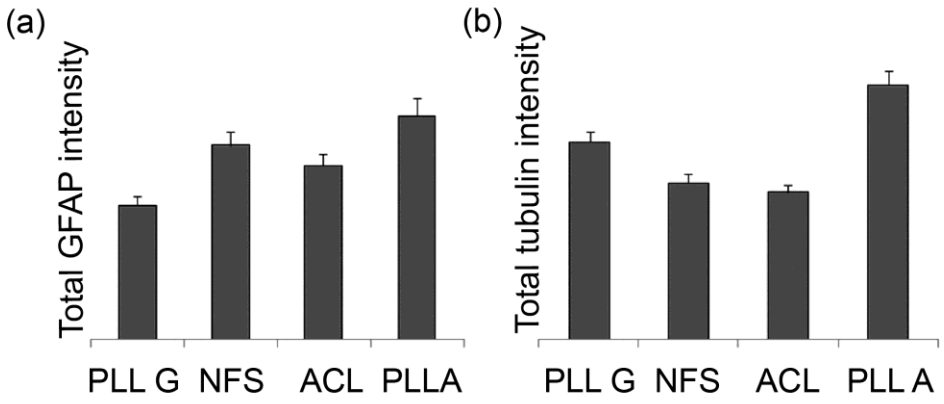

Figure 6.19: Quantitative total GFAP and tubulin expression estimation results for reactive-like astrocytes. Culture surfaces modulate the total GFAP (a) and tubulin (b) expression in reactive-like astrocytes. Error bars show standard error of n=50 cells. PLL G, NFS, ACL, and PLL A, and denote PLL glass, nanofibrillar scaffolds, Aclar, and PLL Aclar, respectively. [117*].

6.2.2.4.3 Cdc42, Rac1, RhoA, and F-actin Immunolabeling Results

The reactive-like astrocytes were immunolabeled by antibodies against Cdc42, Rac1, and RhoA, members of the Rho GTPase family, which are known to be upstream regulators of filopodia, lamellipodia, and stress fiber formation, respectively [78]. Furthermore, inhibition of RhoA effector Kinase (ROCK) through depression of RhoA is associated with the cessation of stress fiber formation and the onset of stellation [93]. Representative results are shown in Figure 6.20 for Cdc42, Rac1, RhoA, with parallel phalloidin staining for F-actin. F-actin staining images showed lack of stress fibers in reactive-like astrocytes for all culture surfaces. Chain-like cell clustering on PLL Aclar was observed from F-actin staining images, as were low cell densities and highly directional cell morphologies on Aclar. The F-actin staining results were therefore consistent with the GFAP staining results. The RhoA intensity on all culture surfaces was dimmer than other protein intensities (Figure 6.20 (c) versus (a) and (b)), which would be consistent with depression of RhoA.

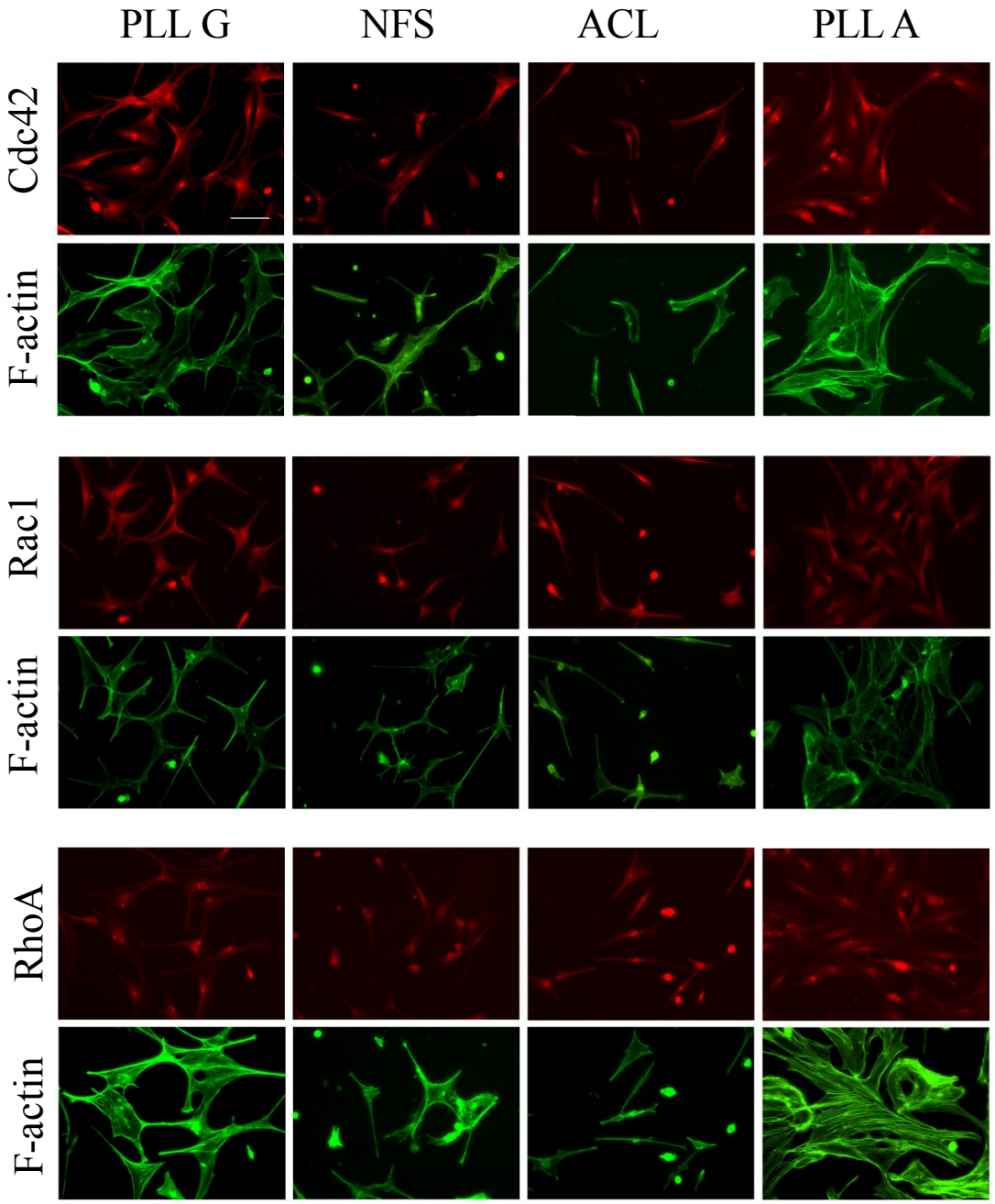

Figure 6.20: Cdc42, Rac1, RhoA, and F-actin staining images of reactive-like astrocytes. Left to right column: fluorescence images of astrocytes cultured on PLL glass, nanofibrillar scaffolds, Aclar, and PLL Aclar. Immunolabeling and corresponding F-actin were represented in red, and green, respectively. Astrocytes were labeled with (a) anti-Cdc42, (b) anti-Rac1, and (c) anti-RhoA. Scale bar, 100 µm. [117*]. Fluorescent images by I. Ahmed, Shreiber laboratory with analysis in this thesis.

6.2.2.4.4 Cdc42, Rac1, and RhoA Quantification Results

Rho GTPase expressions were investigated for statistically significant differences using Tukey's test to perform pairwise comparisons with $P < 0.05$. A total of 20 astrocytes per each culture were selected randomly from both reactive-like and untreated astrocyte samples. The results, shown in Figure 15, are displayed as mean-value bar graphs with standard error of the mean.

For the reactive-like astrocytes alone (Figure 6.21 (a)), RhoA was depressed relative to Rac1 for all culture surfaces, with the greatest differences observed for PLL glass (min $P = 0.0008$) and PLL Aclar (min $P = 0.0002$). This result is consistent with reactive process development through depression of RhoA in dBcAMP-treated astrocytes. The RhoA expression of reactive-like astrocytes was also significantly depressed relative to Cdc42 on PLL Aclar ($P = 0.0175$) and PLL glass ($P < 0.0001$) (Figure 6.21 (a)).

For untreated astrocytes alone (Figure 6.21 (b)), RhoA was significantly depressed relative to Rac1 only for astrocytes cultured on the nanofibrillar scaffolds ($P = 0.0025$). RhoA was also significantly depressed relative to Cdc42 only for astrocytes cultured on the nanofibrillar scaffolds ($P = 0.015$). Both findings were consistent with the previously reported results [12].

For reactive-like versus untreated astrocytes, the Rho GTPase expressions for reactive-like astrocytes were shown to be modulated by the different culture surfaces (Figure 6.21 (a)) in ways that differed from the modulation observed for untreated astrocytes (Figure 6.21 (b)). Comparison of Figure 6.21 (a) and (b) showed that the dBcAMP treatment of astrocytes reversed the relative expression of Cdc42, Rac1, and RhoA on all culture surfaces, except the nanofibrillar scaffolds.

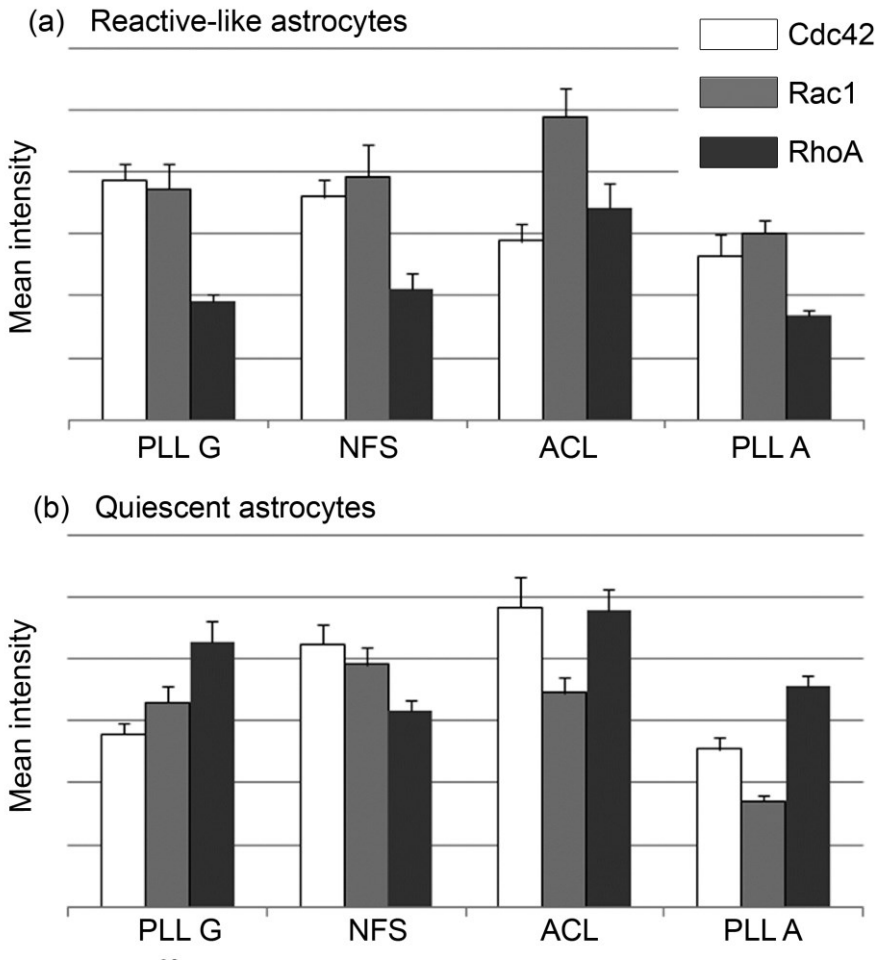

Figure 6.21: Quantitative Cdc42, Rac1 and RhoA expression estimation results for (a) reactive-like and (b) quiescent astrocytes. The white, gray and dark gray bars show the average Cdc42, Rac1 and RhoA intensities, respectively. Error bars show standard error of n=20 cells. PLL G, NFS, ACL, and PLL A, and denote PLL glass, nanofibrillar scaffolds, Aclar, and PLL Aclar, respectively. [117*].

6.2.3 Discussion

In the present work, the effects of culture surface physical properties on the morphological and biochemical differentiation of reactive-like rat cerebral cortical astrocytes were investigated *in vitro*. Additionally, the responses of the reactive-like astrocytes were compared with the responses of untreated astrocytes. Differences in morphology, astrocyte-astrocyte interactions, and immunocytochemistry of astrocytes cultured on four culture surface surfaces: nanofibrillar

scaffolds, and comparative PLL glass, PLL Aclar, and Aclar culture environments were investigated. Four physical properties of the culture surfaces were considered as potentially directive: elasticity, work of adhesion, surface polarity, and surface roughness. The results demonstrated that the morphological and biochemical differentiation of reactive-like astrocytes were modulated by the physical properties of the culture surfaces. Comparison of reactive-like versus untreated responses further demonstrated that the responses were differently modulated by the same culture surface properties.

The present study indicated that nanofibrillar scaffolds reduced the immunoreactivity responses of the reactive-like astrocytes. This was consistently indicated by quantitative morphology assessments, quantitative Rho GTPase expression estimation, and quantitative GFAP and tubulin expression estimation. The quantitative morphology assessments showed that process lengths of reactive-like astrocytes cultured on nanofibrillar scaffolds were significantly shorter than those for reactive-like astrocytes on PLL Aclar and PLL glass (Figure 6.16(a)). Reactive-like and untreated pairwise comparisons also showed that the reactive-like astrocytes developed significantly longer processes, with the *exception* of the ones cultured on the nanofibrillar scaffolds. Furthermore, the pairwise comparisons of the CSI of reactive-like astrocytes showed that the CSI of astrocytes cultured on the nanofibrillar scaffolds was significantly less than the ones of PLL glass and PLL Aclar (Figure 6.16 (d)). Therefore, results from the quantitative morphology assessment indicated that the reactive-like astrocyte response to nanofibrillar scaffolds was similar to the untreated response.

The present study is one of few investigations to combine immunoreactivity proteins with Rho GTPase investigations [121], and the first to compare Rho GTPase investigations of dBcAMP-stimulated and untreated cerebral cortical astrocytes. The dBcAMP-stimulated

astrocyte response to the nanofibrillar scaffolds was unique in that the relative Rho GTPase expressions were unchanged within experimental error while Rho GTPase expressions to the three other surfaces were significantly altered from their untreated expressions.

The dBcAMP-stimulated astrocyte responses to all surfaces showed morphological evidence of stellation with depression of RhoA relative to Rac1, which agrees with the previously reported work [93, 122]. In addition, the lack of stress fiber formation in reactive-like astrocytes, as shown in the Figure 6.20 F-actin staining images, is consistent with the RhoA depression. The quantitative Rho GTPase expression estimation results showed increased expression of Cdc42 for reactive-like astrocytes on PLL glass. The AFM morphology images showed that the reactive-like astrocytes on PLL glass formed nanoscale processes, but actin staining images suggest that those tiny processes are either not filopodia or were below the level of experimental resolution by confocal microscopy.

The immunoreactivity proteins investigation enabled comparison of the amounts of GFAP and tubulin expression among the four culture surfaces. Tubulin and GFAP expressions were both comparatively high for the astrocytes on PLL Aclar surfaces. Comparatively high GFAP expression was observed for astrocytes on the nanofibrillar scaffolds; however, tubulin expression was comparatively low and all other Rho GTPase and morphological responses indicated minimal change from untreated behavior. The overlay of GFAP and tubulin staining images, shown in Figure 6.18, suggested interaction between these proteins. This is consistent with previously reported results [122].

In sharp contrast with the reduction in immunoreactivity responses displayed by reactive-like astrocytes on the nanofibrillar scaffolds, the responses to PLL Aclar exhibited features

reminiscent of glial scar formation. Chain-like clustering of reactive-like astrocytes with interwoven processes was evident in immuno-staining and AFM images. The immunoreactivity investigation demonstrated the largest comparative expressions of both GFAP and tubulin. Furthermore, the most significant depression of RhoA relative to Rac1 was observed for the reactive-like astrocytes on PLL Aclar. The chain-like clustering of reactive-like astrocytes appeared to be induced by the local elastic property of the PLL Aclar surface in combination with the surface polarity property. The directive nature of the elasticity property was indicated by the chain-like versus non-chain-like clustering observed for reactive-like astrocytes on PLL Aclar (soft) versus PLL glass (hard). The directive nature of the surface polarity property was indicated by the chain-like clustering versus the unusual morphology and minimal cell-cell interactions observed for reactive-like astrocytes on PLL Aclar (soft elasticity and high hydrophilicity) versus Aclar (soft elasticity but low hydrophilicity).

It is also interesting to note that the responses of reactive-like astrocytes on PLL Aclar versus PLL glass surfaces differed from the responses of untreated astrocytes on the same culture surfaces. The untreated astrocytes on PLL Aclar surfaces developed extensive filopodia formation that infiltrated along valleys created by the nanoscale surface roughness of these surfaces [12]. The filopodia formation response was not observed on the nanoscale-smooth PLL glass surfaces [12]. For the reactive-like astrocytes, although the surface roughness differences were the same, a glial scar type response was observed instead of filopodia formation. The investigations summarized in Figure 6.12 demonstrated that elasticity differences were also present between the PLL glass and PLL Aclar culture surfaces. Previously reported results [123, 124, 125] have indicated increased sensitivity to local elasticity as a response to wound-healing

situations. Studies of hydrogel-assisted wound healing [125] further suggest that the combination of local elasticity and surface charge may be directive.

The results support the hypothesis that the nanophysical cues of the cell culture surfaces can modulate the morphological and biochemical differentiation of dBcAMP-stimulated cerebral cortical astrocytes. The present study indicated that the properties of the nanofibrillar scaffolds reduced the immunoreactivity responses of the reactive-like astrocytes, while the properties of the PLL Aclar surfaces induced responses reminiscent of glial scar formation. The comparison of reactive-like versus untreated astrocyte responses to elasticity versus surface roughness differences suggested that different nanophysical cues may have more directive importance in a wound-healing situation versus a maintenance situation.

The property investigations and corresponding astrocyte *in vitro* behavior in the present study showed that a combination of tissue scaffold physical properties can modulate cellular mechanisms of reactive-like astrocytes. This suggests that scaffolds with appropriate physical properties could alter the immunoreactivity of astrocytes, which may promote axonal regeneration around a lesion site. The polyamide nanofibrillar scaffolds appear to have the optimum physical properties among the culture surfaces considered in this work. Therefore, it remains as a promising candidate for future *in vitro* and *in vivo* investigations.

6.2.4 Conclusions

The morphological and biochemical differentiation of reactive-like dBcAMP-treated astrocytes cultured on electrospun polyamide nanofibrillar scaffolds, PLL glass, Aclar, and PLL Aclar was investigated by immunocytochemistry, fluorescence, and atomic force microscopy. Four physical

properties of the culture surfaces were considered as potentially directive: elasticity, work of adhesion, surface polarity, and surface roughness. The physical properties of the culture environment were shown to trigger biochemical and morphological consequences for reactive-like astrocytes. The properties of the nanofibrillar scaffolds reduced immunoreactivity responses while the properties of the PLL Aclar surfaces induced responses reminiscent of glial scar formation. The comparison of reactive-like and untreated astrocyte responses suggested that different nanophysical cues may have more directive importance in a wound-healing situation than in a maintenance situation. Local elasticity and surface polarity were indicated as potentially directive for reactive-like cerebral cortical astrocytes.

Chapter 7

AFM Feature Definition for Neural Cells on Nanofibrillar Tissue Scaffolds

7.1 Introduction

The use of AFM in biomedical science has grown rapidly, with recent exciting applications in diverse fields including regenerative medicine (tissue engineering) [14], drug delivery [17], protein folding [126] and clinical medicine [127]. Even so, AFM remains an under-utilized technique within the biomedical research community and more importantly an under-developed enabler of significant new nanoscale biomedical discoveries due to a general problem with inconsistent feature definition. When a feature definition problem is encountered, the standard approach is to use instrument-supplied hardware or software capabilities to resolve it. Deflection imaging (contact mode) or phase imaging (tapping mode) can improve feature definition when changes in cantilever deflection or RMS cantilever oscillation are greatest at boundaries. Alternatively, image processing can be used to extract information that actually exists in an AFM image but is inaccessible prior to processing. Useful filters are a standard component of commercial image processing packages for AFMs, and low pass filtering for noise reduction is a known and popular approach. However for either hardware or software approaches to be successful, it is key to diagnose and accurately identify the nature of the feature definition problem involved. As will be shown, low pass filtering can be the wrong approach to improve feature definition. There has been comparatively little systematic methodology developed for

image diagnosis, other than user experience. This can make the AFM learning curve a lengthy one for new biomedical researchers, especially for certain classes of biomedical problems that have feature definition issues.

In the present work, a severe problem with feature definition of astrocyte neural cells on a promising prosthetic nanofibrillar scaffold for brain and spinal cord injury repair [37, 38] is first diagnosed and then resolved. Recent studies indicate that cells grown on nanofibrillar surfaces that approximate their native extracellular matrix environments behave differently, and in seemingly more biomimetic ways [10, 72]. Many details of the cell-cell and cell-scaffold interactions that may induce the biomimetic response are not presently well known. This is therefore a research area in which the nanoscale resolution capability of AFM could offer significant biomedical insights. The difficulty with AFM investigation is that cells on nanofibrillar surfaces interact with these surfaces via nanoscale edges and processes that are not distinguishable from the nanofibrillar background by height, deflection or phase imaging. This is because the cellular edges and processes are approximately the same order in height as the background nanofibers, ~100 to 200 nm. This problem can be resolved by filtering and present a novel diagnostic approach based on standard AFM section measurements to enable knowledgeable filter selection and design. The requirements for successful image processing were identified as a combination of low frequency component suppression with dynamic range enhancement. This design was implemented to filter the harmonic components present in the images in such a way that the cellular edges and processes became distinguishable from the nanofibrillar backgrounds. The new information revealed in the filtered AFM images would change the biomedical interpretations drawn about the cell-cell interactions present, especially when compared with a more typical analysis of fluorescent microscopy images [83].

7.2 Material and Methods

7.2.1 Neural Cell Culture

Rat cerebral cortical astrocytes were prepared from postnatal day one (P1) Sprague Dawley rats and grown to confluence in astrocyte medium in 75 cm^2 tissue culture flasks as previously described [10]. The astrocyte culture medium was comprised of Dulbecco's Modified Eagle's Medium (DMEM, Invitrogen, Carlsbad, CA) + 10% calf serum (Invitrogen). After reaching confluence (~8-10 days), flasks were shaken overnight on a rotary shaker at 37°C to remove any loosely adherent oligodendrocytes, neurons, or macrophages. Astrocytes were then subcultured in astrocyte medium (0.5 ml) at a density of 50,000 cells/well onto 12 mm coverslips coated with nanofibers in 24 well trays. The astrocytes were maintained for 24 hours (h). The astrocytes were then fixed with paraformaldehyde (4%) and stained with phalloidin [113] for fluorescent microscopy investigation. Phalloidin staining did not affect the AFM imaging.

7.2.2 Nanofibrillar Culture Surface

Randomly oriented polyamide nanofibers (median diameter ~180 nm) were electrospun from a blend [81] of two polymers [$(C_{28}O_4N_4H_{47})_n$ and $(C_{27}O_{4.4}N_4H_{50})_n$] onto plastic ACLAR coverslips (Ted Pella, Reading, CA) by Donaldson Co., Inc. (Minneapolis, MN). Cross-linking of nanofibers was done in the presence of an acid catalyst. The resulting nonwoven polymeric nanofibrillar matrix was approximately 2.0 μm thick when measured on edge by optical microscopy, with no direct openings to the coverslip surface [1, 128].

7.2.3 Epi-Fluorescence Microscopy

Epi-fluorescence microscopy images of astrocyte neural cell cultures at 24 h were captured using a Zeiss Axioplan microscope (Carl Zeiss Microimaging GmbH, Germany). Fluorescence optical microscopy is the most widely utilized technique for cell culture analysis.

7.2.4 Atomic Force Microscopy

AFM images of astrocyte neural cell cultures at 24 h were captured using a Nanoscope IIIA (Bruker AXS Inc, Madison WI, formerly Veeco Metrology) operated in ambient air. Wide-area images showing cell groups were acquired using a J scanner with a maximum scan range of 125 x 125 μm^2 x-y range and ± 2.774 μm z range with the AFM was operated in contact mode, using silicon nitride tips with a nominal tip radius of 20 nm and a cantilever spring constant k = 0.58 N/m. Close-up images of cell-scaffold interactions were acquired using an E scanner with a maximum scan range of 13.5 x 13.5 μm^2 x-y range and ± 1.54 μm z range with the AFM was operated in tapping mode, using etched silicon tips with a nominal tip radius of 10 nm and a drive frequency of ~320 kHz.

7.2.5 Image Processing Methods

Digital image processing techniques were implemented with MATLAB version 7.6.0 (R2008a). Digital images were exported as ASCII files from the Nanoscope Software version 5.30r3.sr3 by converting the units to nm. Four different types of two-dimensional Finite Impulse Response (FIR) digital filters were evaluated in this work: frequency domain Gaussian and Butterworth high pass filters, spatial domain high pass filters and high boost filters. The Gaussian and

Butterworth high pass filters were implemented over frequency domain with normalized cutoff frequencies (ω/π) from 0 to 1 and with integer degrees from 1 to 5. As a final step, histogram equalization was applied for contrast enhancement (MATLAB®, The MathWorks, Natick, MA).

7.2.6 Gaussian High Pass Filter Implementation

Image enhancement in the frequency domain is based on the computation of the two-dimensional discrete Fourier transform (DFT) of the input image, followed by multiplication of the result by a filter transfer function. The final output is obtained by taking the inverse two-dimensional DFT of the product. The fast Fourier transform (FFT), the computationally efficient algorithm [129] for computing DFT, was performed for all of the DFT computations throughout this work.

The two-dimensional DFT of an *M* x *N* pixel image was calculated as:

$$F(u,v) = \frac{1}{MN}\sum_{x=0}^{M-1}\sum_{y=0}^{N-1} f(x,y)\exp\left[-\mathrm{j}2\pi\left(\frac{\mathrm{ux}}{\mathrm{M}}+\frac{\mathrm{vy}}{\mathrm{N}}\right)\right] \quad (7.1)$$

where *x* and *y* are the spatial variables, *f*(*x*,*y*) is the raw image, *u* and *v* are the frequency domain variables, and *F* is the two-dimensional DFT of the *M* x *N* pixel image.

The Gaussian high pass filter (GHPF) transfer function was implemented as:

$$H(u,v) = 1 - \exp\left[-\frac{\mathrm{D(u,v)}^2}{2\mathrm{D}_0^2}\right] \quad (7.2)$$

where D_0 is the cutoff frequency and $D(u,v)$ is the distance from (u,v) to the origin. To apply the GHPF to the image, $F(u,v)$ and $H(u,v)$ were multiplied by array multiplication. $G(u,v)=F(u,v)H(u,v)$ and the inverse two dimensional DFT defined as:

$$g(x,y) = \sum_{u=0}^{M-1} \sum_{v=0}^{N-1} G(u,v) \exp\left[j2\pi\left(\frac{ux}{M} + \frac{vy}{N}\right)\right] \tag{7.3}$$

was applied, and the final GHPF result was obtained.

7.2.7 High Boost Filtering Implementation

High boost, or high-frequency-emphasis, filtering is based on adding a specified percent of the original image to the high pass filtered image [130]. This addition restores the low frequency components that were lost in the high pass filtering operation, so the resulting image may look more like the original image. This was attractive for re-inclusion of cell surface features. A high-boost filter was implemented as:

$$Y = (A-1)O + H \tag{7.4}$$

where Y is the filter output, A is the amplification factor, O is the original image and H is the high pass filtered image.

7.2.8 Histogram Equalization for Contrast Enhancement

A histogram equalization was performed in order to enhance the contrast of the filtered images. The image contrasts were enhanced by transforming the values in the filtered image, so that the

histogram of the output image had a roughly equal number of pixels mapped to each of its 256 levels. The histogram equalization operation converted the low-contrast and dark images to relatively higher contrast and brighter images.

7.3 Results

In this section, the feature definition problem found in distinguishing thin neural cell processes and edges from the tissue culture surfaces that have nanoscale features is identified. The quantitative problem diagnosis procedure is presented next. The optimal filter design based on the problem diagnosis is then given, and finally the biomedical interpretations drawn from analyzing images with missing versus complete information are discussed.

7.3.1 Feature Definition Problem

A composite AFM height image of a three-astrocyte group on a nanofibrillar surface is shown in Figure 7.1 (a). The feature definition is poor for both the cell edges and the cellular processes (extensions with which a cell explores its environment). The structures marked by arrows in the AFM height image of Figure 7.1 (a) could be either nanofibers or cellular processes. Close-ups of potentially important cell-scaffold interactions (dashed box in Figure 7.1 (a)) were investigated by AFM tapping mode phase images. As shown in Figure 7.1 (b) this did not improve the feature definition. The problem is that the cellular edges and processes are approximately the same order in height as the background nanofibers, ~100 to 200 nm.

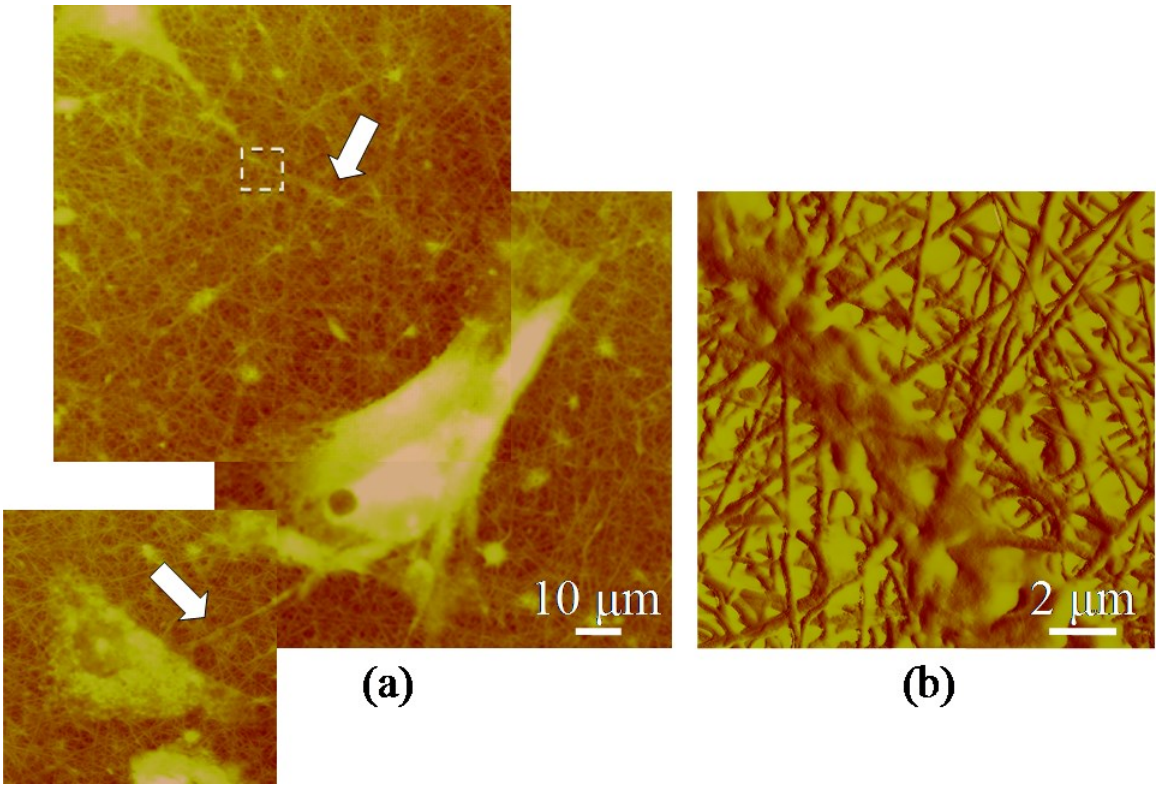

Figure 7.1: Feature definition problems of astrocyte neural cells on nanofibrillar surfaces. (a) The structures marked by arrows in the AFM height image could be either nanofibers or processes. (b) A higher resolution close-up tapping mode phase image of the region shown by dashed box in (a). Its edge features are still unclear. [83*].

7.3.2 Systematic Approach to Problem Diagnosis

A diagnostic approach based on standard AFM section measurements was developed. Individual section measurements of the nanofibrillar surface and an astrocyte cell body are shown in Figure 7.2 (a)/(b) and (d)/(e). A one-dimensional DFT was then applied to the section measurement data of Figure 7.2 (b) and (e). This converted the section measurements into the frequency domain where the harmonic components could be studied and analyzed. The magnitudes of the DFT spectra were then calculated, and the logarithmic DFT spectra were plotted. The logarithmic DFT spectra shown in Figure 7.2 (c) and (f) can be used to identify the key

differences between the cell and nanofibrillar surfaces, which can then be used to create an optimal filter design. In the present case, the differences were:

1. The one dimensional DFT spectra in Figure 7.2 (c) and (f) demonstrated that the amplitude of the zero frequency sample of the cell profile was approximately 5 fold higher than the amplitude of the zero frequency of the nanofibrillar profile. This suggested that attenuation of the zero frequency sample and the other low frequency components with a high pass filter would result in deemphasizing the astrocyte surface relative to the nanofibers so that the astrocyte surface could be distinguished from the nanofibrillar background. This is known as dynamic range enhancement.
2. The nanofibrillar surface had sharper features, meaning more power in the higher frequency harmonics than the astrocyte surface. The high frequency harmonic region above cut-off frequency 0.5 (red dotted lines) had 52% more power than the same frequency region for the astrocyte DFT spectrum.
3. The low frequency harmonics of astrocytes and nanofibers were overlapping in the DFT spectra (Figure 7.2 (c) and (f)). Therefore, total elimination of cell surface information while retaining the nanofibrillar surface information is not possible by filtering techniques. However, because the high frequency components of nanofibrillar surface had more power than the high frequency components of astrocyte surfaces, as shown in Figure 7.2 (c) and (f), amplification of the high frequency components would exaggerate the difference between nanofibers and astrocytes. This is achieved by using a high pass, not a low pass, filter. The results of a preliminary test using a GHPF, shown in space and k-space domains in Figure 7.3, confirmed this approach. When the GHPF surface profiles shown in Figure 7.3 (a) and 7.3 (c) are compared, it can be seen that the nanofibrillar

surface has higher edge features than the astrocytes. Figure 7.3 (b) and 7.3 (d) shows that the high frequency harmonics of nanofibrillar substrate has more power than the high frequency harmonics of astrocyte surface. These quantitative differences are the basis for the subsequent successful filter design.

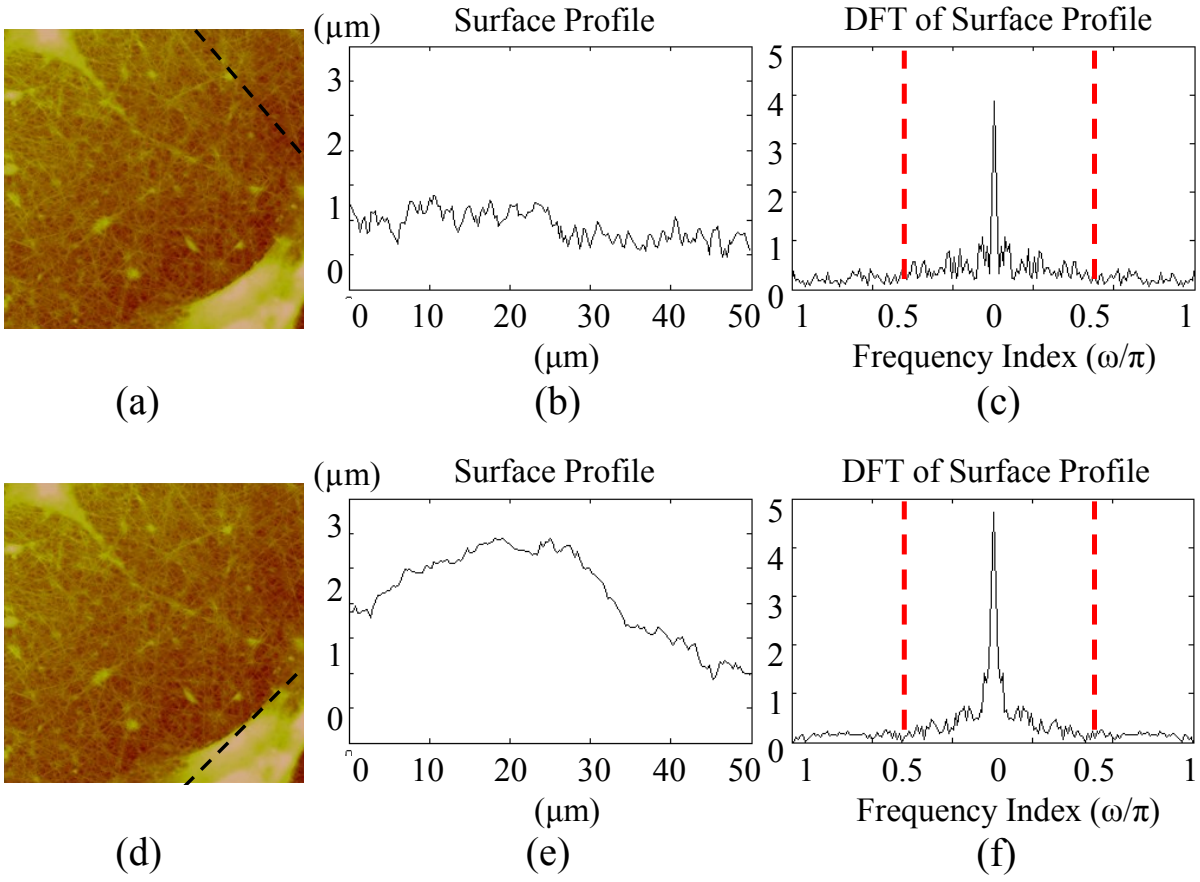

Figure 7.2: (a) Section measurement of nanofibrillar surface along dashed line, (b) corresponding surface profile, and (c) DFT of nanofibrillar surface profile. (d) Section measurement of cell surface along dashed line (e) corresponding surface profile, and (f) DFT of cell surface profile. [83*].

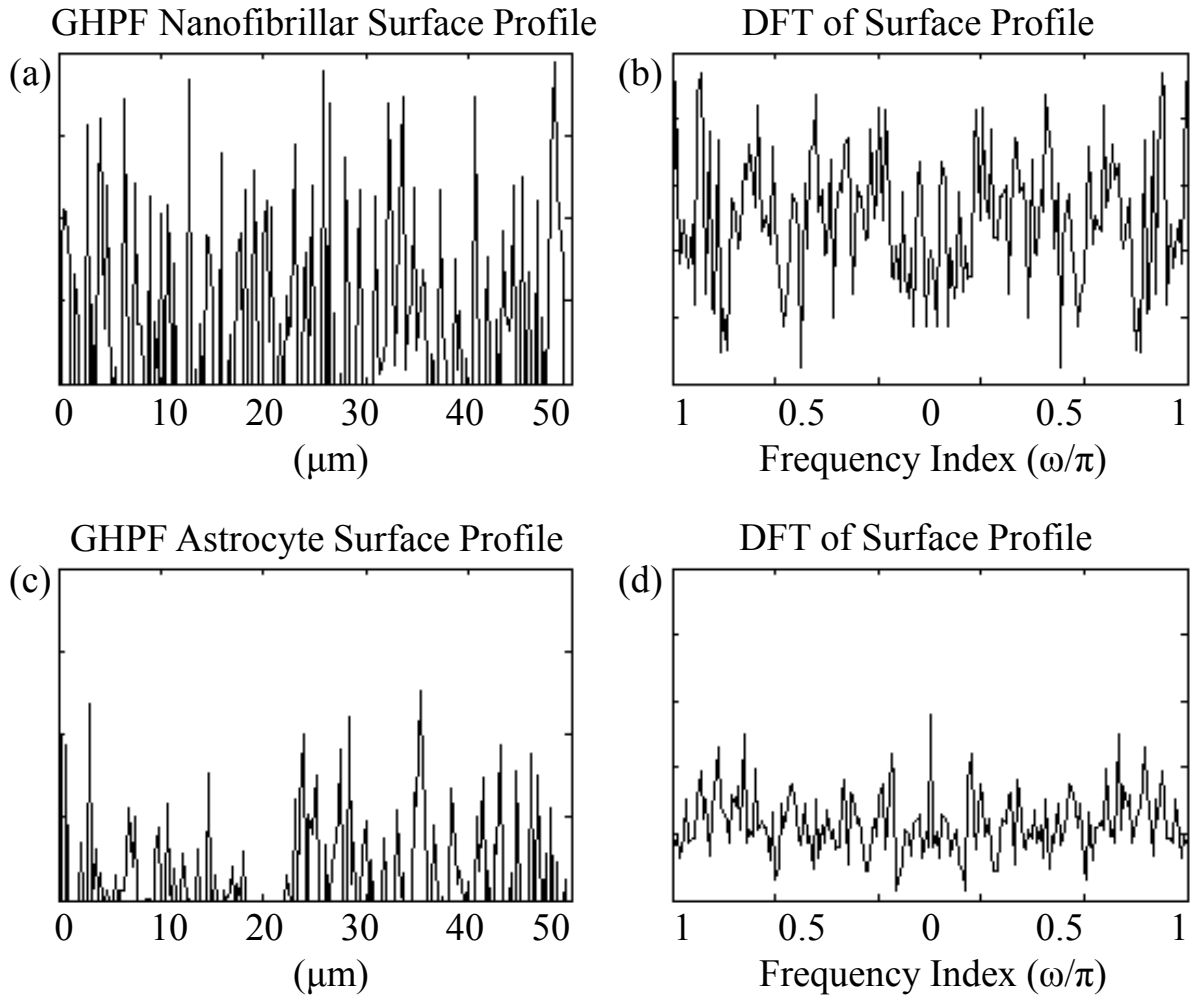

Figure 7.3: GHPF results (a) filtered nanofibrillar surface profile, (b) DFT spectrum of the nanofibrillar surface profile, (c) filtered astrocyte surface profile, and (d) DFT spectrum of the astrocyte surface profile. [83*].

7.3.3 Filter Design Based on Problem Diagnosis

The Gaussian and Butterworth frequency domain high pass filters were implemented by changing the order and the cutoff frequency of the filter. Optimum results were obtained with a GHPF transfer function of order 1 and normalized cutoff frequency 0.5. The perspective plot of the GHPF transfer function of order 1 and normalized cutoff frequency 0.5 is shown in Figure 7.4 (a) and the radial cross section of the transfer function is shown in Figure 7.4 (b). Figure 7.4

(a) shows that the Gaussian frequency domain high pass filter is positional invariant or isotropic. Application of the Butterworth filter yielded noisier results, therefore identifying the optimized GHPF as preferable.

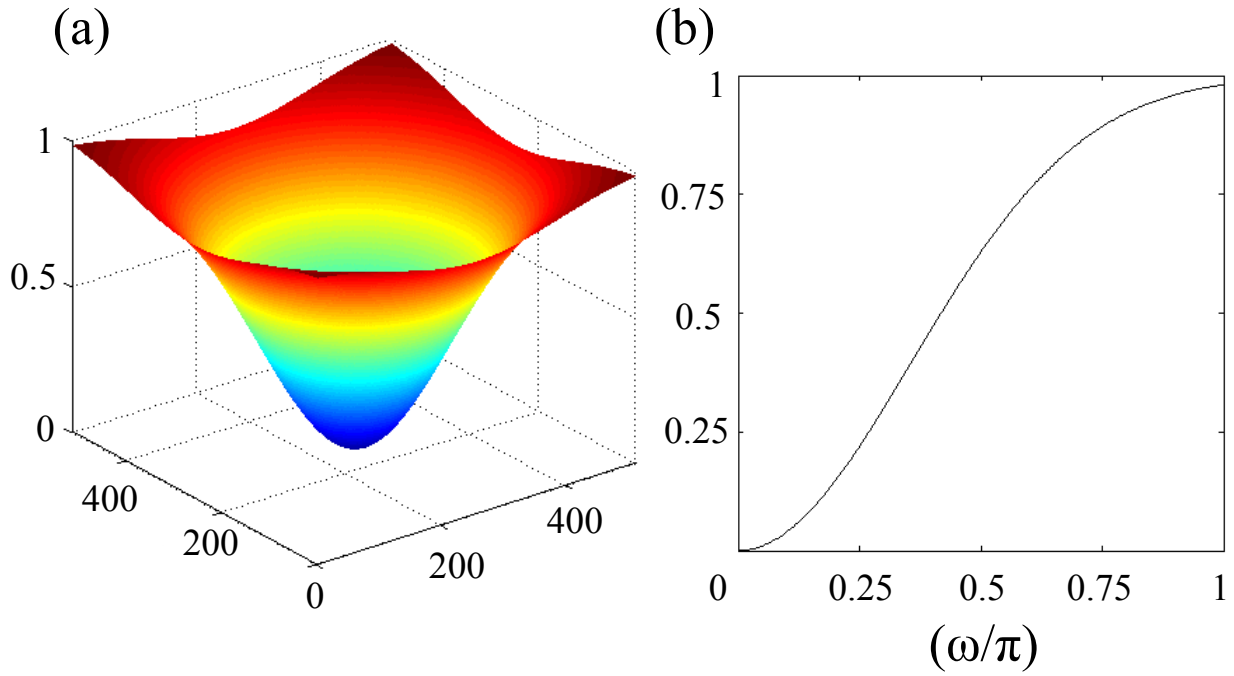

Figure 7.4: (a) Perspective plot and (b) radial cross section of the GHPF transfer function of order 1 and normalized cutoff frequency 0.5. The zero frequency sample is at the center in (a). [83*].

Spatial domain filters were also investigated, both as an alternative to frequency domain filter and for implementation of high boost filtering, a variant of spatial filtering, for return of cell features to filtered images. Spatial domain filters require the specification of a mask. In the present work, 3 x 3, 5 x 5 and 7 x 7 spatial high pass masks were investigated, and 3 x 3 mask size was identified as optimal. High boost filtering was therefore performed using a 3 x 3 spatial high pass mask. Amplification factors of 1.05, 1.10, 1.15 and 1.20 were implemented, and 1.15 was optimum. However, the high boost filtering technique was not successful because return of the %15 of the original image also compressed the dynamic range to the point where cellular edge and process feature definitions were unacceptably reduced. Furthermore, analysis of spatial

domain transfer functions revealed positional anisotropy that would introduce distortions into filtered images of randomly oriented nanofibers. These investigations enabled the systematic selection of the GHPF as best for the investigations.

7.3.4 Biomedical Interpretations Based on Fluorescence Microscopy, AFM and GHPF AFM Height Images

Cell culture protocols include inspection for cell morphology at regular intervals, e.g., at 24 h and 48 h, typically performed using optical microscopy. In a coordinated epi-fluorescence microscopy/AFM investigation [131], a series of images from different regions of the astrocyte-on-scaffold cell cultures were acquired using epi-fluorescence microscopy. The epi-fluorescence microscopy images (Figure 7.5 (a)) indicated that the astrocytes were stellate but largely isolated from each other at 24 h. AFM height image of astrocytes cultured on nanofibrillar surfaces, shown in Figure 7.5 (c), would not contradict the conclusion that the cells were stellate and largely isolated at 24 h. However, the clear feature definition of cellular edges and processes obtained by application of the GHPF filter, shown in Figure 7.5 (b), demonstrated that significant leading edge formation beyond the previously assumed process ending had occurred at 24 h. The high boost filtering result shown in Figure 7.5 (d) demonstrates that loss of dynamic range enhancement by inclusion of as little as 15% of the original image resulted in loss of feature definition to a level comparable to that of an unfiltered AFM image.

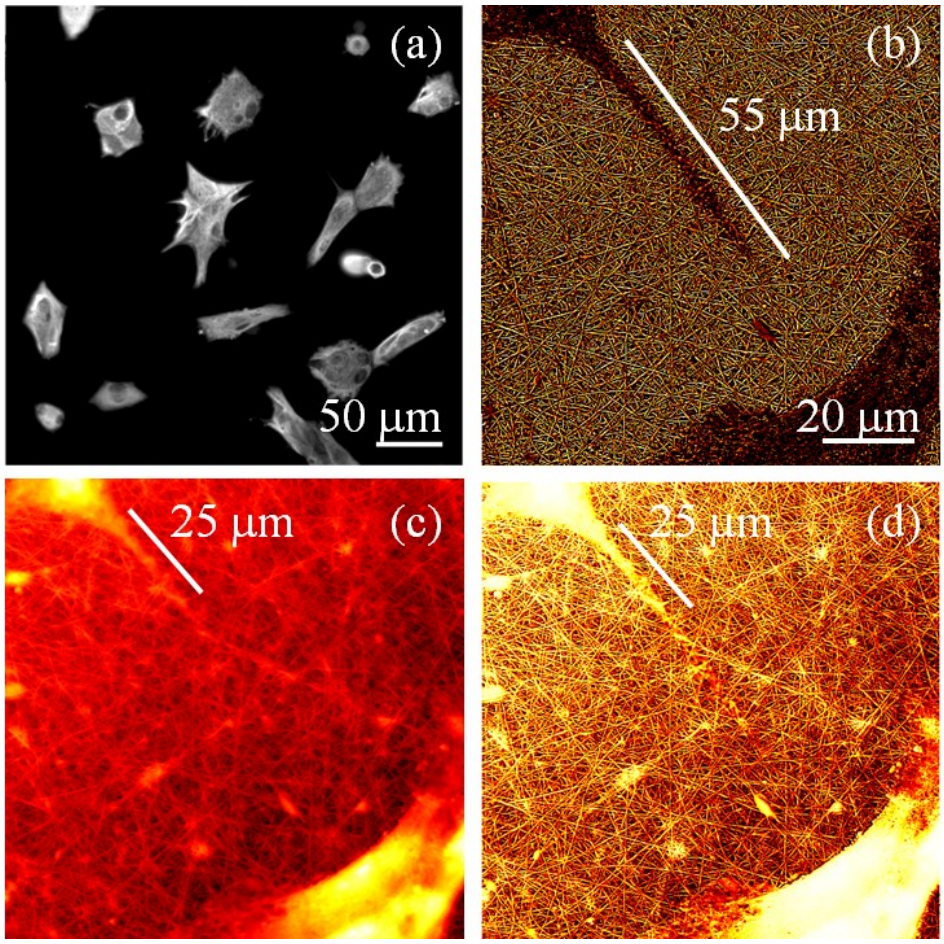

Figure 7.5: (a) Epi-fluorescence microscopy image of "isolated" astrocytes at 24 h. (b) GHPF AFM image revealed significant leading edge formation. (c) Unfiltered AFM image did not show full extent of leading edge formation. (d) Inclusion of 15% of original image in high-boost filtering resulted in loss of feature definition to a level comparable to unfiltered AFM image. [83*].

The unfiltered height image of Figure 7.1 (a) is reproduced in Figure 7.6 (a) and compared with its GHPF equivalent in Figure 7.6 (b). In addition to the long process described in Figure 7.5, the filtered image revealed a second complete cellular bridge that extended between the "isolated" cells. Direct contact via cellular bridges has implications for inter-cellular information exchange [132] and, using the methods developed in this paper, this is the first time to report this possibility for neural cells on nanofibrillar surfaces.

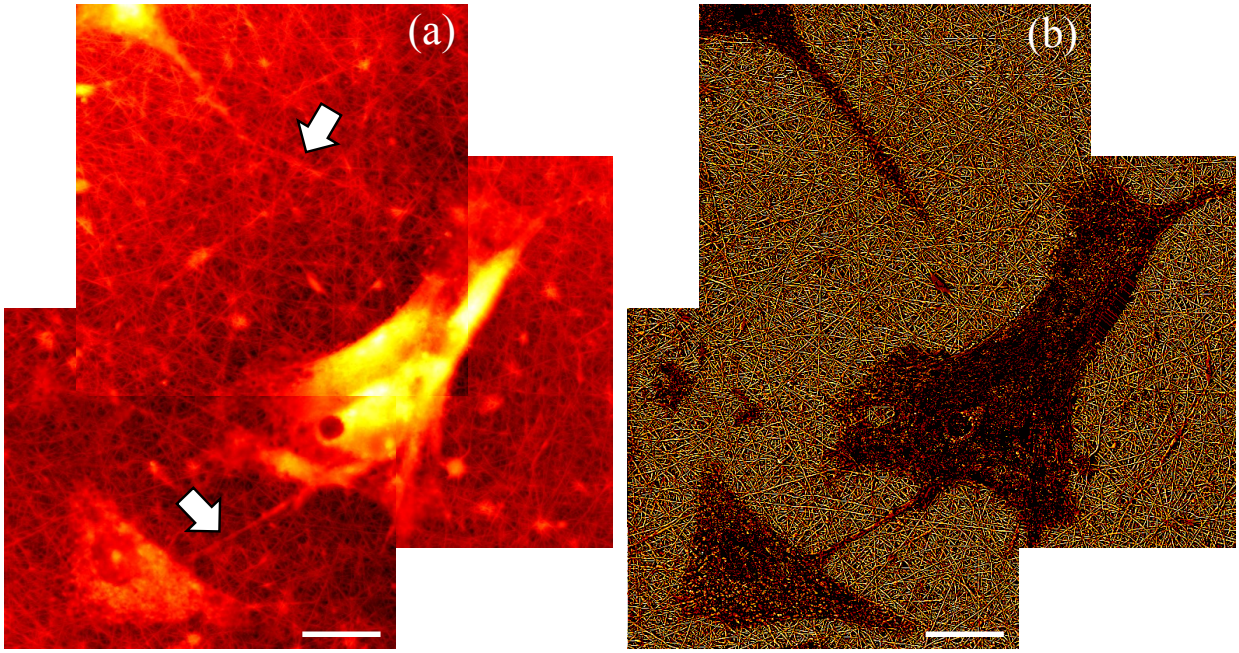

Figure 7.6: In the composite AFM height image (a), cellular processes and cell edges are indistinguishable from the nanofibrillar background. (b) In the GHPF result, the cellular edges and processes are clearly distinguished from nanofibrillar scaffold. Scale bars, 20 μm. [83*].

7.4 Discussion

In this work, DFTs of standard AFM section measurements of astrocytes versus nanofibrillar surfaces were used as the basis for the diagnosis of the feature definition problem. These showed that the high frequency components of nanofibrillar surface had more power than the high frequency components of astrocyte surfaces and identified the use of a frequency domain high pass filter as the potential solution to the feature definition problem. Such a filter has two advantages. The high frequency components of the nanofibrillar surface are amplified, making them easier to distinguish from the cellular features. Furthermore, suppression of the low frequency components yields a dynamic range enhancement of the image. The diagnostic conclusions were therefore that the combination of dynamic range enhancement with low

frequency component suppression that could be achieved through frequency domain high pass filtering would be likely to enhance feature definition of cellular edges and process relative to nanofibrillar tissue scaffolds. A GHPF filter of appropriate degree and cutoff frequency was designed and used to selectively emphasize the high frequency harmonics that belonged to nanofibers of the tissue culture scaffold, enabling the nanoscale cellular edges and processes to be distinguished from nanofibrillar surfaces. The high boost filtering technique, although attractive for inclusion of cell surface features, was not successful in the problem because the return of as little as 15% of the original image also compressed the dynamic range with unacceptable loss of cellular feature definition relative to the nanofibrillar surface. The information needed for clear feature definition was contained in the AFM images all along. The problem was not a damaged or dirty tip, or poor tracking.

The GHPF filter of the present study was successfully applied to more than 250 contact and tapping mode AFM height images of cerebral cortical astrocytes cultured on poly-L-lysine functionalized glass, nanofibrillar scaffolds and fibroblast growth factor-2 derivatized nanofibers; and also cerebellar granular neurons cultured on nanofibrillar scaffolds and poly-L-lysine functionalized glass. While this suggests that the GHPF filter with selected degree and cutoff frequencies has general utility in cell culture investigations, the major emphasis of this study is on the simple diagnostic approach that identified it. The diagnosis and custom filter design approach presented here expands user options beyond the selection supplied with the instrument or towards more knowledgeable use of instrument supplied filters. It also enables the user to connect with the growing body of work in image enhancement methods for AFM images for biological samples [133], for non-biological samples [134], and in general [135, 136, 137].

The electrospun polyamide nanofibrillar matrices of the present study have shown promising results for spinal cord repair [38]. There are many other types of nanofibrillar prosthetics currently under investigation for different injury repair situations, including self-assembling peptide nanofibers [138], porous hydrogels [139], self-assembling nanofibrous gels [140] and ECM allografts [141]. Many potentially significant details of the cell-cell and cell-scaffold interactions are not presently known and the nanoscale resolution of AFM could offer significant biomedical insights. However, AFM investigation of cells on any of these surfaces would encounter the same problem described in the present work: that the dynamic range of the captured images is insufficient to allow thin ~20-100 nm layers of cytoplasm to be distinguished from ~100-200 nm nano-featured surfaces.

GHPF AFM height images revealed that these nanofibrillar surfaces enable the development of previously unknown astrocyte cell-cell interactions by 24 h, which provides new information for ongoing investigations of why cells cultured on nanofibrillar surfaces seem more biomimetic. The same techniques were successfully applied for cerebellar granular neurons cultured on nanofibrillar surfaces, and should be useful in similar investigations, e.g., cardiomyocytes on nanofibrillar surfaces. The methods developed here can therefore extend the usefulness of AFM nanoscale imaging in regenerative medicine.

Chapter 8

A new AFM Based Cell Shape Index for Quantitative Cell Spreading and Stellation Investigation

8.1 Introduction

A cell shape index (CSI) is a measure of the morphological differentiation of a cell that is used to provide a quantitative comparison between cells. *In vivo,* cells have different morphologies depending on their type and environment, e.g., astrocytes have a stellate morphology in the central nervous system (CNS) to allow neuron and capillary interactions [142] while endothelial cells in heart arteries have an elongated morphology with actin and microtubule fibers aligned parallel to the direction of blood flow [143]. *In vitro*, cells also have different morphologies depending on their type and environment, and recent studies have used quantitative cell shape investigations to explore the potentially significant directive impact of environments for healthy or pathological cellular outcomes [12, 116, 144, 145, 146].

A conventional CSI is the ratio of perimeter squared to the cell projection area [142]:

$$CSI = P^2 / (4 \pi A) \tag{8.1}$$

where P is cell perimeter, and A is the cell projection area. This equation describes stellation as a cell's departure from a circular cross section since:

$$(2 \pi r)^2 / 4 \pi (\pi r^2) = 1 \tag{8.2}$$

The conventional CSI has been previously used to provide two-dimensional shape information of astrocytes [142] and vascular endothelial cells [143]. However, this definition for CSI, which was created for use with two-dimensional optical microscopy images, does not include three-dimensional effects, e.g., cell-spreading or hypotonic swelling.

New research directions are actively being pursued to enhance the usefulness of cell shape analysis in biomedical research. Two important directions are research to incorporate three-dimensional information and research to segment cells for CSI analysis. Addressing the former, Canham and Burton have proposed a "sphericity index" for the study of human red blood cells [147]. Chvátal *et al.* has recently developed a three-dimensional cell morphometry definition for use with z-series confocal microscopy images [148]. Tiryaki *et al.* has recently developed a new CSI that incorporates volumetric information acquired from high-resolution AFM height images of cells on culture surfaces [120]. Addressing the segmentation issue, CSI analysis is a revealing but currently under-utilized approach because CSI calculation requires a clearly defined cell perimeter. Automatic extraction of cell boundary information using, e.g., NIH Image J 1.46r is limited to isolated cells with perimeters that display sharp contrast. In recent work by Pincus and Theriot [149], a mask and template matching approach was innovatively applied to confluent cells in culture to create an accurate numerical two-dimensional representation for individual cells with extractable boundaries.

In the present work, the new CSI definition based on analysis of high-resolution AFM images is used [120] and additionally incorporate a new cell segmentation algorithm that uses a new multi-dimensional texture analysis to segment cells from substrate regions. The cell area and cell contours are found automatically without user bias. Segmentation of cells from substrate regions is important for CSI analysis applied to cells cultured on the new, biomimetic substrates

as nanofibrillar [10] or hydrogel scaffolds, which have with significant surface features. AFM images retain volumetric information such as cell spreading for cells cultured on surfaces, making the new CSI segmentation and analysis system appropriate for investigations of substrate-adherent cell cultures and surface seeding of three-dimensional matrix cultures.

The new AFM-based CSI segmentation and analysis system is applied to analysis of the responses of untreated and dBcAMP-treated reactive-like astrocytes to the nanophysical cues provided by four culture environments including polyamide nanofibrillar scaffolds. Astrocyte responses to polyamide nanofibrillar scaffolds appear to favorably modulate the glial scar response that blocks axon regeneration in CNS traumatic injury [37, 38]. AFM studies [12] have identified that responses include cell spreading as well as process formation, and that the cell spreading can vary depending on the surface polarity of the cell substrate. In the present work, the new CSI segmentation and analysis system is used to perform the first quantitative cell spreading and stellation response investigation for astrocytes in response to (1) changes in nanophysical environment cues, and (2) untreated versus reactive-like states of astrocytes.

8.2 Experimental Procedures

8.2.1 Preparation of samples

Four culture surfaces were investigated in this work: PLL glass, PLL Aclar, Aclar and polyamide nanofibrillar scaffolds. Glass coverslips (12 mm, No. 1 coverglass, Fisher Scientific, Pittsburgh, PA) and Aclar coverslips (12 mm, Ted Pella, Redding, CA) were used as underlying surfaces for the PLL functionalization. Glass or Aclar coverslips were placed in a 24-well tissue culture plate (one coverslip/well) and covered with 1 mL of poly-L-lysine (PLL) solution (50 μg PLL/mL in

dH_2O) overnight. The coverslips used for the cultures were then rinsed with dH_2O and sterilized with 254 nm UV light using a Spectronics Spectrolinker XL-1500 (Spectroline Corporation, Westbury, NY). The polyamide nanofibrillar scaffolds electrospun on Aclar substrates were obtained from Donaldson Co., Inc. (Minneapolis, MN) and Corning Life Sciences (Lowell, MA). The fiber diameter for the nanofibrillar scaffolds has a range from 100 to 300 nm.

Primary untreated and reactive-like astrocyte cultures were prepared as previously reported [115, 150]. The astrocytes cultured on coverslips were fixed in 4% paraformaldehyde for 10 minutes, rinsed with distilled water and air-dried. All cells in this study were fixed at 24 h, at which time cells were either isolated or in small clusters.

Astrocyte responses to the nanofibrillar surfaces were studied in comparison with their responses to three additional culture surfaces: poly-L-lysine-functionalized planar glass (PLL glass), unfunctionalized planar Aclar (Aclar), and PLL-functionalized planar Aclar (PLL Aclar). PLL glass is a standard astrocyte culture surface, and astrocyte responses to it are well characterized, making it useful for identifying differences in astrocyte responses to other surfaces. The polyamide nanofibrillar scaffolds were electrospun on Aclar substrates; therefore, astrocyte responses to Aclar surfaces were investigated to distinguish responses to the nanofibrillar scaffolds from possible responses to the underlying Aclar substrate. Astrocyte responses to PLL Aclar surfaces were studied to clarify the role of the underlying substrate versus surface functionalization. The four culture surfaces were previously characterized [12, 116] in terms of four of the nanophysical cues that they presented: local surface roughness, local elasticity, local work of adhesion and global surface polarity.

8.2.2 Analytical techniques

The AFM investigations were performed using a Nanoscope IIIa (Bruker AXS Inc, Madison WI, formerly Veeco Metrology) operated in contact mode and in ambient air. A J scanner with 125 μm x 125 μm x 5.548 μm x-y-z scan range, and Bruker DNP silicon nitride probes with a 35º ± 2º cone angle and a nominal 20 nm tip radius of curvature were used for the AFM investigations. For each culture surface, a minimum of 50 images were captured from different regions of at least three different cell substrates. The AFM height images are 512x512 and 256x256 pixels as identified in the text with 16 bit gray level depth. In this work, the field of view of the images was 100 μm x 100 μm. Cell segmentation for both the conventional and new CSI calculations was implemented with MATLAB version 7.7.0 (R2012b) (The MathWorks, Natick, MA) using the neural network and image processing toolboxes.

Cell segmentation was performed automatically by texture segmentation. The AFM height data was exported as an ASCII file, and the textural features were extracted from the height and the Gaussian High-Pass Filtered height image. For comparative culture surfaces, Aclar, PLL Aclar and PLL glass, the cell and substrate surface training data was determined manually. The cell boundaries on nanofibrillar scaffolds are not easily distinguishable. Therefore, for astrocytes on nanofibrillar scaffolds the cell surface training data features were collected from AFM cell culture images, and scaffold surface data features were collected from bare nanofibrillar scaffold AFM images to ensure correct training data. A total of 28 types of textural features were extracted from AFM height images, and are listed in Table 8.1. The textural features were extracted from each pixel of the image, and the moving window size was set to 5x5 for local statistics textural features. The texture measure A and GHPF textural features were calculated as described in Ref [151] and Ref [83]. Sequential forward selection (SFS) and sequential floating

forward selection (SFFS) feature selection algorithms [152] were used to select features and reduce the computational cost for segmentation. The texture features were then used to classify each pixel of the AFM image either to cell or cell substrate region via a two-hidden-layer feedforward neural network with resilient backpropagation algorithm [153]. The number of training iteration was set to 30 times the number of input features to prevent the overtraining of the classifier. The number of hidden nodes was approximately 10% of the number of training patterns. For target values, each digit was encoded with +1 and -1 values to improve performance of the classifier. After segmentation, the morphological close operation was used to remove the noise. The small regions in the segmented image which are less than 1% of the whole image were eliminated. The segmented image was used to calculate the conventional and new CSI. In this work, the cell segmentation method was not intended for finding the boundaries of cells in clusters. The boundaries of cells were outlined manually when the cells were clustered. The segmentation performance on PLL Aclar surfaces was low. When 7x7 pixels moving window was used, the accuracy was 85%. Therefore, the segmentation was done manually when needed.

GLCM is a statistical method of extracting texture features from images. It is a tabulation of how often different combinations of pixel brightness values occur in an image [154]. The texture idea came from Haralick's paper [155]. In this work, a subset of 28 textural features derived from two models: the gray level co-occurance matrix and local statistics texture features were used to classify cell region versus cell substrate region. The 28 textural features are listed in Table 8.1.

Table 8.1: The textural features used to segment the cell surface from the cell substrate. (STD: standard deviation; GHPF: Gaussian high pass filter; GLCM: gray level co-ocurance matrix; IMC1: information measure of correlation 1; IMC2: information measure of correlation 2.

#	**textural feature**	**model**		#	**textural feature**	**model**
1	mean	local statistics		15	inverse difference moment	GLCM
2	STD	local statistics		16	sum average	GLCM
3	mean by STD	local statistics		17	sum variance	GLCM
4	GHPF	local statistics		18	sum of variances	GLCM
5	texture measure A	local statistics		19	sum entropy	GLCM
6	entropy	local statistics		20	entropy	GLCM
7	skewness	local statistics		21	difference variance	GLCM
8	kurtosis	local statistics		22	difference entropy	GLCM
9	power spectrum	local statistics		23	IMC1	GLCM
10	local binary partition	local statistics		24	IMC2	GLCM
11	contrast	GLCM		25	dissimilarity	GLCM
12	correlation	GLCM		26	inertia	GLCM
13	energy	GLCM		27	cluster shade	GLCM
14	homogeneity	GLCM		28	cluster prominence	GLCM

8.2.2.1 Astrocyte Morphology Investigation by Conventional CSI

After segmentation, the conventional CSI definition given in equation 1 was used to investigate the quantitative morphometry of the cerebral cortical astrocytes cultured on the four different culture surfaces that presented different nanophysical cues [120]. The conventional CSI measures were investigated for statistically significant differences using Tukey's test pairwise comparisons with $P < 0.05$.

8.2.2.2 Astrocyte Morphology Investigation by New AFM-based Cell Shape Index

The new CSI that includes volumetric information extracted from AFM images of cells on surfaces is defined as:

$$\text{New CSI} = (1/18\ \pi) \times (SA_{cell})^3 / (V_{cell})^2 \quad (8.3)$$

where SA_{cell} is the cell surface area, and V_{cell} is the cell volume. This assumes that the cell is resting on, not penetrating, a surface. For a hemispherical "cell" on a surface, the new CSI is:

$$(1/18\ \pi) \times (0.5[4\pi r^2])^3 / (0.5[4/3\ \pi r^3])^2 = 1 \quad (8.4)$$

Therefore, the new CSI increases as the cell morphology become more stellate and/or the cell spreading increases.

After cell segmentation from the cell substrate, the surface area of each cell was calculated by splitting the AFM topography faces into triangles. The area of a triangle in three-dimensional space was computed using the cross product given by:

$$SA_{triangle} = 0.5\ |(v_2 - v_1) \times (v_3 - v_1)| \quad (8.5)$$

where $SA_{triangle}$ is the area of a triangle on the cell surface, and the coordinates of the vertices are given by $v_i=(x_i, y_i, z_i)$. The surface area of each triangle was then computed over the segmented cell area, and cell surface area was obtained. The volume of each astrocyte was calculated by assuming each pixel and its z coordinate as a square prism [156]. The volume under each pixel was computed by multiplying the unit pixel area by the height of that pixel. This was repeated for all the pixels of the segmented cell region. The base level for all culture

surfaces was assumed to be a planar surface. The base level for planar culture surfaces was determined taking the average of the user-defined culture surface region. The base level for the nanofibrillar scaffolds was determined similarly except when the average value of the culture surface is not lower than the minimum height point on the cell region, the base level was assumed to be 10 nm (the thickness of cell membrane) lower than the minimum height point on the cell region. The new CSI was computed as given in equation 8.3. Departure from unity reflects the average departure from a three-dimensional hemispherical volume by both stellation and cell spreading.

8.3 Experimental Results

8.3.1 Initial Segmentation Step

CSI analysis requires mathematical segmentation of cell from the cell substrate. The difficulty of segmentation varies depending on the cell and the substrate. In this work, the cell segmentation on nanofibrillar scaffolds and PLL Aclar surfaces were more challenging than the PLL glass and Aclar surfaces. Cells on nanofibrillar scaffolds interact with these surfaces via nanoscale edges and processes that are not distinguishable from the nanofibrillar background by AFM height, deflection, or phase imaging. This is because the cellular edges and processes are approximately the same order in height as the background nanofibers, ~100 to 200 nm. This difficulty was overcome by using GHPF as described in detail [83].

The textural features of astrocytes and PLL Aclar surface were similar which reduced the segmentation performance. The surface roughness of PLL Aclar surfaces was higher than other cell substrates when the surface roughness values were measured from individual nanofibers [3].

The surface roughness of the cell region has a lot of variance because of the many different types of protein assemblies, glycoproteins, cell protrusions, and ion channels on astrocyte membrane. Therefore, in terms of surface roughness, the cell and the PLL Aclar surfaces were closer than other cell substrate surfaces. This explains the reason of the difficulty in segmenting the cell region from the PLL Aclar surfaces.

In previous work, a diagnostic approach based on analysis of discrete Fourier transform of standard AFM section measurements was developed and used to identify quantitative differences in the frequency components of nanoscale cellular edges and processes of neural cells cultured on nanofibrillar scaffolds. Accurate identification of differences formed the basis for the subsequent successful Gaussian high-pass filter (GHPF) design that enabled the edges and processes to be clearly distinguished in AFM images. In the present work, the GHPF was applied to AFM height images and followed by histogram equalization. The final cell boundaries were determined by manual segmentation. The results of the segmentation procedure steps for a representative astrocyte AFM height image were shown in Figure 8.1 (a)-(c).

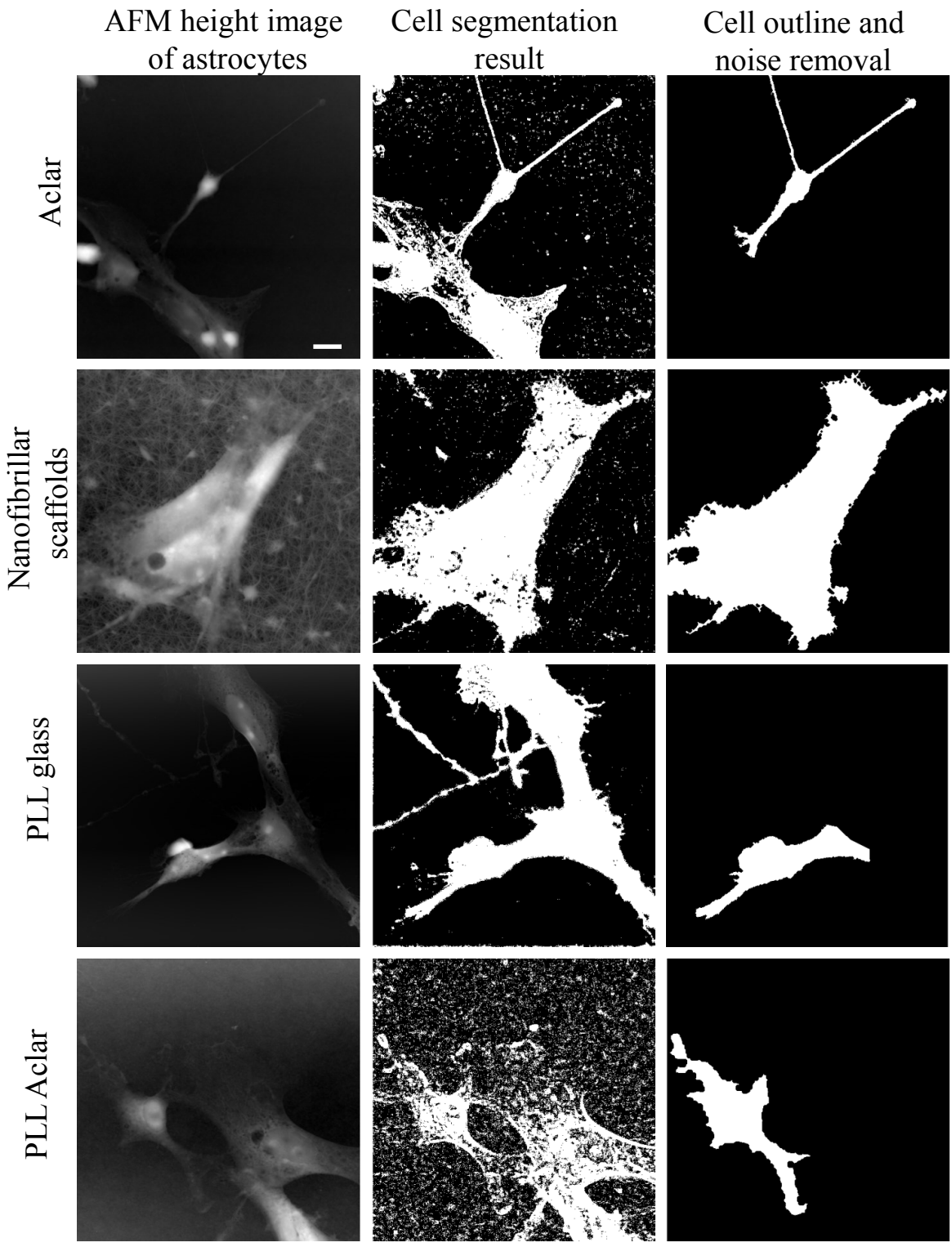

Figure 8.1: The segmentation procedure results of AFM height images of an astrocyte cultured on cell substrates. AFM height images of the astrocytes (left column), the segmentation results (middle column), and individual cell area outlines (right column). Scale bar, 10 μm.

8.3.2Astrocyte Morphology Investigation by Conventional CSI

After segmentation, the conventional CSI definition given in equation 8.1 was used to investigate the quantitative morphometry of the cerebral cortical astrocytes cultured on the four different culture surfaces that presented different nanophysical cues. At 24 h, astrocytes on all substrates exhibited variation in their morphologies. The conventional CSI results, shown in Figure 8.2, indicated that untreated astrocytes cultured on Aclar surfaces are more stellate than the ones on other surfaces. The astrocytes on PLL glass and nanofibrillar scaffolds became more stellate when they were treated by dBcAMP, whereas other astrocytes did not.

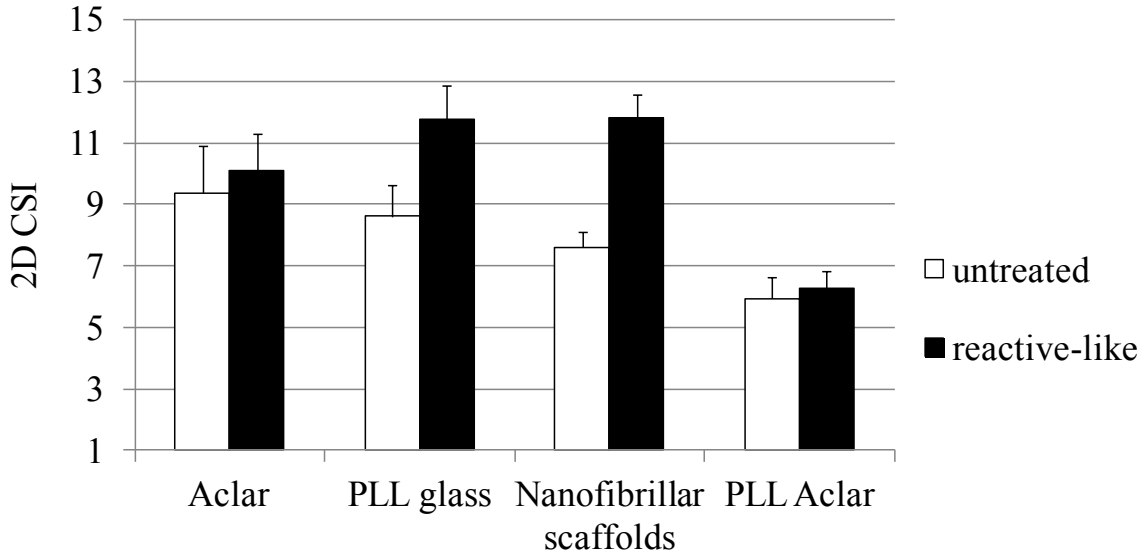

Figure 8.2: The conventional CSI results of untreated and reactive-like astrocytes cultured on Aclar, PLL glass, nanofibrillar scaffolds and PLL Aclar. Error bars show standard error.

8.3.3 Astrocyte Morphology Investigation by New AFM-based Cell Shape Index

The new CSI results shown in Figure 8.3 indicated that untreated and reactive-like astrocytes cultured on the nanofibrillar scaffolds had the lowest CSI values. This implies that, with the same stellation counted in the new CSI, there is also dominant low spreading behavior. The other astrocyte group with low CSI values was on Aclar. AFM and phalloidin staining results [12] confirmed that astrocytes cultured on Aclar surfaces were significantly more hemisphere-like than the ones on other substrates. The new CSI results further indicated that the astrocytes cultured on the two PLL functionalized surfaces were similar in terms of combined cell spreading and stellation possibly due to PLL functionalization. The new CSI of astrocytes on PLL glass reduced when the astrocytes became reactive-like, whereas the ones of PLL Aclar were increased. This result may be due to the different elastic property of cell substrate.

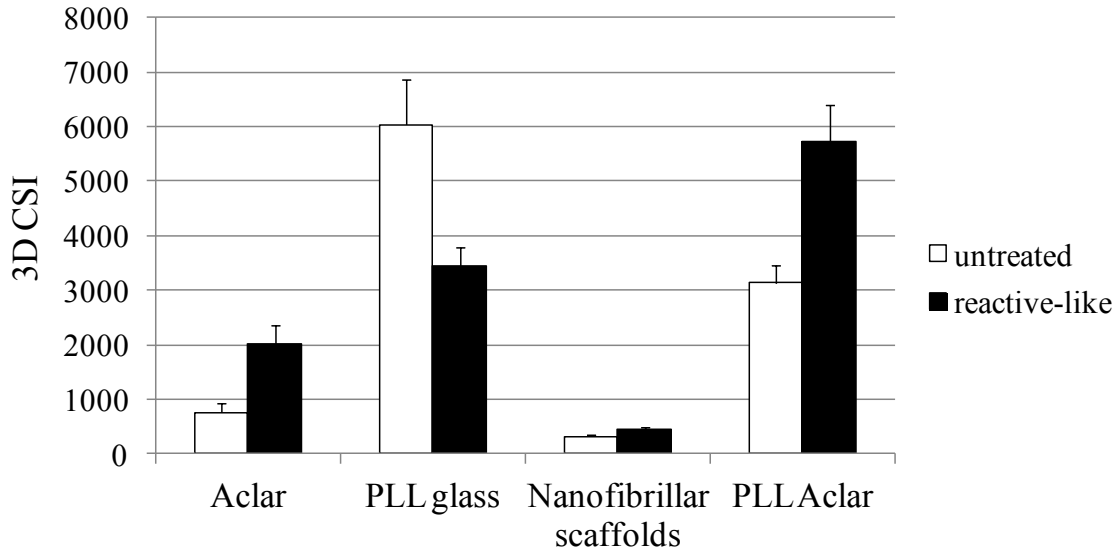

Figure 8.3: New CSI results of untreated and reactive-like astrocytes cultured on Aclar, PLL glass, nanofibrillar scaffolds, and PLL Aclar. Error bars show standard error.

8.4 Discussion

The field of measuring cell morphology changes is known as quantitative morphometry. CSI is a dimensionless two-dimensional cell shape analysis method [142]. A CSI that incorporates volume information acquired from high-resolution AFM height images of cells on culture surfaces was recently reported [120]. In this work, a new automatic cell segmentation method that can be successfully applied to cells on rough non-planar surfaces is presented. The new CSI is also dimensionless but includes quantitative information about the cell spreading and stellation.

Cell-matrix adhesion is mediated by biomolecular interactions between adhesion receptors on the plasma membrane and cell substrate. Cell spreading is an F-actin and myosin dependent process, and it is important for cell growth and cell motility. To date, cell spreading has been investigated by using confocal microscopy [157], and recently with AFM [158]. One of the advantages of AFM over CLSM is that AFM resolution with the J scanner used in this work, in z direction is less than 1 nm, whereas it is around 500 nm for CLSM. Thus, cell volume and cell surface area calculations with AFM are more accurate than CLSM. As a result, this study presents a very accurate quantitative evaluation of cell spreading.

The PLL functionalized surfaces are commonly used as a cell substrate for neural cells to increase cell adhesion. The astrocytes cultured on Aclar adopted a hemisphere-like shape, but the ones on PLL Aclar and PLL glass were well spread. The new CSI is a new quantitative cell morphology evaluation method that makes use of the volumetric information provided by high-resolution AFM investigation, expected to useful in biomedical science.

Chapter 9

Conclusions and future work

There is currently no treatment option for human CNS injury. However, CNS axons have been proven to grow in permissible environments; therefore, the primary problem to CNS injury is finding the chemical and physical conditions that will promote axon regeneration [159]. This dissertation demonstrates studies to elucidate the effects of nanophysical properties of a promising CNS scaffold on the modulation of the cellular and molecular components of glial scar.

In this research, dBcAMP-treatment was performed to obtain astrocytes that are similar to reactive astrocytes in the glial scar, and named as reactive-like astrocytes. Nanophysical cues of tissue scaffolds have been shown to affect morphology of untreated and dBcAMP-treated astrocytes, and the astrocyte cytoskeletal protein expressions including actin, GFAP, and tubulin (Chapter 6). Nanophysical cues that were investigated in this thesis are surface polarity, work of adhesion, surface roughness, and elasticity. The expression of F-actin, GFAP, and tubulin were quantified by CLSM z-series, and western blot. Western blot is used in biomedical science to detect specific proteins in the given sample but does not show the distribution of the protein in the cell cytoplasm. CLSM presents three-dimensional localization of protein which can also be used for quantification of specific proteins.

In conclusion, polyamide nanofibrillar scaffolds presented a mid-range of multiple cues to cells, while the comparative substrates presented cues that were extreme in one or more physical parameters. One major finding from this research was identification of the nanofibrillar scaffold

cues that corresponded to unchanged morphologies and cytoskeletal protein expressions even for cells with deliberately induced reactivity. Another important major finding was identification of a different set of nanophysical cues that induced morphological and protein expressions that recapitulated glial scar formation. A further major finding was that all of the following showed statistical differences as a function of the nanophysical cues presented by the culture environments: cytoskeletal proteins, reactivity proteins, and morphological expressions including process length, soma height, and cell shape index.

The special contribution to image processing for AFM investigations was presented in Chapter 7. GHPF is a useful feature for segmenting neural cells from nanofibrillar scaffolds. The comparison of GHPF and other local statistics and GLCM textural features on the recognition performance is given in Chapter 8. A new CSI definition which includes stellation and spreading behavior of cells is also explained in Chapter 8.

The investigation of neural cell responses with super-resolution microscopy, a form of high resolution light microscopy, continues. A preliminary study on the quiescent astrocyte-astrocyte interactions on the nanofibrillar scaffolds demonstrated contact spacing at 24 h, with interactions by stellate processes. While multiple examples of contacting structures that appeared to be in various stages of development were discovered using AFM, a protein composition investigation was below the resolution limit of the CLSM. A new capability, super-resolution microscopy, is starting to enable protein investigations below the optical diffraction limit using strategic combinations of emission, depletion and pixel-by-pixel analysis. The Figure 9.1 images, which are immunostained for GFAP, were acquired using on a gated stimulated emission depletion (GSTED) super-resolution microscopy system. An apparent contact (arrow) is located in the large field of view confocal image shown in Figure 9.1 A. The GFAP fibril thickness was

measured to be about 90 nm using the GSTED image and Huygens software (asterisk), and this is well below the level of resolution of confocal microscopy. The new information provided by the increased resolution indicates that function of the contacting process may be to increase the interaction area. Furthermore, approximate location of the contacting cell GFAP with that of the contacted cell is observed (left arrow), suggesting possible interaction(s) that can be explored.

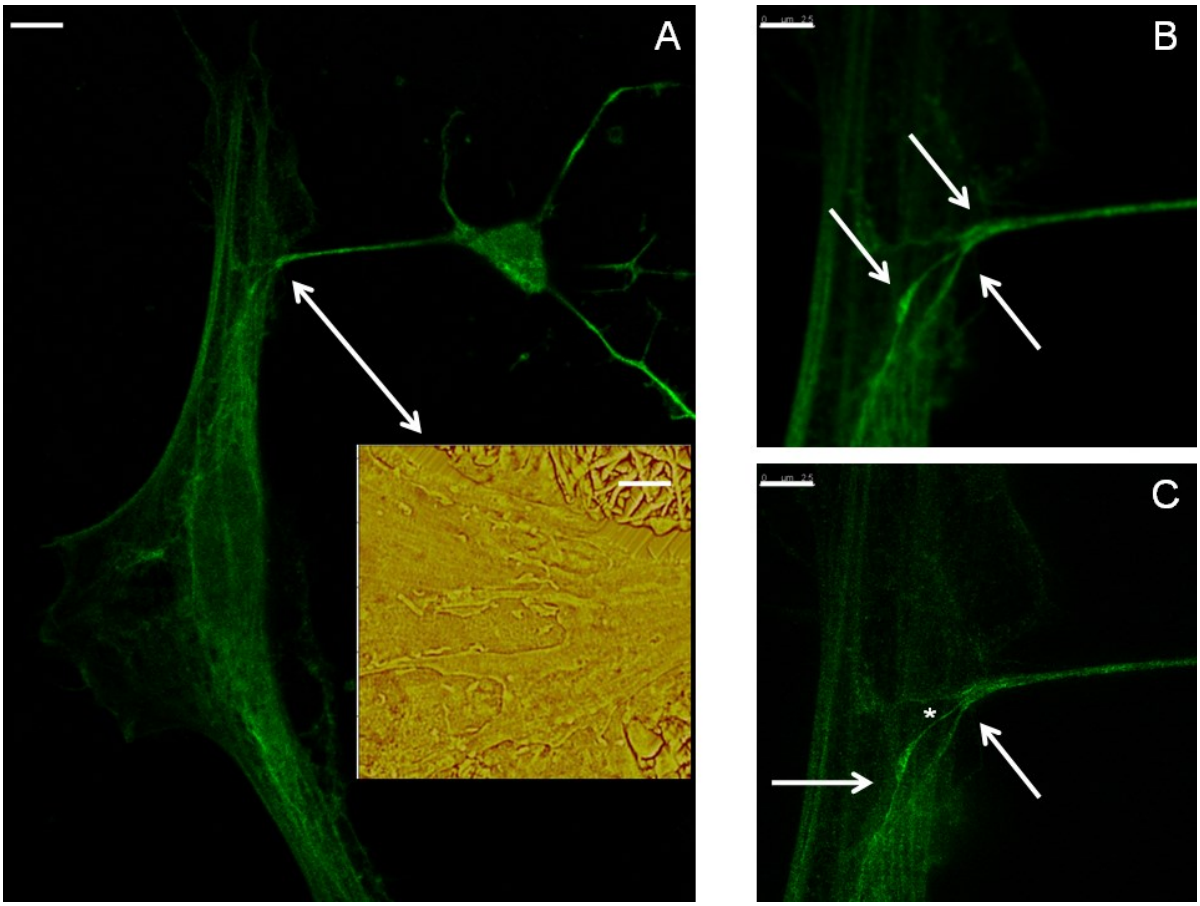

Figure 9.1. A. Confocal GFAP staining image of an intercellular contact (arrow) between untreated astrocytes cultured on nanofibrillar scaffolds. An AFM image of a contacting structure is shown in the inset. B. In the higher resolution confocal image, the contact points between the two cells (arrows) are not clearly resolved. C. In the STED image, the continuity of the connections to the process is clearly resolved (right arrow). A potential interaction between cells is shown by left arrow. The GFAP polymers were measured to be about 90 nm using the STED image and Huygens software (asterisk). Images, D. I. Shreiber and V. M. Ayres laboratories. Scale bars show 10, 2, 2.5 and 2.5 μm in A, A inset, B, and C, respectively.

Finally, there is a need for investigating the changes in the physical properties of tissue scaffolds over time. An ideal scaffold should have growth inhibitory cues for axonal regeneration at the acute phase of the recovery, but a growth promoting behavior in the chronic phase [160]. The degradation behavior of polyamide nanofibrillar scaffolds, the change in the physical properties of scaffolds over time, and the influence of physical property changes on the neural cell response remain as a future work.

BIBLIOGRAPHY

BIBLIOGRAPHY

[1] Ahmed I, Liu HY, Mamiya PC, Ponery AS, Babu AN, Weik T, Schindler M, Meiners S. Three-dimensional nanofibrillar surfaces covalently modified with tenascin-C-derived peptides enhance neuronal growth in vitro. *J Biomed Mater Res A* 76(4), 851–860 (2006).

[2] Nur-E-Kamal A, Ahmed I, Kamal J, Schindler M, Meiners S. Three-dimensional nanofibrillar surfaces induce activation of Rac. *Biochem Biophys Res Commun* 331(2), 428–434 (2005).

[3] Tejeda-Montes E, Smith KH, Poch M, López-Bosque MJ, Martín L, Alonso M, Engel E, Mata A. Engineering membrane scaffolds with both physical and biomolecular signaling. *Acta biomater* 8(3), 998–1009 (2012).

[4] Ereifej ES, Matthew HW, Newaz G, Mukhopadhyay A, Auner G, Salakhutdinov I, Vandevord PJ. Nanopatterning effects on astrocyte reactivity. *J Biomed Mater Res A* 101(6) 1–15 (2012).

[5] Hallab NJ, Bundy KJ, O'Connor K, Moses RL, Jacobs JJ. Evaluation of metallic and polymeric biomaterial surface energy and surface roughness characteristics for directed cell adhesion, *Tissue Eng* 7(1), 55–71 (2001).

[6] Discher DE, Janmey P, Wang Y. Tissue Cells Feel and Respond to the Stiffness of Their Substrate. *Science*, 310(5751) 1139–1143 (2005).

[7] Lampin M, Warocquier-Clerout R, Legris C, Degrange M, Sigot-Luizard MF. Correlation between substratum roughness and wettability, cell adhesion, and cell migration. *J Biomed Mater Res* 36(1) 99–108 (1997).

[8] Lipski AM, Pino CJ, Haselton FR, Chen IW, Shastri VP. The effect of silica nanoparticle-modified surfaces on cell morphology, cytoskeletal organization and function. *Biomaterials*, 29(28) 3836–3846 (2008).

[9] Janmey PA, van Oosten AS. Extremely charged and incredibly soft: physical characterization of the pericellular matrix. *Biophys J* 104(5) 961–963 (2013).

[10] Delgado-Rivera R, Harris SL, Ahmed I, Babu AN, Patel R, Ayres VM, Flowers DA, Meiners S. *Matrix Bio* 28 137-147 (2009).

[11] Iannaccone PM, Jacob HJ. Rats! *Dis Model Mech* 2(5–6), 206–210 (2009).

[12] Tiryaki VM, Ayres VM, Khan AA, Ahmed I, Shreiber DI, Meiners S. Nanofibrillar scaffolds induce preferential activation of Rho GTPases in cerebral cortical astrocytes. *Int J Nanomedicine*, 7, 3891-3905, (2012).

[13] Chen Q, Fan Y, Ayres VM, Udpa L, Schindler MS, Rice AF. Scanning probe recognition microscopy investigation of the elastic properties of tissue scaffolding. In *Materials Research Society*, Boston, MA (2005).

[14] Fan Y, Chen Q, Ayres VM, Baczewski AD, Udpa L, Kumar S. Scanning probe recognition microscopy investigation of tissue scaffold properties. *Int J Nanomed* 2(4), 651–661 (2007).

[15]Delgado Rivera R, Ayres VM, Chen Q, Fan Y, Flowers DA, Meiners S, Ahmed I. Scanning probe recognition microscopy investigation of neural cell prosthetic properties. *Int J Nanomanufacturing* 6, 279–290 (2010).

[16] Wang X, Bukoreshtliev NV, Gerdes HH. Developing neurons form transient nanotubes facilitating electrical coupling and calcium signaling with distant astrocytes. *PloS one* 7(10), e47429 (2012).

[17] Sitterberg J, Ozcetin A, Ehrhardt C, Bakowsky U. Utilising atomic force microscopy for the characterisation of nanoscale drug delivery systems. *Eur J Pharm Biopharm* 74(1), 2–13 (2010).

[18] Wang CC, Tsong TY, Hsu YH, Marszalek PE. Inhibitor binding increases the mechanical stability of staphylococcal nuclease. *Biophys J* 100(4) 1094–1099 (2011).

[19] Kreplak L, Wang H, Aebi U. Atomic force microscopy of mammalian urothelial surface. *J Mol Biol* 374(2) 365–373 (2008).

[20] Nedergaard M, Ransom B, Goldman SA. New roles for astrocytes: redefining the functional architecture of the brain. *Trends Neurosci* 26(10) 523–530 (2003)

[21] Matyash V, Kettenmann H. Heterogeneity in astrocyte morphology and physiology. *Brain Res Rev*, 63(1-2), 2–10 (2010).

[22] Abbott NJ, Rönnbäck L, Hansson E. Astrocyte-endothelial interactions at the blood-brain barrier. *Nat Rev Neurosci* 7(1), 41–53 (2006).

[23] Oberheim NA, Takano T, Han X, He W, Lin JH, Wang F, Xu Q, Wyatt JD, Pilcher W, Ojemann JG, Ransom BR, Goldman SA, Nedergaard M Uniquely hominid features of adult human astrocytes. *J Neurosci* 29 3276–3287 (2009)

[24] McKeon RJ, Jurynec MJ, Buck CR. The chondroitin sulfate proteoglycans neurocan and phosphacan are expressed by reactive astrocytes in the chronic CNS glial scar. *J Neurosci* 19(24), 10778–10788 (1999).

[25] Hikino M, Mikami T, Faissner A, Vilela-Silva AC, Pavão MS, Sugahara K. Oversulfated dermatan sulfate exhibits neurite outgrowth-promoting activity toward embryonic mouse hippocampal neurons: implications of dermatan sulfatein neuritogenesis in the brain. *J Biol Chem* 278, 43744–43754 (2003).

[26] Raisman, G. Myelin inhibitors: does NO mean GO? *Nat Rev Neurosci* 5, 157–161 (2004).

[27] Sofroniew MV, Vinters HV. Astrocytes: biology and pathology. *Acta neuropathol* 119(1), 7–35 (2010).

[28] Carlstedt T. Nerve fibre regeneration across the peripheral-central transitional zone. *J Anat* 190 51–56 (1997).

[29] Schmidt CE, Leach JB. Neural tissue engineering: strategies for repair and regeneration. *Annu Rev Biomed Eng* 5, 293–347 (2003).

[30] Zhou K, Nisbet D, Thouas G, Bernard C, Forsythe J. Bio-nanotechnology Approaches to Neural Tissue Engineering. Tissue engineering, InTech North America. 459–485 (2010).

[31] Albert E. Einige operationen an nerven. *Wien Med* 26 1285 (1885).

[32] Gluck T. Ueber Neuroplastik auf dem Wege der Transplantation. *Arch Klin Chir* 25 606–616 (1880).

[33] Payr E. Beitr¨age zur Technik der Blutgefass und Nervennaht nebst Mit-teilungen ¨ uber die Verwendung eines resorbibaren Metalles in der Chirurgie. *Arch Klin Chir* 62, 67 (1900).

[34] Kirk EG, Lewis D. Fascial tubulization in the repair of nerve defects. *JAMA* 65:486–92 (1915).

[35] Lundborg G. Nerve injury and repair. New York: Longman Group UK (1988).

[36] Mackinnon SE, Dellon AL. Surgery of the peripheral nerve. New York: Thieme Med. Publ. (1988).

[37] Meiners S, Ahmed I, Ponery AS, Amor N, Harris SL, Ayres VM, Fan Y, Chen Q, Delgado-Rivera R, Babu AN. Engineering electrospun nanofibers for spinal cord repair: A discussion. *Polymer Int* 56, 1340-1348 (2007).

[38] Meiners S, Harris SL, Delgado-Rivera R, Ahmed I, Babu AN, Patel RP, Crockett DP. A nanofibrillar prosthetic modified with fibroblast growth factor-2 for spinal cord repair In; Chang WN. editor. Nanofibers: Fabrication, Performance, and Applications. Hauppage, NY: Nova Science Publishers, Inc. 327–343 (2009).

[39] Binnig A, Rohrer G. Scanning tunneling microscopy. *Helvetica Physica Acta*, 55, 726–735 (1982).

[40] Guckenberger R, Heim M, Cevc G, Knapp HF, Wiegräbe W, Hillebrand A. Scanning tunneling microscopy of insulators and biological specimens based on lateral conductivity of ultrathin water films. *Science* 266(5190), 1538–1540 (1994).

[41] A practical guide to scanning probe microscopy, Veeco Instruments Inc, (2005).

[42] Parpura V, Haydon PG, Henderson E. Three-dimensional imaging of living neurons and glia with the atomic force microscope. *J Cell Sci* 104, 427–432 (1993).

[43] Schaus SS, Henderson ER. Cell viability and probe-cell membrane interactions of XR1 glial cells imaged by atomic force microscopy. *Biophys J* 73(3), 1205–1214 (1997).

[44] Lapshin RV. Feature-oriented scanning methodology for probe microscopy and nanotechnology. *Nanotechnology* 15(9), 1135–1151 (2004).

[45] Butt HJ, Cappella B, Kappl M. Force measurements with the atomic force microscope: Technique, interpretation and applications. *Surface Science Reports* 59(1–6), 1–152 (2005).

[46] Hansma HG. Surface biology of DNA by atomic force microscopy. *Annu Rev Phys Chem* 52, 71–92 (2001).

[47] Ng L, Grodzinsky AJ, Patwari P, Sandy J, Plaas A, Ortiz C. Individual cartilage aggrecan macromolecules and their constituent glycosaminoglycans visualized via atomic force microscopy. *J Struct Biol* 143(3), 242–257 (2003).

[48] Chen CH, Clegg DO, Hansma HG. Structures and dynamic motion of laminin-1 as observed by atomic force microscopy. *Biochemistry* 37(22), 8262–8267 (1998).

[49] Aifantis KE, Shrivastava S, Pelidou SH. Capturing the elasticity and morphology of live fibroblast cell cultures during degradation with atomic force microscopy. *J Microsc* 249(1), 62–68 (2013).

[50] Fan Y, Chen Q, Ayres VM, Baczewski AD, Udpa L, Kumar S. Scanning probe recognition microscopy investigation of tissue scaffold properties. *Int J Nanomed* 2(4), 651–61 (2007).

[51] Ayres VM, Chen Q, Fan Y, Flowers DA, Meiners SA, Ahmed I, Delgado-Rivera R. Scanning probe recognition microscopy investigation of neural cell prosthetic properties. *Int J Nanomanufacturing* 6, 279–290 (2010).

[52] Minsky MM. Microscopy apparatus, US 3013467 (1961)

[53] Pawley JB. Handbook of Biological Confocal Microscopy, Berlin: Springer. (2006).

[54] Bolte S, Cordelières FP. A guided tour into subcellular colocalization analysis in light microscopy. *J Microsc* 224, 213–232 (2006).

[55] Shastri VP, Lendlein A. Engineering materials for regenerative medicine, *MRS Bulletin* 35(8), 571-577 (2010).

[56] Ayres VM, Chen Q, Fan Y, Flowers DA, Meiners SA, Ahmed I, Delgado-Rivera R. Neural cell prosthetic investigation by scanning probe recognition microscopy. *6th International Symposium on Nanomanufacturing*, Athens, Greece, 5.B.2.(2008).

[57] Zhao BH, Lee IS, Han IH, Park JC, Chung SM. Effects of surface morphology on human osteosarcoma cell response. *Current Applied Physics* 7S1, e6-e10 (2007).

[58] Lipski AM, Jaquiery C, Choi H, Eberli D, Stevens M, Martin I, Chen IW, Shastri VP. Nanoscale engineering of biomaterial surfaces. *Adv Mater* 19, 553-557 (2007).

[59] Pelham RJ, Wang YL. Cell locomotion and focal adhesions are regulated by substrate flexibility. *Proc Natl Acad Sci USA* 94, 13661–13665 (1997).

[60] Kubinová Š, Horák D, Hejčl A, Plichta Z, Kotek J, Proks V, Forostyak S, Syková E. SIKVAV-modified highly superporous PHEMA scaffolds with oriented pores for spinal cord injury repair. *J Tissue Eng Regen Med* doi: 10.1002/term.1694 (2013).

[61] Thomas WE, Discher DE, Shastri VP. Mechanical regulation of cells by materials and tissues, *MRS Bulletin* 35(8), 578-583 (2010).

[62] Khan A, Philip J, Hess P. Young's modulus of silicon nitride used in scanning force microscope cantilevers. *J Appl Phys* 95(4), 1667-1672 (2004).

[63] Derjaguin BV, Muller VM, Toporov YP. Effect of Contact Deformations on the Adhesion of Particles. *Prog Surf Sci* 45(1-4), 131-143 (1994).

[64] Jogikalmath G, Stuart JK, Pungor A, Hlady V. Adhesion mapping of chemically modified and poly(ethylene oxide)-grafted glass surfaces. *Colloid Surface A* 154(1-2), 53-64 (1999).

[65] Chen Q, Fan Y, Ayres VM, Udpa L, Schindler MS, Rice AF. Scanning probe recognition microscopy investigation of the elastic properties of tissue scaffolding. *MRS* Warrendale, PA (2005).

[66] Hallab NJ, Bundy KJ, O'Connor K, Moses RL, Jacobs JJ. Evaluation of metallic and polymeric biomaterial surface energy and surface roughness characteristics for directed cell adhesion. *Tissue Eng* 7(1), 55–71 (2001).

[67] Ayres VM, Xie K, Tiryaki VM, Ahmed I, Shreiber DI. Investigation of Nanophysical Properties of Aging Polyamide Nanofibrillar Tissue Scaffolds by TEM, SAED, Contact Angle and Raman Spectroscopies. In *MRS* Boston, MA (2011).

[68] Roggendorf E. The biostability of silicone rubbers, a polyamide and a polyester. *J Biomed Mater Res* 10, 123 (1976).

[69] Hatamleh MM, Polyzois GL, Silikas N, Watts DC. Effect of extraoral aging conditions on mechanical properties of maxillofacial silicone elastomer. *J Prosthodont* 20, 439-446 (2011).

[70] Tiryaki VM, Khan AA, Pastor A, Alduhaileb RA, Delgado-Rivera R, Ahmed I, Meiners S, Ayres VM. Quantitative investigations of nanoscale elasticity of nanofibrillar matrices. In *MRS* Boston, MA, (2010).

[71] Ferrari AC, Robertson J. Resonant Raman spectroscopy of disordered, amorphous, and diamondlike carbon. *Phys Rev B* 64, 075414 (2001).

[72] Georges PC, Miller WJ, Meaney DF, Sawyer ES, Janmey PA. Matrices with compliance comparable to that of brain tissue select neuronal over glial growth in mixed cortical cultures. *Biophys J* 90, 3012-3018 (2006).

[73] McKeon RJ, Schreiber RC, Rudge JS, Silver J. Reduction of neurite outgrowth in a model of glial scarring following CNS injury is correlated with the expression of inhibitory molecules on reactive astrocytes. *J Neurosci* 11, 3398–3411 (1991).

[74] Tang X, Davies JE, Davies SJA. Changes in distribution, cell associations, and protein expression levels of NG2, neurocan, phosphacan, brevican, versican V2, and tenascin-C during acute to chronic maturation of spinal cord scar tissue. *J Neurosci Res* 71, 427–444 (2003).

[75] Biran R, Noble MD, Tresco PA. Characterization of cortical astrocytes on materials of differing surface chemistry. *J Biomed Mater Res* 46, 150–159 (1999).

[76] Patel KR, Tang H, Grever WE, Simon Ng KY, Xiang J, Keep RF, Cao T, McAllister JP 2nd. Evaluation of polymer and self-assembled monolayer-coated silicone surfaces to reduce neural cell growth. *Biomaterials* 27:1519–1526, (2006).

[77] Tonazzini I, Bystrenova E, Chelli B, Greco P, Stoliar P, Calò A, Lazar A, Borgatti F, D'Angelo P, Martini C, Biscarini F.. Multiscale morphology of organic semiconductor thin films controls the adhesion and viability of human neural cells. *Biophys J* 98, 2804–2812 (2010).

[78] Nobes CD, Hall A. Rho, Rac, and Cdc42 GTPases regulate the assembly of multimolecular focal complexes associated with actin stress fibers, lamellipodia, and filopodia. *Cell* 81(1), 53–62 (1995).

[79] Biyasheva A, Svitkina T, Kunda P, Baum B, Borisy G. Cascade pathway of filopodia formation downstream of SCAR. *J Cell Sci* 117, 837–848 (2004).

[80] Racchetti G, D'Alessandro R, Meldolesi J. Astrocyte stellation, a process dependent on Rac1 is sustained by the regulated exocytosis of enlargeosomes. *Glia* 60(3), 465–475 (2011).

[81] Chung HY, Hal JRB, Gogins MA, Douglas G. Crofoot, Thomas M. Weik. Donaldson Company, Inc. Polymer, polymer microfiber, polymer nanofiber and applications including filter structures. US 6743273 B2, (2004).

[82] Spatz C. Basic Statistics: Tales of Distributions. 10th ed. Belmont: Wadsworth Cengage Learning (2011).

[83] Tiryaki VM, Khan AA, Ayres VM. AFM feature definition for neural cells on nanofibrillar tissue scaffolds. *Scanning* 34, 316 (2012).

[84] Davis-Cox MI, Turner JN, Szarowski D, Shain W. Phorbol ester-stimulated stellation in primary cultures of astrocytes from different brain regions. *Microsc Res Tech* 29, 319–327 (1994).

[85] Kasa I. A curve fitting procedure and its error analysis. *IEEE Trans Inst Meas* 25 8–14, (1976).

[86] Ridley AJ, Paterson HF, Johnston CL, Diekmann D, Hall A. The small GTP-binding protein Rac regulates growth factor-induced membrane ruffling. *Cell* 70:401–410 (1992).

[87] Jones KJ, Korb E, Kundel MA, Kochanek AR, Kabraji S, McEvoy M, Shin CY, Wells DG. CPEB1 regulates beta-catenin mRNA translation and cell migration in astrocytes. *Glia* 56(13), 1401–1413 (2008).

[88] Etienne-Manneville S, Hall A. Rho GTPases in cell biology. *Nature* 420, 629–635 (2002).

[89] Bishop AL, Hall A. Rho GTPases and their effector proteins. *Biochem J* 348:241–255 (2000).

[90] Ridley AJ, Hall A. The small GTP-binding protein Rho regulates the assembly of focal adhesions and actin stress fibers in response to growth factors. *Cell* 70, 389–399 (1992).

[91] Kalman D, Gomperts SN, Hardy S, Kitamura M, Bishop JM. Ras family GTPases control growth of astrocyte processes. *Mol Biol Cell* 10, 1665–1683, (1999).

[92] Schneider CA, Rasband WS, Eliceiri KW. NIH Image to ImageJ: 25 years of image analysis. *Nature Methods* 9, 671–675 (2012).

[93] Abe K, Misawa M. Astrocyte stellation induced by Rho kinase inhibitors in culture. *Brain Res Dev Brain Res* 143, 99–104 (2003).

[94] Hall A. Rho GTPases and the actin cytoskeleton. *Science* 279, 509–514 (1998).

[95] Cook GMW. Glycoproteins in membranes. *Biol Rev* 43, 363–391 (1968).

[96] Finkelstein EI, Chao PG, Hung CT, Bulinski JC. Electric field-induced polarization of charged cell surface proteins does not determine the direction of galvanotaxis, cell motility and the cytoskeleton. *Cell Motil Cytoskeleton* 64, 833–846 (2007).

[97] Seil JT, Webster, TJ. Electrically active nanomaterials as improved neural tissue regeneration scaffolds. *Wiley Interdiscip Rev Nanomed Nanobiotechnol* 2, 635–647 (2010).

[98] Sivron T, Schwartz M. Glial-cell types, lineages, and response to injury in rat and fish - implications for regeneration. *Glia* 13(3), 157-165 (1995).

[99] Ridet JL, Malhotra SK, Privat A, Gage FH. Reactive astrocytes: cellular and molecular cues to biological function. *Trends Neurosci* 20(12), 570-577 (1997).

[100] Wilhelmsson U, Bushongt EA, Price DL, Smarr BL, Phung V, Terada M, Ellisman MH, Pekny M. Redefining the concept of reactive astrocytes as cells that remain within their unique domains upon reaction to injury. *P Natl Acad Sci USA* 103(46), 17513-17518 (2006).

[101] Wiese S, Karus M, Faissner A. Astrocytes as a source for extracellular matrix molecules and cytokines. *Front Pharmacol* 3, 120 (2012).

[102] Silver J, Miller JH. Regeneration beyond the glial scar. *Nat Rev Neurosci* 5(2), 146-156 (2004).

[103] Vignaud T, Galland R, Tseng QZ, Blanchoin L, Colombelli J, Thery M. Reprogramming cell shape with laser nano-patterning. *J Cell Sci* 125(9), 2134-2140 (2012).

[104] Koegler P, Clayton A, Thissen H, Santos GNC, Kingshott P. The influence of nanostructured materials on biointerfacial interactions. *Adv Drug Deliver Rev* 64(15), 1820-1839 (2012).

[105] Yim EKF, Pang SW, Leong KW. Synthetic nanostructures inducing differentiation of human mesenchymal stem cells into neuronal lineage. *Exp Cell Res* 313(9), 1820-1829 (2007).

[106] Wood JA, Ly I, Borjesson DL, Nealey PF, Russell P, Murphy CJ. The modulation of canine mesenchymal stem cells by nano-topographic cues. *Exp Cell Res* 318(19), 2438-2445 (2012).

[107] Ahmed I, Ponery AS, Nur-E-Kamal A, Kamal J, Meshel AS, Sheetz MP, Schindler M, Meiners S. Morphology, cytoskeletal organization, and myosin dynamics of mouse embryonic fibroblasts cultured on nanofibrillar surfaces. *Mol Cell Biochem* 301(1-2), 241-249 (2007).

[108] Engler AJ, Sen S, Sweeney HL, Discher DE. Matrix elasticity directs stem cell lineage specification. *Cell* 126(4), 677-689 (2006).

[109] Nemir S, West JL. Synthetic materials in the study of cell response to substrate rigidity. *Ann Biomed Eng* 38(1), 2-20 (2010).

[110] Leipzig ND, Shoichet MS. The effect of substrate stiffness on adult neural stem cell behavior. *Biomaterials* 30(36), 6867-6878 (2009).

[111] Banerjee A, Arha M, Choudhary S, Ashton RS, Bhatia SR, Schaffer DV, Kane RS. The influence of hydrogel modulus on the proliferation and differentiation of encapsulated neural stem cells. *Biomaterials* 30(27), 4695-4699 (2009).

[112] Liu T, Houle JD, Xu JY, Chan BP, Chew SY. Nanofibrous collagen nerve conduits for spinal cord repair. *Tissue Eng Pt A* 18(9-10), 1057-1066 (2012).

[113] Schindler M, Ahmed I, Kamal J, Nur-E-Kamal A, Grafe TH, Young Chung H, Meiners S. A synthetic nanofibrillar matrix promotes in vivo-like organization and morphogenesis for cells in culture. *Biomaterials* 26(28), 5624-5631 (2005).

[114] Jiang FX, Yurke B, Firestein BL, Langrana NA. Neurite outgrowth on a DNA crosslinked hydrogel with tunable stiffnesses. *Ann Biomed Eng* 36(9), 1565-1579 (2008).

[115] Fedoroff S, Mcauley WaJ, Houle JD, Devon RM. Astrocyte Cell Lineage .5. Similarity of Astrocytes That Form in the Presence of Dbcamp in Cultures to Reactive Astrocytes In vivo. *J Neurosci Res* 12(1), 15-27 (1984).

[116] Tiryaki, VM, Ayres, VM, Ahmed, I, Shreiber, DI. Differentiation of reactive-like astrocytes cultured on nanofibrillar and comparative culture surfaces. In press, *Nanomedicine* (2013).

[117] East E, Golding JP, Phillips JB. A versatile 3D culture model facilitates monitoring of astrocytes undergoing reactive gliosis. *J Tissue Eng Regen M* 3(8), 634-646 (2009).

[118] Rao S, Winter J. Adhesion molecule-modified biomaterials for neural tissue engineering. *Front Neuroeng* 2, 1-14 (2009).

[119] Dreher Z, Tout S, Stone J. Interactions of living astrocytes in vitro - evidence of the development of contact spacing. *Glia* 11(1), 57-63 (1994).

[120] Tiryaki VM, Adia-Nimuva U, Hartz SA, Xie K, Ayres VM, Ahmed I, Shreiber DI. New atomic force microscopy based astrocyte cell shape index. In *MRS*. UU: Scanning Probe Microscopy - Frontiers in Nanotechnology (2013).

[121] Yoshimura S, Sakai H, Nakashima S, Nozawa Y, Shinoda J, Sakai N, Yamada H. Differential expression of Rho family GTP-binding proteins and protein kinase C isozymes during C6 glial cell differentiation. *Mol Brain Res* 45(1), 90-98 (1997).

[122] Charrierebertrand C, Leprince G, Bouchier C, Fages C, Tardy M, Nunez J. Expression of tubulin, GFAP and of their encoding messenger-RNAs during the proliferation and differentiation of cultured astrocytes. *Neurochem Int* 15(2), 215-222 (1989).

[123] Georges P, McCormick M, Flanagan L, Ju Y, Sawyer E, Janmey P. Tuning the elasticity of biopolymer gels for optimal wound healing. In: *MRS*. Boston, MA (2005).

[124] Taber LA. Towards a unified theory for morphomechanics. *Philos T R Soc A* 367(1902), 3555-3583 (2009).

[125] Zuidema JM, Pap MM, Jaroch DB, Morrison FA, Gilbert RJ. Fabrication and characterization of tunable polysaccharide hydrogel blends for neural repair. *Acta Biomater* 7(4), 1634-1643 (2011).

[126] Wang CC, Tsong TY, HsuYH, Marszalek PE. Inhibitor binding increases the mechanical stability of staphylococcal nuclease. *Biophys J* 100, 1094–1099 (2011).

[127] Kreplak L, Wang H, Aebi U, Kong X. Atomic force microscopy of mammalian urothelial surface. *J Mol Biol* 374, 365–373 (2007).

[128] Grafe T, Graham K. Polymeric nanofibers and nanofiber webs: a new class of nonwovens. *Proceedings of the International Nonwovens Technical Conference*, Atlanta, GA, 24–26 (2002).

[129] Frigo M, Johnson SG. FFTW: an adaptive software architecture for the FFT. *Proceedings of the International Conference on Acoustics, Speech, and Signal Processing* 3:1381–1384 (1998).

[130] Gonzalez RC, Woods RE. Digital Image Processing 3rd ed. Prentice Hall, Upper Saddle River, NJ (2008).

[131] Tiryaki VM, Ayres VM, Khan AA, Flowers DA, Ahmed I, Flowers, DA, Ahmed, I, Delgado-Rivera, R and Meiners, S. Investigation of nanofibrillar influence on cell-cell interactions of astrocytes by atomic force microscopies. In *MRS*, Boston, MA (2011).

[132] Gerdes HH, Carvalho RN. Intercellular transfer mediated by tunneling nanotubes. *Curr Opin Cell Biol* 20, 474–475 (2008).

[133] Kienberger F, Pastushenko VP, Kada G, Chtcheglova L, Riethmueller C, Rankl C, Ebner A, Hinterdorfer P. Improving the contrast of topographical AFM images by a simple averaging filter. *Ultramicroscopy* 106, 822–828 (2006).

[134] Liu Q, Wang H, Liu J, Huang H. AFM image processing for estimating the number and volume of nanoparticles on a rough surface. *Surf Interface Anal* 43:1354–1359 (2010).

[135] Osher SJ, Rudin LI. Feature-oriented image enhancement using shock filters. *SIAM J Numer Anal* 27, 919-940 (1990).

[136] Alvarez L, Mazorra L. Signal and image restoration using shock filters and anisotropic diffusion. *SIAM J Numer Anal* 31, 590–605 (1994).

[137] Gilboa G, Sochen N, Zeevi YY. Regularized shock filters and complex diffusion. *Proceedings of the European Conference on Computer Vision'02* 399–313 (2002).

[138] Zou Z, Zheng Q, Wu Y, Guo X, Yang S, Li J, Pan H. Bio-compatibility and bioactivity of designer self-assembling nanofiber scaffold containing FGL motif for rat dorsal root ganglion neurons. *J Biomed Mater Res A* 95, 1125–1131 (2010).

[139] Hwang CM, Sant S, Masaeli M, Kachouie NN, Zamanian B, Lee SH, Khademhosseini A. Fabrication of three-dimensional porous cell-laden hydrogel for tissue engineering. *Biofabrication* 2, 1–12 (2010).

[140] Zhou M, Smith AM, Das AK, Hodson NW, Collins RF, Ulijn RV, Gough JE. Self-assembled peptide-based hydrogels as scaffolds for anchorage-dependent cells. *Biomaterials* 30, 2523–2530 (2009).

[141] Lisy M, Pennecke J, Brockbank KG, Fritze O, Schleicher M, Schenke-Layland K, Kaulitz R, Riemann I, Weber CN, Braun J, Mueller KE, Fend F, Scheunert T, Gruber AD, Albes JM, Huber AJ, Stock UA. The performance of ice-free cryopreserved heart valve allografts in an orthotopic pulmonary sheep model. *Biomaterials* 20, 5306–5311 (2010).

[142] Matsutani S, Yamamoto N. Neuronal regulation of astrocyte morphology in vitro is mediated by GABAergic signaling. *Glia* 20, 1-9, (1997).

[143] Vartanian KB, Kirkpatrick SJ, Hanson SR, Hinds MT. Endothelial cell cytoskeletal alignment independent of fluid shear stress on micropatterned surfaces. *Biochem Biophys Res Commun* 371, 787-792 (2008).

[144] Dike LE, Chen CS, Mrksich M, Tien J, Whitesides GM, Ingber DE. Geometric control of switching between growth, apoptosis, and differentiation during angiogenesis using micropatterned substrates. *In Vitro Cell Dev Biol Anim* 35, 441-448, (1999).

[145] Chen CS, Mrksich M, Huang S, Whitesides GM, Ingber DE. Micropatterned surfaces for control of cell shape, position, and function. *Biotechnol Prog* 14, 356-363 (1998).

[146] Chen CS, Mrksich M, Huang S, Whitesides GM, Ingber DE. Geometric control of cell life and death. *Science* 276(5317), 1425-1428, (1997).

[147] Canham P B, Burton AC. Distribution of size and shape in populations of normal human red cells. *Circ Res* 22(3), 405–422 (1968).

[148] Chvátal A, Andrová M, Kirchhoff F. Three-dimensional confocal morphometry - a new approach for studying dynamic changes in cell morphology in brain slices. *J Anat* 210, 671-683 (2007).

[149] Pincus Z, Theriot A. Comparison of quantitative methods for cell-shape analysis. *J Microsc* 227, 140-156 (2007).

[150] Petroski RE, Grierson JP, Choikwon S, Geller HM. Basic fibroblast growth-factor regulates the ability of astrocytes to support hypothalamic neuronal survival in vitro. *Dev Biol* 147(1), 1-13 (1991).

[151] Bolle R, Connell J, Haas N, Mohan R, Taubin G. Veggievision: a produce recognition system. *Proceedings of the 3rd IEEE Workshop on Applications of Computer Vision*, Sarasoto, FL, 244–251 (1996).

[152] Pudil P, Novovicova J, Kittler J. Floating Search Methods in Feature Selection. *Pattern Recognition Letters*, 15, 119-125 (1994).

[153] Riedmiller M, Braun H. A direct adaptive method for faster backpropagation learning: the RPROP algorithm. *Proceedings of the IEEE International Conference on Neural Networks*, 586-591 (1993).

[154] Hall-Beyer M. http://www.fp.ucalgary.ca/mhallbey/ Version: 2.10 February (2007).

[155] Haralick RM, Shanmugam K, Dinstein I. Textural features for image classification. *IEEE Transactions on Systems, Man and Cybernetics* 3(6), 610-620 (1973).

[156] Korchev YE, Gorelik J, Lab MJ, Sviderskaya EV, Johnston CL, Coombes CR, Vodyanoy I, Edwards CRW. Cell volume measurement using scanning ion conductance microscopy. *Biophys J* 78, 451-457, (2000).

[157] Fardin MA, Rossier OM, Rangamani P, Avigan PD, Gauthier NC, Vonnegut W, Mathur A, Hone J, Iyengarband R, Sheetz MP. Cell spreading as a hydrodynamic process. *Soft Matter* 6, 4788-4799, (2010).

[158] Shao W, Jin H, Huang J, Qiu B, Xia R, Deng Z, Cai J, Chen Y. AFM investigation on Ox-LDL-induced changes in cell spreading and cell-surface adhesion property of endothelial cells *Scanning*, 35(2), 119-126 (2012).

[159] Recknor JB, Mallapragada SK. Nerve regeneration: tissue engineering strategies, The Biomedical Engineering Handbook: Tissue Engineering and Artificial Organs, Taylor & Francis: New York (2006).

[160] Rolls A, Shechter R,Schwartz M. The bright side of the glial scar in CNS repair. *Nat Rev Neurosci* 10(3), 235–241 (2009).